

An-Najah National University

Faculty of Graduate Studies

**Synthesis of Nano-Meter-Sized Core-Shell Bimetallic
Magnesium-Palladium Clusters and Their Hydrogen Uptake
Capacity**

By

Diaa "Mohammed Marouf" Saleh Aref

Supervisor

Dr. Mohammed Suleiman

**This Thesis is Submitted in Partial Fulfillment of the Requirements for
the Degree of Master of Chemistry, Faculty of Graduate Studies, An-
Najah National University, Nablus, Palestine.**

2014

Synthesis of Nano-Meter-Sized Core-Shell Bimetallic Magnesium-Palladium Clusters and Their Hydrogen Uptake Capacity

By
Diaa "Mohammed Marouf" Saleh Aref

This thesis was Defended Successfully on 2/1/2014 and approved by:

Defense Committee Members

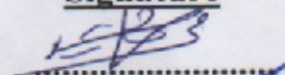
1. Dr. Mohammed Suleiman / Supervisor

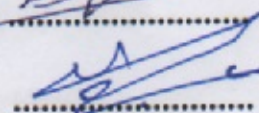
2. Prof. Atef Qasrawi / External Examiner

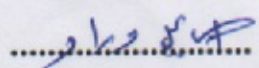
3. Prof. Ismail Warad / Internal Examiner

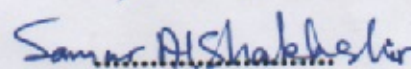
4. Dr. Samar AL-Shakhshir / Internal Examiner

Signature









Dedication

أهدي عملي هذا خالصا لله "سبحانه و تعالی" و لوجهه الكريم.

و أسأله ان يتقبل عملي هذا خالصا له سبحانه و تعالی.

اللهم صل و سلم على سيدنا

محمد (صلى الله عليه وسلم)

I dedicate my dissertation work purely to the Lord (Allah) his Glorified and Exalted and to his Countenance with full of majesty, full of honor.

"O Allah, I am asking you to accept this work purely for you."

O Allah,

Bless and Peace on the Master

Muhammad (peace is upon him)

Acknowledgement

The Author wishes with deepest appreciation to his supervisor Dr. M. Suleiman for his guidance, help and moral support during research work and thesis writing.

The Author would like to express his deepest appreciation to Prof. I. Warad for his Encouragement and every one, who teaches him at An-Najah National University.

Thanks are due to the technical staff in Chemistry and CEMSANT Laboratory-Sciences Department for their technical help, especially Mr. O. Nabulsi and Mr. N. Dwekat. to King Abdullah Institute at King Saud University for SEM, SEM-EDX and TEM measurements, to Güttingen Institute – Güttingen - Germany for TEM, TEM-EDX measurements and to Dr. D. Bikiaris at Aristotle University – Thessaloniki - Greece for XRD measurements.

Author would also like to express his deepest appreciation and thanks to his dearests father and mother for their continuous encouragement, supporting and their patience during the study period.

Finally, I would like to thank my brothers and sisters "Saleh, Ahmad, Joan and sweetie Aman", my uncles and never forget my dearest friends "Waseem, Moath, Anas, Moumen, Younes and Mazin".

Diaa Aref

الإقرار

أنا الموقع أدناه مقدم الرسالة التي تحمل العنوان

Synthesis of Nano-Meter-Sized Core-Shell Bimetallic Magnesium-Palladium Clusters and Their Hydrogen Uptake Capacity

أقر بأن ما اشتملت عليه الرسالة هو نتاج جهدي الخاص، باستثناء ما تمت الإشارة إليه حيثما ورد، وأن هذه الرسالة ككل، أو أي جزء منها لم يقدم من قبل لنيل أي درجة أو لقب علمي أو بحثي لدى أي مؤسسة تعليمية أو بحثية أخرى.

Declaration

The work provided in this thesis, unless otherwise referenced, is the researcher's own work, and has not been submitted elsewhere for any other degree or qualification.

Student's name:

اسم الطالب:

Signature:

التوقيع:

Date:

التاريخ:

List of Contents

No.	Content Title	Page
	DEDICATION	iii
	ACKNOWLEDGEMENT	iv
	Declaration	v
	List of Abbreviations	xvi
	List of Contents	vi
	List of Figures	ix
	List of Tables	xiv
	ABSTRACT	xviii
	CHAPTER (1) INTRODUCTION	1
1.1	Introduction to Nano-Sized Materials	3
1.1.1	Nanoscience and Nanotechnology "General Perspective"	3
1.1.2	Nanosized Materials "Properties and Classifications"	4
1.1.3	"Mono and Bi" Metallic Nanoparticles and Clusters	10
1.1.4	Methods of Synthesis Nanosized Particles and Metallic Clusters	15
1.1.4.1	Stepwise Formation of Colloidal Metallic Nanosized Particles and Clusters by Wet-Chemical Methods	17
1.1.4.2	Stabilization of Colloidal Metallic Clusters	19
1.1.4.2.1	Electrostatic Stabilization Manner	20
1.1.4.2.2	Steric Stabilization Manner	20
1.1.4.3	Mechanism of "Mono and Bimetallic" Clusters Formation By Electrochemical Technique	22
1.2	Introduction to Hydrogen Storage Technology	25
1.2.1	Hydrogen Storage Technology "General Perspective"	25
1.2.2	Metals as Solid Materials for Hydrogen Storage	32
1.2.2.1	Thermodynamics of Metal Hydride Fomation and Phase Transition	35
1.2.2.2	Kinetics of Metal Hydrides Formation	42
1.2.3	Experimental Techniques for Hydrogen Absorption/Desorption Measurements	44
	CHAPTER (2) LITERATURE REVIEW	45
2.1	Palladium as Hydrogen Storage Material	45
2.2	Magnesium as Hydrogen Storage Material	48

2.3	Combined Palladium and Magnesium Solids as Hydrogen Storage Materials	50
2.4	Objectives of This Work	53
	CHAPTER (3) EXPERIMENTAL TECHNEQUES	54
3.1	Chemicals and Materials	54
3.2	Equipments and Apparatus	55
3.2.1	Fourier-Transform-Infrared Spectrophotometers (FT-IR)	56
3.2.2	Scanning Electron Microscope (SEM)	56
3.2.3	Powder X-Ray diffraction (XRD)	57
3.2.4	Transmission Electron microscope (TEM)	57
3.2.5	Energy Dispersive X-Ray Spectroscopy (EDX)	58
3.2.6	Atomic Absorption Spectroscopy (AAS)	58
3.2.7	UV-VIS Spectroscopy	58
3.2.8	Volumetric and Gravimetric Hydrogen Storage Measurements	59
3.3	Preparation of Cluster Samples	59
3.3.1	General Procedure for the Preparation of Magnesium-Palladium Clusters	60
3.3.1.1	Electrochemical Preparation of Cluster Samples	60
3.3.1.2	Vacuum drying for Prepared Solids	60
3.4	The Measurements of Hydrogen Storage Capacity	61
3.4.1	Gravimetric Measurements	61
3.4.1.1	General Procedure for the Hydrogen Measurements	62
3.4.1.1.1	Sample Pre-Treatment	62
3.4.1.1.2	Hydrogen Absorption/Desorption Thermodynamic Measurements	63
3.4.1.1.3	Hydrogen Absorption/Desorption Kinetics	64
3.4.2	Volumetric Measurements	65
	CHAPTER (4) RESULTS & DISCUSSIONS	67
4.1	Samples Preparation and Characterization	67
4.1.1	Fourier Transform – Infrared Spectroscopy of as-Prepared Cluster Samples	69
4.1.2	Scanning Electron Microscopy of as-Prepared Cluster Samples	74
4.1.3	Transmission Electron Microscopy of as-Prepared Cluster Samples	75
4.1.4	X-Ray Diffraction of as-Prepared Cluster Samples	82

4.1.5	Energy Dispersed X-Ray of as-Prepared Cluster Samples	87
4.1.6	Atomic Absorption Spectroscopy of as-Prepared Cluster Samples	91
4.1.7	UV-VIS spectroscopy of as-Prepared Cluster Samples	95
4.1.8	Structure, Morphology and Crystallite of as-Prepared Clusters	101
4.1.9	Size and Size-Distribution of as-Prepared Clusters	103
4.1.10	Influence of the Electrolysis Parameters	104
4.2	Hydrogen Storage Measurements of as-Prepared Clusters	107
4.2.1	Hydrogen Volumetric Measurements	107
4.2.2	Hydrogen Gravimetric Measurements of as-Prepared Clusters " Size of 3.5 nm and Mg ₁ Pd ₃ stoichiometry"	111
4.2.2.1	Pressure-Concentration (Composition)-Isotherm (PCI)	111
4.2.2.2	Hydrogen Absorption and Desorption Kinetics	118
	Conclusions	121
	Suggestion for Farther Works	123
	References	124
	المخلص	ب

List of Figures

No.	Figure Title	Page
1.1	Schematic image describes the difference between energy levels of the bulk, nanoparticles and molecules.	5
1.2	Mass-abundance spectra of gold (left) and titanium (right) clusters, showing electronic and geometric magic numbers, respectively. The lower panel shows a schematic representation of the sequence of spherical electronic shells, as it applies to gold clusters, and a number of small symmetric geometric structures, which apply to titanium clusters.	8
1.3	Schematic image describe different morphological structures of bimetallic nanoparticles by models.	12
1.4	Different shapes of core/shell nanoparticles: (a) spherical core/shell nanoparticles; (b) hexagonal core/shell nanoparticles; (c) multiple small core materials coated by single shell material; (d) nano-matryushka material; (e) movable core within hollow shell material.	15
1.5	Stepwise formation of colloidal metallic clusters by "Wet-Chemical Techniques".	17
1.6	Schematic image describes the stabilization of a colloidal metallic cluster by the tetraoctylammonium bromide (TOAB).	19
1.7	Schematic image describes the electrostatic stabilization manner of metallic clusters.	21
1.8	Schematic image describes the steric stabilization manner of metallic clusters.	22
1.9	Schematic image of electrochemical mechanisms of preparation for stabilized M-clusters.	23

1.10	The volumetric and gravimetric H-densities for different hydrogen storage strategies and materials.	30
1.11	One-Dimensional Potential Energy Diagram according to the distance of the hydrogen gas from the metal surface.	35
1.12	Schematic image describes the adsorption and diffusion of H-atoms in the interface and bulk of M-host solid.	36
1.13	Pressure-Composition-Temperature Isotherm (PCI) curves (left hand side) and the resulting van't Hoff plot (right hand side) for thermodynamic metal-hydride formation.	36
1.14	The <i>PIT</i> isotherm and schematic representative images for the relationship between H-diffusion and lattice constant during absorption of H-atoms.	37
1.15	Schematic image describes the phase transition for M-H system and their stepwise of phase-transitions for H-absorption and desorption processes.	40
1.16	Hypothetical (PCI) for both H-absorption (blue curve) and desorption (red curve) processes that clarifies the <u>Hysteresis</u> .	41
3.1	Photographic image for the setup that was used in the preparation of samples. Composed of three main parts: (I) electrolysis cell (Pd-anode, counter cathode and nitrogen inlet/outlet system), (II) power supply for current generation and (III) ultrasonic shaking system.	55
3.2	Schematic image for the drying vacuum setup of as-prepared clusters through extracting the clusters from the reaction solution by siphoned off the supernatant.	61
3.3	Schematic image of High-Vacuum Electronic-Microbalance was used in Hydrogen gravimetric measurements	62

3.4	Schematic draw image of hydrogen gravimetric loading-unloading steps which was going to use for constructing the pressure-composition isotherm.	64
3.5	Photographic image (upward) and schematic image (downward) for the designed volumetric apparatus and its main compartments.	66
4.1	FT-IR spectrum for the TOAB in its pure solid form.	70
4.2	FT-IR spectrum of the as-prepared cluster samples (No. 1-4) for TOAB-stabilized Clusters.	73
4.3	SEM images of the as-prepared cluster samples (No. 1-4) for TOAB-stabilized MgPd CS Clusters.	74
4.4	TEM images of the as-prepared cluster sample (No. 1), which was prepared at $J = 5.2 \text{ mA.cm}^{-2}$ and $C_{\text{Mg}} = 0.022 \text{ M}$. The scale bar is: (a) 100 nm, (b) 50 nm, (c) 20 nm and (d) 10 nm.	76
4.5	TEM images of the as-prepared cluster sample (No. 2), which was prepared at $J = 3.0 \text{ mA.cm}^{-2}$ and $C_{\text{Mg}} = 0.022 \text{ M}$. The scale bar is: (a) 200 nm, (b) 100 nm, (c) 50 nm and (d) 20 nm.	77
4.6	TEM images of the as-prepared cluster sample (No. 3), which was prepared at $J = 3.0 \text{ mA.cm}^{-2}$ and $C_{\text{Mg}} = 0.049 \text{ M}$. The scale bar is: (a) 50 nm, (b), (c) and (d) 20 nm.	78
4.7	TEM images of the as-prepared cluster sample (No. 4), which was prepared at $J = 1.5 \text{ mA.cm}^{-2}$ and $C_{\text{Mg}} = 0.022 \text{ M}$. The scale bar is: (a) and (b) 50 nm, (c) and (d) 20 nm.	74
4.8	Size and size-distribution of as-prepared cluster sample (No. 2).	80
4.9	Constructed size-histograms for the size and size-distribution of as-prepared clusters (No.1-4) that	81

	obtained by the TEM.	
4.10	The XRD-patterns of the as-prepared cluster samples (No.1-4).	84
4.11	Lorentzian fitted function of XRD-patterns of the as-prepared cluster samples (No.1-4) that was performed with Origen-Lab program in order to estimate the position of the diffraction peaks and FWHM-values.	85
4.12	SEM-EDX profile of the as-prepared cluster samples (No. 1-4).	89
4.13	TEM-EDX profile of the as-prepared cluster sample (No. 2)	90
4.14	Schematic image describes the constructed models for the sizes and core to shell stoichiometry of the as-prepared clusters in samples (No. 1-4) that was obtained by TEM and AAS-data analysis, respectively.	94
4.15	UV-Vis spectra profile of the as-prepared cluster samples (No. 1- 4), and downward the image for the solutions of the four cluster samples were prepared at same concentration.	97
4.16	Schematic image for the hybridization model that describes the interaction between Core-sphere and Shell-cavity Plasmons and the formation of bonding and anti-bonding Plasmon modes.	98
4.17	UV-Vis spectra profile the as-prepared cluster samples (No.1-4), the wavelength values of absorption band are characterized in order to use in measuring band gap energy.	100
4.18	The effect of the current density (J) on the TEM-obtained size of the as-prepared clusters.	100

4.19	The stability profile for the volumetric apparatus under approximate 1bar of H-loading.	108
4.20	Volumetric profile of H-absorption of the as-prepared cluster samples (No.1- 4) after loading with approximate 1bar of H ₂ gas at ambient temperature. The drop in the pressure value during time progressing are corresponding to the amount of absorbed hydrogen by a certain weight of cluster sample.	109
4.21	H-loading (A) and Unloading (B) profiles of the Gravimetric measurements for as-prepared cluster sample (No.2) have (clusters' size ca. 3.5nm and Mg ₁ Pd ₃ stoichiometric formula). The left y-axes show the amount of hydrogen absorbed and desorbed at different hydrogen pressure loading and unloading steps per time progress in minutes (x-axes).	113
4.22	PCI of the as-prepared cluster sample (No. 2) with (clusters, size ca. 3.5 nm and Mg ₁ Pd ₃ stoichiometric formula). The blue-colored curve is H-absorption isotherm. The red-colored curves for the H-desorption isotherm.	114
4.23	The hysteresis between the absorption-desorption isotherms of the as-prepared cluster sample (No. 2)	115
4.24	H-absorption (left-hand side) and desorption (right-hand side) of as-prepared Cluster sample (No. 2) with (Mg ₁ Pd ₃ stoichiometry and size ca. 3.5 nm) that obtained at ambient conditions 298 K and 1bar (0.1MPa).	119

List of Tables

No.	Table Title	Page
1.1	Summary of the No. of surface atoms and shows how the percent of surface atoms increases at less sized GaAs nanoparticle.	6
1.2	The relation between the number of atoms in Pd-cluster with "cubic close packing" of n-shell with the No. of surface atoms (N_s), whole No. of cluster atoms (N) and cluster size in diameter (d).	10
1.3	Typical preparations and characterizations of bimetallic nanoparticles reported in literature.	14
1.4	The technical system targets of H-storage carriers, based on DOE for Fuel-Cell-Vehicles.	20
1.5	The energy densities (ED's) for different energy storage materials with clarifying some examples and recent uses.	28
2.1	Volumetric and gravimetric hydrogen content of different materials.	50
4.1	The preparation conditions of the four as-prepared cluster samples (1-4) and their metallic composition wt. %.	68
4.2	The spectral regions for TOAB in its pure-solid form.	71
4.3	The size and size-distribution of as-prepared clusters that was obtained by the analysis of TEM.	82
4.4	The XRD-diffraction peaks; the orientations for (111) and (200) planes of the as-prepared cluster samples (No. 1-4).	86
4.5	The estimated size (in diameter) of as-prepared clusters;	87

	obtained from using Scherrers' formula for the fitted peak of (111) plane.	
4.6	The exact wt. of as-prepared cluster samples was used in preparing the stock solution for analysis and the amounts of Pd and Mg have been detected (in ppm) by AAS.	91
4.7	The amounts of Pd and Mg (in mg) and (mmoles) that were obtained by AAS in as-prepared cluster samples.	92
4.8	The wt. % of each metal (Pd and Mg) and the wt. % of the metallic composition in as-prepared cluster samples and their Pd:Mg mole-ratios.	92
4.9	The wavelength of absorption band and the calculated band gap energy (in eV) of acetone dispersed as-prepared clusters.	101
4.10	The Clusters' size and size-distribution of the as-prepared clusters that obtained by TEM and XRD.	104
4.11	The electrochemical preparation parameters (J and C_{Mg}) and the obtained characterization properties (size, E_g , and Pd:Mg mol-ratio) by different characterization techniques (TEM, UV-Vis spectroscopy and AAS) of the four as-prepared clusters.	106
4.12	The properties "size and stoichiometry" of the as-prepared clusters and the obtained pressure difference and (H/MgPd) wt % of these studied clusters.	110
4.13	The H-properties for the (as-prepared cluster No.2) with clusters size 3.5 nm and M-stoichiometry of Mg_1Pd_3 that was obtained from the PCI for Hydrogen absorption-desorption processes.	118

List of Abbreviations

Symbol	Abbreviation
<i>H</i>	Hydrogen (atom(s) or molecule(s))
<i>Mg</i>	Magnesium metal(s) (atom(s)) [M.wt.= 24.306g.mol ⁻¹]
<i>Pd</i>	Palladium metal(s) (atom(s)) [M.wt.= 106.43g.mol ⁻¹]
<i>MgPd</i>	Magnesium and Palladium alloys (or Combination)
<i>M</i>	Metal(s) (Metallic portion or composites)
<i>M-H</i>	Metal Hydride (Metal-Hydrogen system)
<i>TOAB</i>	Tetraoctylammonium bromide
<i>CS</i>	Core-Shell morphology (Structure)
<i>MgPd-CS</i>	Magnesium-Palladium Core-Shell Clusters
<i>UHVEM</i>	Ultra-High-Vacuum Electronic Microbalance
<i>J</i>	Current Density (mA.cm ⁻²)
<i>nm</i>	Nanometer unit
<i>FT-IR</i>	Fourier Transform-Infrared (spectroscopy)
<i>SEM</i>	Scanning Electron Microscopy
<i>TEM</i>	Transmission Electron Microscopy
<i>XRD</i>	Powder X-ray Diffraction
<i>AAS</i>	Atomic-Absorption Spectroscopy
<i>SEM-EDS</i>	Energy Dispersive X-Ray Spectroscopy
<i>(SEM-EDX)</i>	attached with SEM
<i>TEM-EDS</i>	Energy Dispersive X-Ray Spectroscopy
<i>(TEM-EDX)</i>	attached with TEM
<i>UV-Vis</i>	Ultraviolet-Visible-near infrared Spectroscopy
<i>FWHM</i>	Full Width at the Half of Maximum
<i>PCI</i>	Pressure-Concentration-Temperature Isotherm
<i>PIT</i>	Pressure-Lattice-Temperature Isotherm
<i>SPRB</i>	Surface Plasmon Resonance Band
<i>E_g</i>	Band Gap Energy
<i>eV</i>	Electron Volt (6.24150934×10 ¹⁸ J)
<i>H/M</i>	Mole H/Mole <u>M</u> (<u>Metallic-Composite of Cluster</u>)
<i>Wt.</i>	Weight
<i>(WtH/WtM)</i>	Hydrogen Storage Capacity in weight percent
<i>[Wt. %]</i>	Weight percent
<i>θ_s^o_(abs)</i>	Miscibility gap slope-degree for H-absorption process
<i>θ_s^o_(des)</i>	Miscibility gap slope-degree for H-desorption process

Synthesis of Nano-Meter-Sized Core-Shell Bimetallic Magnesium-Palladium Clusters and Their Hydrogen Uptake Capacity

By

Diaa "Mohammed Marouf" Saleh Aref

Supervisor

Dr. Mohammad Suleiman

Abstract

The synthesis of magnesium and palladium core-shell bimetallic clusters (MgPd CSC) was performed with combined salt reduction-electrochemical technique by using a simple electrolysis cell. The surfactant, tetraoctylammonium bromide (TOAB) was used as stabilizing agent to prevent the agglomeration process and as an electrolyte for electrochemical cell.

As-prepared clusters were characterized by using FT-IR, SEM, TEM, XRD, EDX, AAS and UV-Vis spectroscopy to probe clusters' surface, size, structure, shape, morphology, and optical properties, respectively.

The hydrogen storage capacity of the as-prepared clusters was investigated from both points of view "thermodynamic and kinetic" by using the gravimetric and volumetric techniques.

The characterization of the as-prepared clusters confirms the success in preparation of core/shell bimetallic clusters with Mg- rich core and Pd-rich shell with fcc crystalline structure and size near to mono-distribution and ranging from 1.5-4.5 nm, which increases as the current density decreases or the concentration of Mg-core increases.

The optical properties of the as-prepared clusters were performed by using UV-Vis spectroscopy, which shows a blue shift for the surface plasmon resonance with lowering the ratio between Pd-shell and Mg-core. The band gap energy (E_g) of clusters was calculated and found to be core to shell size dependent in the range (3.0-3.3 eV).

As-prepared clusters show a large enhancement "approximately 2 folds" for the hydrogen storage capacity from Pd clusters reported in literature, with reliable kinetics and reversible absorption-desorption processes. Where, as-prepared cluster with size ca. 3.5 nm and metallic stoichiometry of Mg_1Pd_3 formula absorbed the maximum amount of hydrogen (ca. 1.22 wt %) at ambient conditions "1bar and 25°C" during few minutes and desorbed all amounts of absorbed hydrogen again, effectively within absorption time.

CHAPTER (1)

INTRODUCTION

Hydrogen is a colorless odorless gas as well as the most existent element in nature [1, 2]. Its abundance as H₂ gas is low, but it often exists as attracted hydrogen with other elements "carbon and oxygen", i.e. hydrocarbons and water, the vital gradients of whole organisms in this environment [2, 3].

Hydrogen can be produced easily through direct processes by using sustainable sources, i.e. bio-organisms or photo-catalytic-semiconductor cells for water splitting [3-6], or through indirect processes, i.e. thermal processing of biomass or fossil fuels [6]. These and because of its energy is efficient with no harmful emissions compared with fossil fuels [2, 4, 7], hydrogen is considered the most promising ideal material of alternative renewable sources of coming energy [1, 8-10].

Hydrogen energy is the most important source of coming energies. Unlike, it has many drawbacks and obstacles in implementations. The utilization of hydrogen as a sustainable energy source still requires many technologies, including: the effective processes and systems for hydrogen generation [4, 8], purification, energy conversion to electricity [11] and fundamental hydrogen storage systems [1, 9].

Mainly, there are three available systems "manners" for hydrogen storage (H-storage); as a highly compressed gas, cryogenic liquid and "chemically or physically" storage in solid materials [9, 10].

The liquid state and highly compressed H-storage manners cannot reach the proposed target by US-Department of Energy (US-DOE) because of several aspects, e.g. their storage carriers with significant weight, expenses and unreliable conditions for hydrogen storage as well as the low storage capacity and many other safety risks. Therefore, a rising attentions have been focusing on "chemical or physical" H-storage by solid materials that can store the hydrogen effectively at ambient conditions [1, 7, 9-15], e.g. carbon nanotubes (CNT), metal organic frameworks (MOF), metal hydrides, complex metal hydrides, molecular sieves ...etc. [1, 2, 12, 16-18].

Recently, the science known as nanoscience has extreme performances in this field of the H-storage technology and its economy; through synthesis of nanosized materials with remarkable and extremely different physicochemical properties than bulk-materials of the same components [19, 20]. Particularly, the relative surface area of nanosized materials that is extremely larger than bulk-materials [19-21], which is the most vital feature for improvement the H-storage capacity [18].

This chapter will be two sections; section 1.1 will touch on topic of metallic nanoparticles, their properties and preparations perspectives. Thereafter, in section 1.2, an introduction about hydrogen storage technology with focusing on hydrogen-metal (H-M) systems will be mentioned.

1.1 Introduction to Nano-Sized Materials

1.1.1 Nanoscience and Nanotechnology "General Perspective"

Nanoscience is the science refers to the control and manipulation of the matters' sizes and shapes that was made of composites in nano-scaled diameters [20-23, 25-28]. On the other hand, nanotechnology can be defined as the science that refers to how these matters can be employed and exported in the best economic opportunity to the civilization of mankind [23]. Nanotechnology was emerging in few decades ago and its revolution reached the peak at 20th of 1st mid-century after the unique properties of these nanosized composites have been discovered [22, 23].

The term "Nano" is an expression refers to the *Latina* word of ($\nu\tilde{\alpha}\nu\omicron\varsigma = \text{Nanus}$) has a meaning of Dwarf [29]. "Nano" is a scale corresponds to one billionth of meters (10^{-9} m) [23]. Nano-materials are materials made of nanosized particles with size around 1-50 nm [21, 30], and often literary from 1-100 nm [23-32].

All the nano-structural materials, i.e. clusters, fibers and thin films ... etc. have been attracted a considerable attentions, due to their remarkable properties as well as technological applications in the present technologies [33-35], i.e. catalysis, optical devices, chemical and biological sensors and photo electric cells, in addition to its applications in medical, environmental and coming energy technologies [20, 28, 31, 34, 36].

1.1.2 Nanosized Materials "Properties and Classifications"

Matters made of nanosized composites have a high scientific and technological interests, because of their remarkable macroscopic "physicochemical" properties that are superior to their bulk materials [33, 34, 38], i.e. mechanical (hardness, and corrosion resistance), optical, magnetic, catalytic and thermal properties [22, 26, 32, 37, 39].

Nanosized particles and their properties mainly depends on the size and crystalline structure "crystallites and inter-grain boundaries" [32-34]. Nanosized particles have sizes between atomic and bulk. Therefore, their own properties are size dependent [36, 22]. Where, their behaviors and actions become quantized as their size decreases, in phenomenon of "quantum sized effect" [26, 33, 37].

In nanosized particles, the bands theory of solid has inconvenient features because of the decreasing in the number of aggregated atoms, which leads to rise the gaps between their energy levels, as shown in figure 1.1, as well as the varying in their electric conductive properties [39], This phenomenon is known as "energy level quantization" [33, 35, 37].

In another way, nanosized particles have size dependent optical properties, due to the variation in the mobility electrons located on (or near) to the surface (interface) with varying of their sizes [27, 35, 37, 40].

Metallic nanosized particles almost show characteristic phase behaviors that lead to the lowering of their melting points and spontaneous alloying [19].

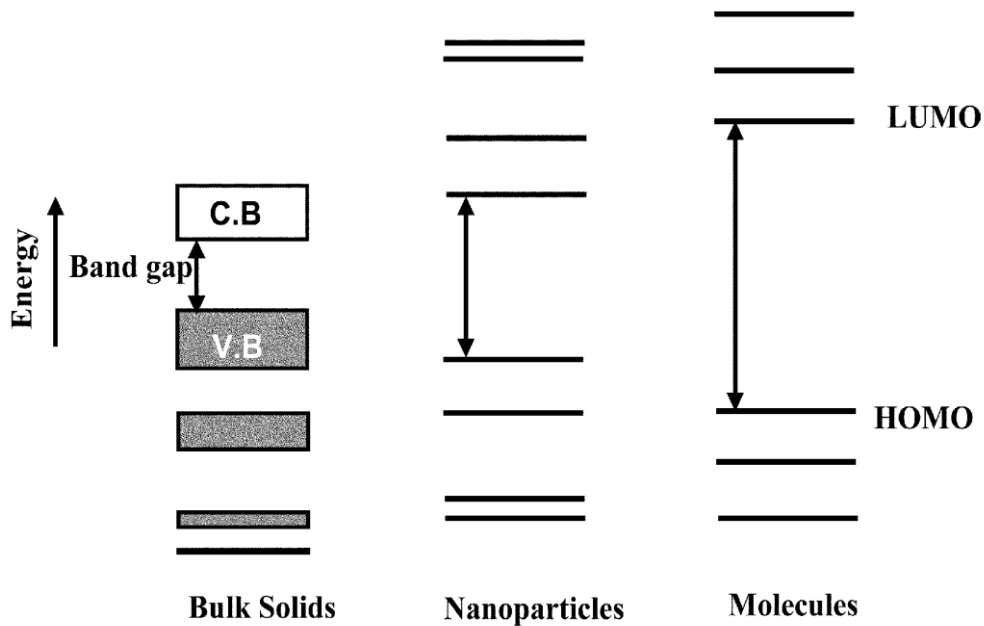


Figure 1.1: Schematic image describes the difference between energy levels of the bulk, nanoparticles and molecules. [35].

One of the most characteristic properties of nanosized particles is the vast increasing in their relative surface area "surface to volume ratio" [22, 23, 28, 42], which earning them synergistic behaviors in comparison to bulk, table 1.1 shows how the percent of surface atoms (N_s) increases at less sized particles. However, nanoparticles have great stresses "surface tensions" and thermodynamically instable for their surface atoms, due to the large excess of Gibbs free energy (ΔG) in comparison with the atoms are located in bulky (lattice) for each single nanosized particle [24, 27, 39].

Surface tensions of nanosized particles increase with decreasing the size because of the rising in the number of unoccupied surface atoms [20, 21,

26, 27]. These stresses on the surface are rapiers; it makes the synthesis of particles with nano-scaled size bit hard and requires specific techniques and ligand-protecting shells to prevent the agglomeration process [40]. Otherwise, This earning these particles some unique attributes, i.e. catalytic activity and high reactivity with their surrounding molecules and gases, i.e. H₂-gas [5, 28, 39, 41].

Table 1.1: Summary of the number of surface atoms and shows how the percent of surface atoms increases at less sized GaAs nanoparticle. [20]

n	Size [nm]	Total number of atoms	Number of surface atoms	% of surface atoms
2	1.13	94	48	51.1
3	1.70	279	108	38.7
4	2.26	620	192	31.0
5	2.83	1165	300	25.8
6	3.39	1962	432	22.0
10	5.65	8630	1200	13.9
15	8.48	2.84 x 10⁴	2700	9.5
25	14.1	1.29 x 10⁵	7500	5.8
50	28.3	1.02 x 10⁶	3.0 x 10⁴	2.9
100	56.5	8.06 x 10⁶	1.2 x 10⁵	1.5

Nanoparticles can be classified in accordance to the type of their components, shapes and dimensions. The nanoparticles can be classified as organic or inorganic nanoparticles according to their components type [20, 22].

In accordance to the shapes type, nanoparticles can be classified into: quantum-dots, nanowires, nanotubes or as rods, spherical ... etc. [20, 26]. According to the dimension, they can be classified into zero (e.g. quantum-dots and clusters), one (e.g. Nano-fibers) and two-dimensions (e.g. layered-structures and thin-films) [27].

Nanoparticles with size lower than 10 nm (~100 atoms) with narrow size-distribution can be called clusters [21, 42]. The clusters are considered the excellence novel materials because of their remarkable small and mono-dispersed size.

The properties and stabilities of clusters "particularly, metallic clusters" mainly depend upon the type and number of the building blocks (nuclei and electrons) [38].

The number of atoms on the surface and the finite spacing between electronic energy levels of the clusters are the key of their unique properties and stabilities. It was found that, clusters with geometric or electronically closed shell configuration "when the number of delocalized electrons on the clusters' surface is equivalent to the valence electrons that required filling an electronic shell" are the most stable and abundant

clusters ever observed. Recently, are known in the term of "*Magic number*" [5, 38].

The composed clusters from alkali and noble metallic atoms, the identification magic numbers are 2, 8, 18, 20, 34, 40, 58 ... etc. of atoms, which corresponds to the valence electrons of constituent atoms. Whereas, in transition metallic (TM) clusters, the magic numbers are 7, 13, 15, 19 ... etc. of atoms, which corresponds to the number of surface atoms depending on their symmetric and geometric structure, as shown in figure 1.2 for gold (Au) and Titanium (Ti) clusters, respectively [38].

Originally, the full shell clusters observes a hexagonal or cubic closed packing with first magic number for clusters built of 13, 55, 147, and 309 atoms [5, 42]. The relation between the number of atoms and shells with their related size (in diameter) for cubic closed packing clusters was obtained by Jellium model [42], which is summarized in table 1.2.

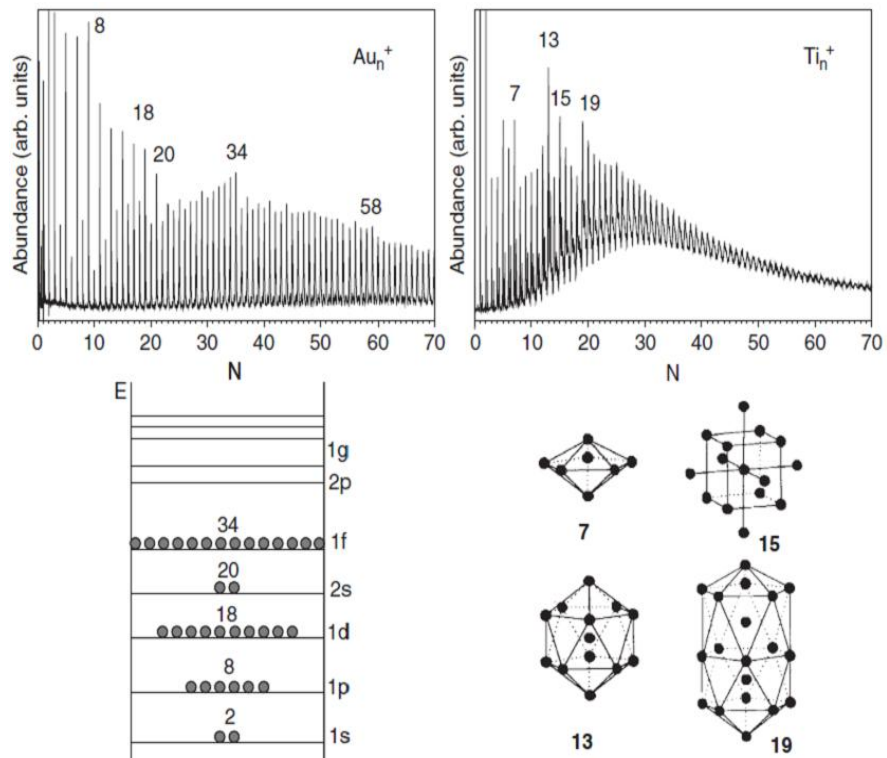


Figure 1.2: Mass-abundance spectra of gold (left) and titanium (right) clusters, showing electronic and geometric magic numbers, respectively. The lower panel shows a schematic representation of the sequence of spherical electronic shells, as it applies to gold clusters, and a number of small symmetric geometric structures, which apply to titanium clusters. [38].

Table 1.2: The relation between the number of atoms in Pd-cluster with "cubic close packing" of n-shell with the No. of surface atoms (N_s), whole No. of cluster atoms (N) and cluster size in diameter (d). [43]

n	d [nm]	N	N_s
1	0.7	13	12
2	1.13	55	42
3	1.56	147	92
4	2.00	309	162
5	2.44	561	252
6	2.88	923	362
7	3.33	1415	492
8	3.77	2057	812
9	4.21	2869	1002
10	4.65	3871	1212
11	5.09	5083	1442
12	5.53	6525	1692

1.1.3 "Mono and Bimetallic" Nanoparticles and Clusters:

Metallic nanoparticles and clusters can be composed from one or two different metals (mono and bimetallic clusters, respectively). They have been attracted a great interest in the wide range of science and technology. Particularly, bimetallic clusters which attracts more and more attentions, not only for their quantum-sized properties but also for their composition tunable physicochemical properties [36, 41, 44].

In 1857, the first metallic nanoparticles were prepared by Faraday, who prepared a solution of dispersed gold (Au)-colloids with size about 3-30 nm by using a chemical reduction method. In 1988, these sizes were confirmed by Thomas [45, 46]. Thereafter, in 1951, Turkevich et al. prepared an aqueous solution dispersed Au-colloidal nanoparticles by reduction technique of Au-ions with phosphorous or carbon monoxide, and then he published a significant paper about the colloidal nanoparticles of their mechanisms and preparation methods [47, 48].

In 1970, the first bimetallic nanoparticles were prepared from Pd and Au with different structural compositions by J. Turkevich and G. Kim, which was performed with sequential reduction method and the citrate was used as reducing agent [49]. Thereafter, the idea was further developed by Toshima's group, who used PVP to stabilize 1–3 nm bimetallic Pd-Au clusters [50].

Bimetallic nanoparticles can be categorized based on its metallic arrangements into four main types: Random-alloys, cluster in cluster, core/shell (CS) and inverted core/shell morphological structures, which are shown as models in figure 1.3 [41].

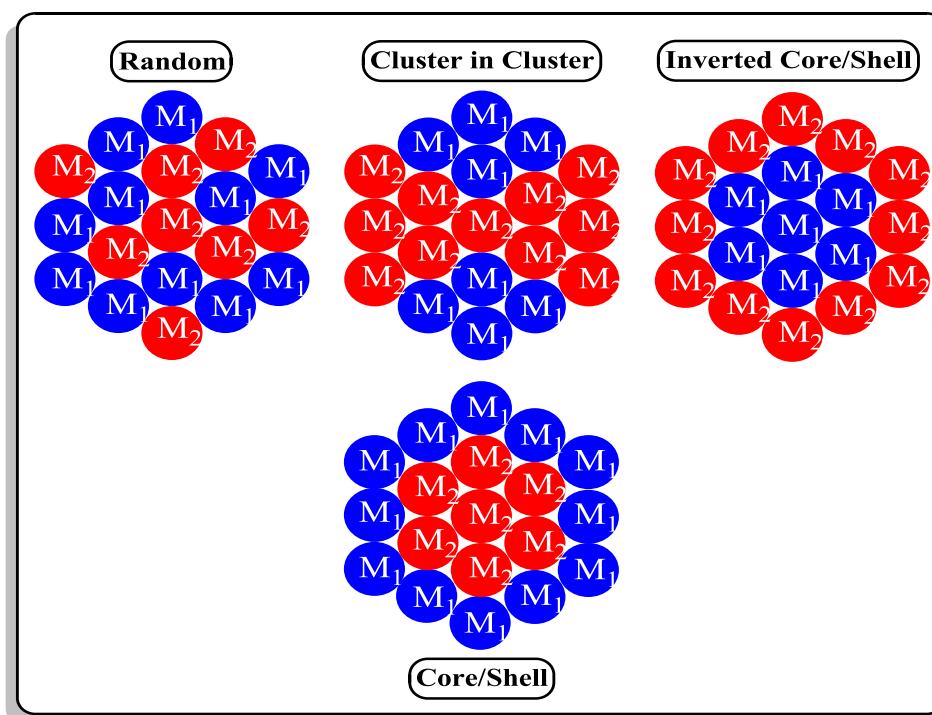


Figure 1.3: Schematic image describes different morphological structures of bimetallic nanoparticles by models.

The most interesting in bimetallic nanoparticles are their modifying and synergistic properties [40]. Sometimes, the properties of bimetallic nanoparticles "particularly, CS-type" are quite different from their individual metallic components, as well as their properties can be modified by manipulating of their shapes and metallic composites ratio. These make them highly functional materials [26, 41].

The modifying in CS-type nanoparticles may lead to increase their surface stability, and functionality. Sometimes, they are modified to protect metal-core from outside reactants and environments, i.e. from corrossions. Farther to its improved properties, CS-type can be used to reduce the consumption through lowering of the used precious materials by coating them with other inexpensive materials [26].

Most of metals, particularly TM's and noble metals can be used to form CS-type. Table 1.3, summarizes the different types of bimetallic clusters and some of their preparation conditions and characterization techniques was reported in literature.

Different selective techniques have been used to prepare CS bimetallic clusters with ability to manipulate their shapes and core to shell ratios [26], as in figure 1.4, i.e. precipitation, grafted polymerization, micro emulsion, sol–gel condensation, layer-by-layer adsorption technique ... etc. [35].

In chemical methods, i.e. chemical reduction technique, the synthesis of CS-type of nanoparticles involves one of these techniques: (i) simultaneous (co-) reduction technique, (ii) or successive (sequential) reduction technique [26, 41]. Although, the simultaneous reduction usually formed bimetallic alloying-type instead of CS-type clusters compared with successive reduction technique [41].

Table 1.3: Typical preparations and characterizations of bimetallic nanoparticles reported in literature. [41]

Metals	Structure	Particle size	Stabilizer	Reducing agent	Analyses
Pt/Pd	-	1.5nm	PVP	alcohol	UV-Vis, TEM, EXAFS
Pt/Ru	Alloys	1.1nm	PVP	H ₂	HRTEM
Ag/Pd	Alloy or core/shell	1-4nm	PVP	Acetone	UV-Vis
Ag/Hg	Alloy	-	Poly(ethylneimine)	NaBH ₄	UV-Vis
Pt/Ru	-	-	-	NOct ₄ (BHEt ₂)	-
Au/Pd	-	-	-	Sonochemical	-
Pd/Au	Alloy or core/shell	22-30nm	-	Citrate	-
Cu/Pd	Alloy	<2nm	PVP	Glycol	XPS, Raman
Ni/Pd	Alloy	1.9nm	PVP	Glycol	TEM, XRD, EXAFS
Au/Pd	Cluster in cluster	-	PVP	Alcohol	TEM, EXAFS
Pd/Ni	Core/Shell	-	PVP	Alcohol	-
Pd/Ag	Core/Shell	-	-	Formaldehyde	UV-Vis
Pd/Pt	Core/Shell	1.5-5.5nm	Polymer	H ₂	CO-IR
Pt/Pd	Core/Shell	1.5-5.5nm	Polymer	H ₂	CO-IR
Ag/Pd	Alloy	-	Stearate ions	Stearic acid	UV-Vis, TEM, XRD
Au/Pd	Core/Shell	-	-	Ethylene glycol	UV-Vis
Pd/Au	Core/Shell	-	PVP	Ethanol	CO-IR, UV-Vis, TEM

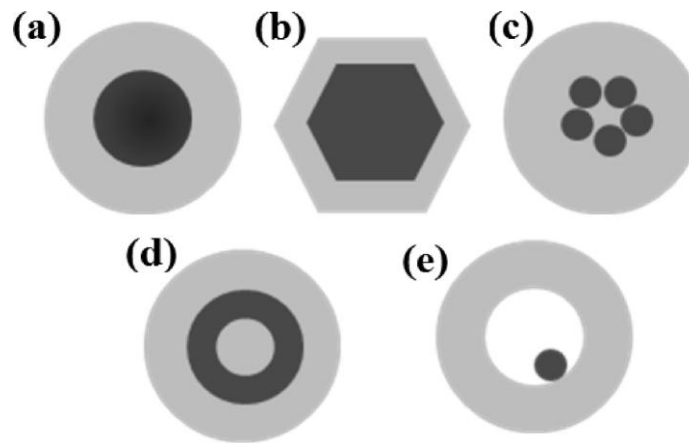


Figure 1.4: Different shapes of core/shell nanoparticles: (a) spherical core/shell nanoparticles; (b) hexagonal core/shell nanoparticles; (c) multiple small core materials coated by single shell material; (d) nano-matryushka material; (e) movable core within hollow shell material. [26]

1.1.4 Methods of Synthesis Nanosized Particles and Metallic Clusters

Recently, there are several advanced manners and techniques for selective preparation of nanoparticles and clusters with manipulating of their sizes, and shapes. For instance, (i) condensation from vapor, (ii) synthesis by chemical reaction and (iii) solid-state processes (e.g. milling) [26, 33].

These different preparation methods and techniques can be classified into two main types: The physical and chemical preparation types [41, 43].

In physical preparation type, it depends upon the physical techniques in preparation of nanoparticles, i.e. grinding, deposition, attrition and milling, without involving any chemical reaction or making changes on their atomic terms.

In chemical preparation type, there is a chemical reaction "almost was described by nucleation and growth" should be involved, i.e. preparation of metallic clusters by salt reduction or electrochemical techniques.

Otherwise, the preparation methods can be divided into: (i) Top-down and (ii) Bottom-up strategies. In top-down strategy, the nanoparticles are produced from bulk materials, which majority depends upon the physical manners, i.e. milling or either of mechanical or photo-radiation attritions. On the other hand, in bottom-up strategies, the nanoparticles and clusters are formed from its molecular terms as starting materials, which often involves a chemical reaction [20, 21].

The chemical techniques are the most extensive technique for preparing mono and bimetallic clusters with mono- size distribution "size variation less than 5%" [51]. Particularly, the salt-reduction and electro-chemical techniques were used because of their simplicity, selectivity and because these techniques saving time and costs [21, 43, 51]. Both of salt-reduction and electrochemical techniques that is known as wet chemical methods, where colloidal nanoparticles will be formed either in aqueous solvent (hydro-sols) or in organic solvents (organo-sols) are mainly depends on the reduction reaction for the desired metal from one of its salts [21].



1.1.4.1 Stepwise Formation of Colloidal Metallic Nanosized Particles and Clusters by Wet-Chemical Methods

The stepwise synthesis and gradual formation of nanosized metallic clusters through using wet chemical methods "salt reduction and electrochemical techniques" were proposed by Turkevich based on three stages: nucleation, propagation "growth" and aggregation, figure 1.5 [21, 46, 48].

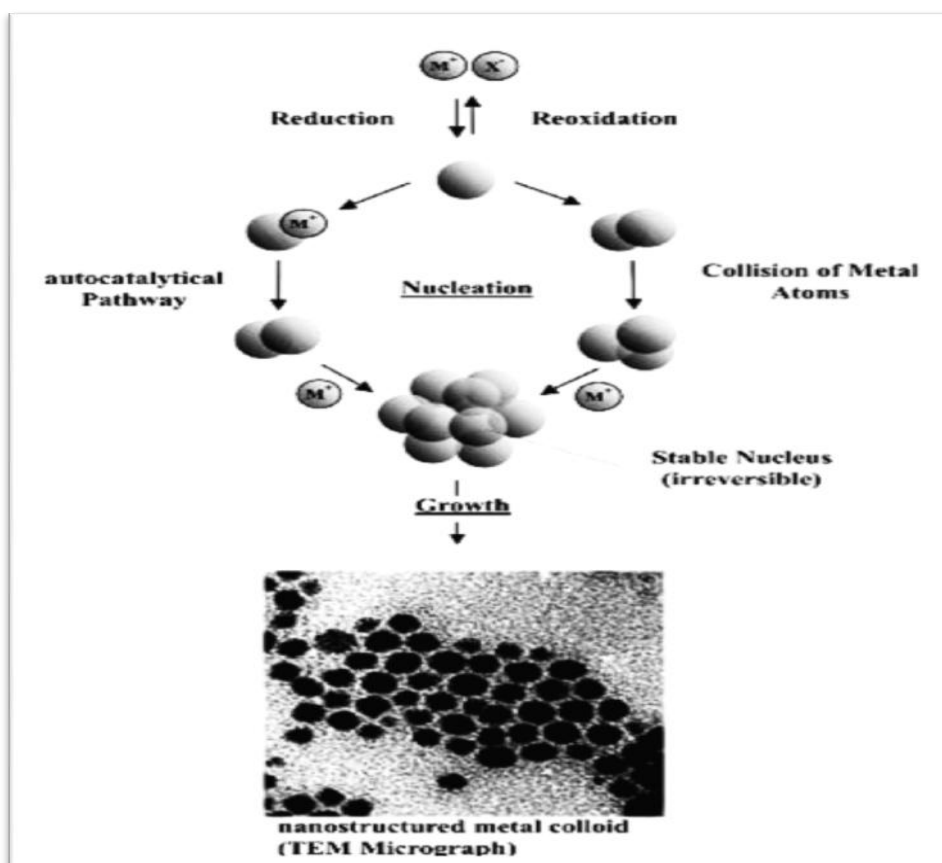


Figure 1.5: Stepwise formation of colloidal metallic clusters by "Wet-Chemical Techniques". [21].

The mechanism and stepwise formation of colloidal nanosized particles and clusters are:

- (i) Reduction of metal salts to zero-valent metal atoms.
- (ii) Nucleation stage, where the metal atoms coalesce with each other to generate sub-clusters almost contains "13 atoms of the full-shell", resulting in formation of stable nuclei, so-called "seeds of growth" [21, 24].
- (iii) Finally, the reduced zero-valent M-atoms were aggregated and grow over the formed nuclei.

The nucleation step has a couple of pathways (trails) to proceed. First, the autocatalytic trail, where metal ions adsorbed and reduced over the surfaces of other formed M-colloids. Second, the collision trail, where the two zero-valent M-atoms collides together within formation a stable nuclei "seeds of growth". These formed nuclei are irreversible and never broken down again to metal atoms

The growth process has a tendency to still in progress even after formation of colloidal metal clusters. Therefore, to save the formed clusters and avoid the agglomerating to bulk, stabilizing agents "stabilizers" are necessary for this purpose, which can prevent undesired agglomeration process by caging the formed clusters and protecting them [24, 43, 52, 53].

1.1.4.2 Stabilization of Colloidal Metallic Clusters

The stabilizing agents "stabilizers" are a composites almost used in wet chemical methods to avoid the undesired agglomeration process by making a protecting shell around the colloidal metal clusters, as shown in figure 1.6. These prevent the growth process through lowering their surface tensions by lowering the surface excess free energy to the formed colloidal particles with process so-called "stabilization" [21, 28, 42, 54, 55].

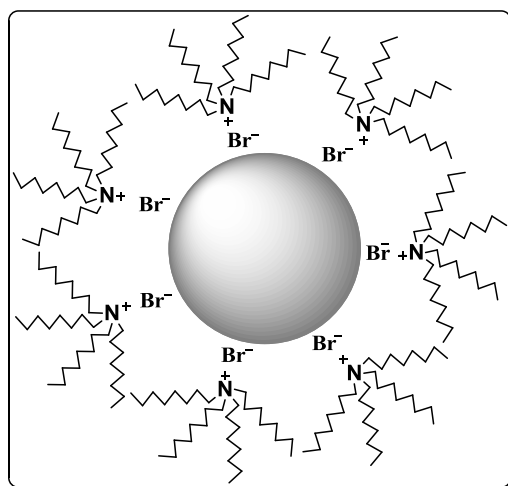


Figure 1.6: Schematic image describes the stabilization of a colloidal metallic cluster by the tetraoctylammonium bromide (TOAB).

Stabilization may effect on the clusters properties and their catalytic activity, because of the significant binding energy between stabilizers and the surface atoms of stabilized clusters [56]. Therefore, the physicochemical properties of the stabilized clusters will be differed from non-stabilized "free" clusters. The using of elastically soft stabilizers will overcome this stabilization disadvantage by the low binding energy of

these soft stabilizers, i.e. tetraoctylammonium halides, which is known as quasi-free stabilizers [43, 57].

The most interested stabilizer for metallic clusters. Particularly, for TM's and noble M-clusters is the TOAB, because of its quasi-free stabilization property and the four symmetrical long chains of (octyl-groups), which lead to form semi-regular spherical shaped clusters [58].

Several types of stabilizers with different stabilization manners were studied, and can be classified into: electrostatic "i.e. Surfactants", steric "i.e. Polymers", free donor ligands "i.e. P, N and S", electro-steric, which have combined steric and electrostatic stabilization manner "i.e. Tetraalkylammonium halides" and solvents "i.e. THF, NaOH and carbonate solvents" [21, 55].

1.1.4.2.1 Electrostatic Stabilization Manner

This stabilization manner depends on the columbic repulsive forces. In which, the formed clusters are protected by an electrical double layer, as shown in the figure 1.7.

The anionic-part of stabilizer interacts with M-cation on the cluster's surface. Therefore, the electrostatic repulsive force between the cations associated with anionic-part of the stabilizer can avoid the formed clusters from agglomeration process [42, 43, 52, 58].

Among of these stabilizers take advantage of the electrostatic repulsive force to stabilize the clusters are: surfactants, donor ligands, and sodium citrate, which firstly was used to stabilize the gold nanoparticles, as mentioned in (section 1.1.3) [47-48].

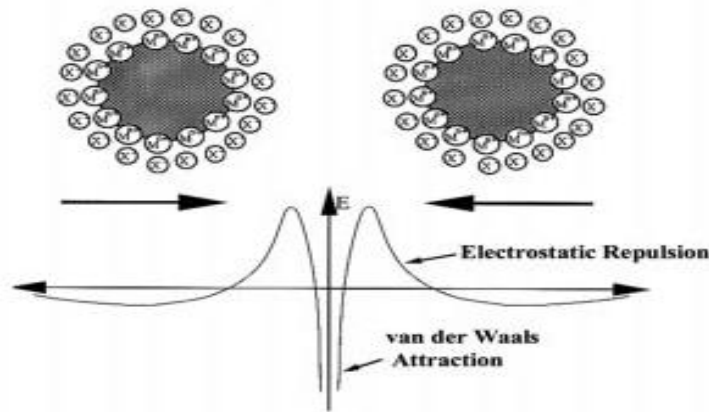


Figure 1.7: Schematic image describes the electrostatic stabilization manner of metallic clusters. [42].

1.1.4.2.2 Steric Stabilization Manner

Among the stabilization manners is the stabilization based on the steric hindrance. Such large molecular weight composites can make a sufficient counter force to the agglomeration process and ceased the aggregating to bulk, i.e. polymers and large molecular weight surfactants, as shown in the schematic image, figure 1.8 [42, 43, 52, 58].

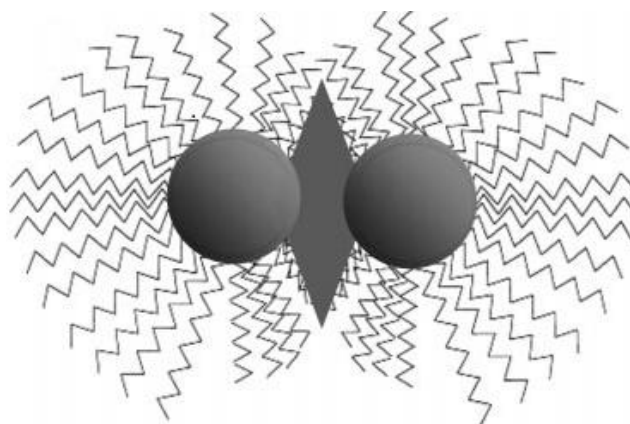


Figure 1.8: Schematic image describes the steric stabilization manner of metallic clusters. [21]

1.1.4.3 Mechanism of "Mono and Bimetallic" Clusters Formation By Electrochemical Technique

Electrochemical preparation technique of M-clusters is very useful, powerful and thoroughly explored by researchers. Since, it is considered as a simple, cheap, and a selective preparation technique for different clusters sizes and shapes. The manipulation process in clusters sizes and shapes can be achieved by changing the preparation parameters, e.g. current density, time, temperature and distance between electrodes ... etc. Moreover, electrochemical technique is the most typical method for metallic clusters preparation with no side products compared with salt-reduction technique and the used reducing agent.

The stepwise formation of M-clusters by this technique is shown in figure 1.9 and can be summarized as:

- (i) Oxidative dissolution of the anodic M-atoms to M-cations.
- (ii) Migration process of M-cations toward the cathode.

- (iii) At the cathode, a reduction for adsorbed M-cations to undissolved zero-valent M-atoms "ad-atoms".
- (iv) M-atoms nucleate and grow to form colloidal small-sized particles "Clusters".
- (v) Stabilization of the formed clusters with a type of stabilizers.
- (vi) Precipitation of the formed M-clusters as solids or powders [21, 40, 43, 52, 58].

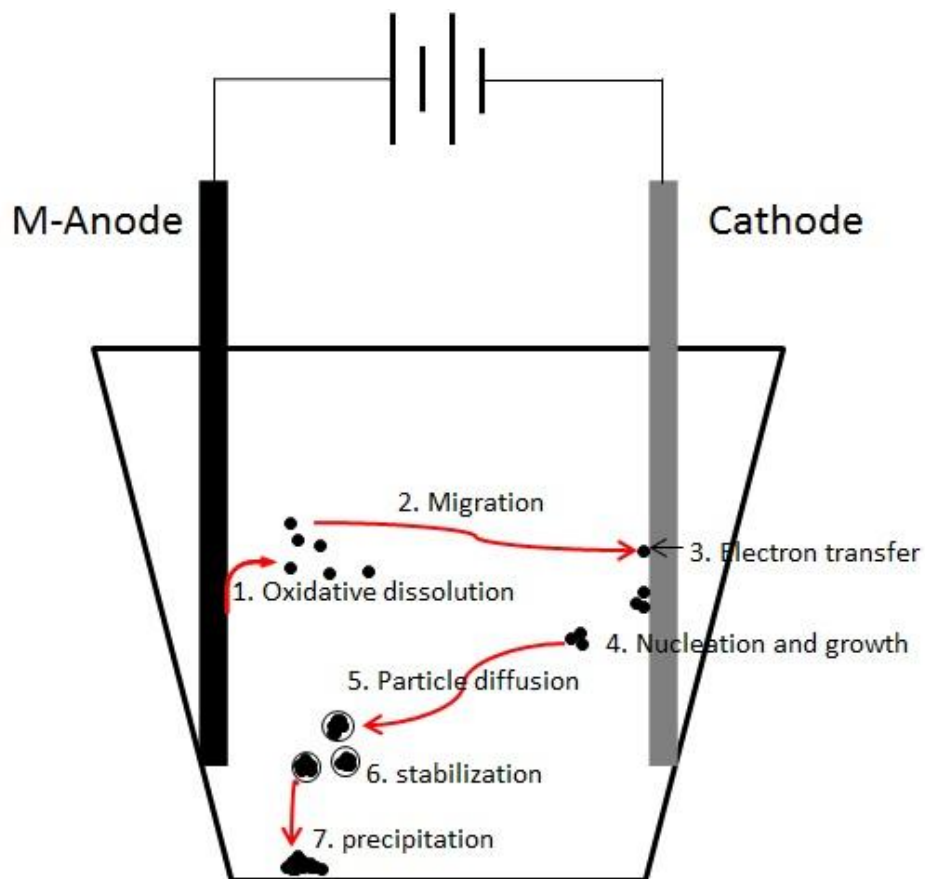
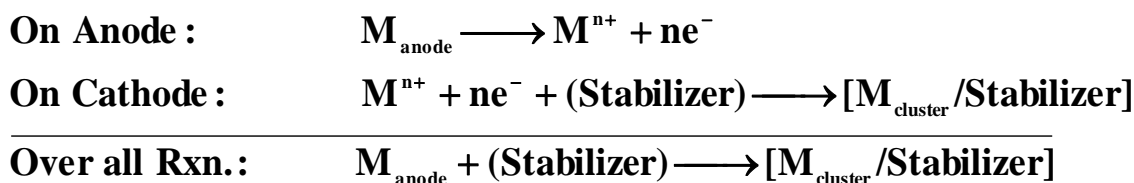


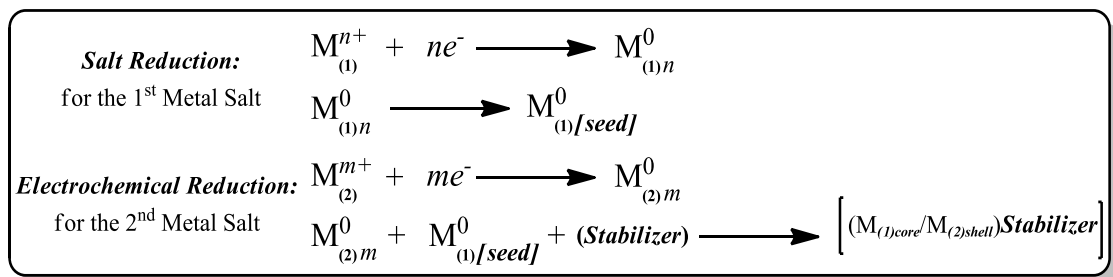
Figure 1.9: Schematic image of electrochemical mechanisms of preparation for stabilized M-clusters.

The overall reactions of metallic clusters preparation can be briefly summarized with the following oxidation-reduction equation [43, 52]:



In another way, the salt reduction technique for preparation of bimetallic clusters with CS-type was almost achieved by the successive reduction of both desired metals from its salts.

Electrochemically, CS bimetallic clusters can be formed, but with a little modification on the electrochemical cell [59], which can be achieved by constructing a more, complicated electrochemical cell with a couple of anodes instead of one. These anodes are composed of the desired metals for clusters preparation. Wherein, first reduced metal served as a seed of growth for the second metal, as represented in the following reaction equations:



1.2 Introduction to Hydrogen Storage Technology

1.2.1 Hydrogen Storage Technology "General Perspective"

In the hydrogen storage technology "i.e. storage carriers", several aspects must be critically concerned, includes: Safety degree, preliminary carrier's weight and storage conditions, economic aspects and spending costs as well as the energy density of stored hydrogen from "gravimetric and volumetric" points of view. These points are evident in the major research themes identified during Battelle's review of nearly 100-hydrogen fuel vehicles (HFV) technical papers and presentations [60, 61].

In accordance to US-department of Energy (DOE), the proposed targets for the different hydrogen carriers to be satisfied for hydrogen technological applications are summarized in table 1.4 [9].

Recently, there are several available strategies and technological manners for hydrogen storage, which can be classified into two classes:

- (i) Physical manners for hydrogen storage, i.e. highly pressurized hydrogen gas, cryogenic hydrogen liquid, and hydrogen storage in some solid materials, such as highly porous materials "e.g. carbon nanotubes and metal-organic frameworks".
- (ii) Chemical manners, i.e. storage of hydrogen in metals, alloys and M-complexes "e.g. MgH_2 and LiBH_4 ".

Table 1.4: The technical system targets of H-storage carriers, based on DOE for Fuel-Cell-Vehicles. [62]

Technical System Targets: Onboard Hydrogen Storage for Light-Duty Fuel Cell Vehicles ^a			
Storage Parameter	Units	2017	Ultimate
System Gravimetric Capacity: Usable, specific-energy from H ₂ (net useful energy/max system mass)	kWh/kg (kg H ₂ /kg system)	1.8 (0.055)	2.5 (0.075)
System Volumetric Capacity: Usable energy density from H ₂ (net useful energy/max system volume)	kWh/L (kg H ₂ /L system)	1.3 (0.040)	2.3 (0.070)
Storage System Cost:	\$/kWh net	12	8
• Fuel cost	(\$/kg H ₂ stored) \$/gge at pump	400 2-4	266 2-4
Durability/Operability:			
• Operating ambient temperature	°C	-40/60 (sun)	-40/60 (sun)
• Min/max delivery temperature	°C	-40/85	-40/85
• Operational cycle life (1/4 tank to full)	Cycles	1500	1500
• Min delivery pressure from storage system	bar (abs)	5	3
• Max delivery pressure from storage system	bar (abs)	12	12
• Onboard Efficiency	%	90	90
• "Well" to Powerplant Efficiency	%	60	60
Charging / Discharging Rates:			
• System fill time (5 kg)	min (kg H ₂ /min)	3.3 (1.5)	2.5 (2.0)
• Minimum full flow rate	(g/s)/kW	0.02	0.02
• Start time to full flow (20 °C)	s	5	5
• Start time to full flow (-20 °C)	s	15	15
• Transient response at operating temperature 10%-90% and 90%-0%	s	0.75	0.75
Fuel Quality (H₂ from storage) :	% H ₂	SAE J2719 and ISO/PDTS 14687-2 (99.97% dry basis)	
Environmental Health & Safety:		Meets or exceeds applicable standards, for example SAE J2579	
• Permeation & leakage	-		
• Toxicity	-		
• Safety	-		
• Loss of usable H ₂	(g/h)/kg H ₂ stored	0.05	0.05

In general, there are three main systems "carriers" for hydrogen storage:

(i) High pressurized H-carrier.

Based on this storage system, the hydrogen can be stored in the gas phase under high pressure into specific manufacturing cylinders, their structure and materials were designed carefully to avoid the leakage of H-gas and

carrier's embrittlement. It is usually made of highly pressurized steel, where hydrogen can be stored at 150 bar (15 MPa).

Recently, it is designed by a shell made of lighter weight matters from carbon fiber-reinforcement resins that are able to load pressures up to 700 bar (70 MPa) and lowering of the carrier's weight as well as the polymer-liner that is used to prevent H-leakage.

H₂-gas storage carriers have excellent gravimetric energy density (about 120 MJ per kg) but its volumetric energy density is poor in comparison to the current used fuels, as shown in table 1.5, which means, a larger carrier's weight, about 110 kg is required to reach the DOE target, the 6% and 30 kg.m⁻³ of gravimetric and volumetric densities, respectively. In addition, about 15% - 18% of the assumed energy content was lost in pressurizing the H-gas as well as their associated large spending costs, and safety aspects that should be taken into account [3, 10, 11, 61, 63-65].

(ii) Cryogenic liquid H-carrier.

The second system for H-storage is storing of H₂ in its liquid phase. This process needs high pressure with very low temperature (~ 20 K) to boil off and liquefying the H₂-gas. All of these requirements for liquefying H₂-gas assume a lot of costs and energy "about 30 % of its total energy content" to achieve, as well as the more complicated and hard handling systems, i.e. designed tanks with large spacing and pressure release valves. Therefore, liquid hydrogen storage carriers is in certain extent, incapable for applying

despite of their high hydrogen energy density compared to highly pressured hydrogen storage systems, as shown in table 1.5 [10, 11, 61-65].

Table1.5: The energy densities (ED's) for different energy storage materials with clarifying some examples and recent uses. [65]

E-Storage Materials	E-Specific (Gravimetric ED) [MJ.Kg⁻¹]	E-Density (Volumetric ED) [MJ.L⁻¹]	Direct Uses
Uranium-235	8.31X10 ⁷	1.55X10 ⁹	Nuclear reactors
Hydrogen (70MPa)	123	5.6	Exp. automotive engines
Hydrogen liquid	141.86	8.491	-
Hydrogen gas	141.86	1.01X10 ⁻²	-
Gasoline (Diesel)	~46	~36	Automotive engines
Propane	46.4	26	Home heating and cooking
Coal	24	-	Electric power plants
Carbohydrates	17	-	Human/animal nutrition
Protein	16.8	-	Human/animal nutrition
Wood	16.2	-	Heating and outdoor cooking
TNT	4.6	-	Explosives
Gunpowder	3	-	Explosives
Li-Battery	1.8	4.32	Portable electric devices
Li-ion-Battery	0.72-0.875	0.9-2.63	Some modern electric vehicles
Super-capacitor	0.018	-	Electric circuits
Electrostatic capacitor	3.6X10 ⁻⁵	-	Electric circuits

(iii) Solid Phase Materials as H-Storage Carriers.

There are several materials are widespread studied and investigated of their hydrogen storage behaviors, which are summarized in figure 1.10.

Solid materials for hydrogen storage can be classified into three main categories: (i) Highly porous materials, like carbon based materials, i.e. fullerene, activated carbon and carbon nanotubes [2, 8], metal-organic framework, and organic polymers [16], (ii) complex hydrides, i.e. lithium borohydrides (LiBH_4) [1, 2] and (iii) interstitial metallic hydride materials like amorphous or crystalline metals and alloys [2, 9]. These materials and others were extensively studied as candidate solids for hydrogen storage [18]. Recently, three of these studied materials are potentially occupied the force in this field, which are: carbon nanotubes, alloys and metal hydrides based materials.

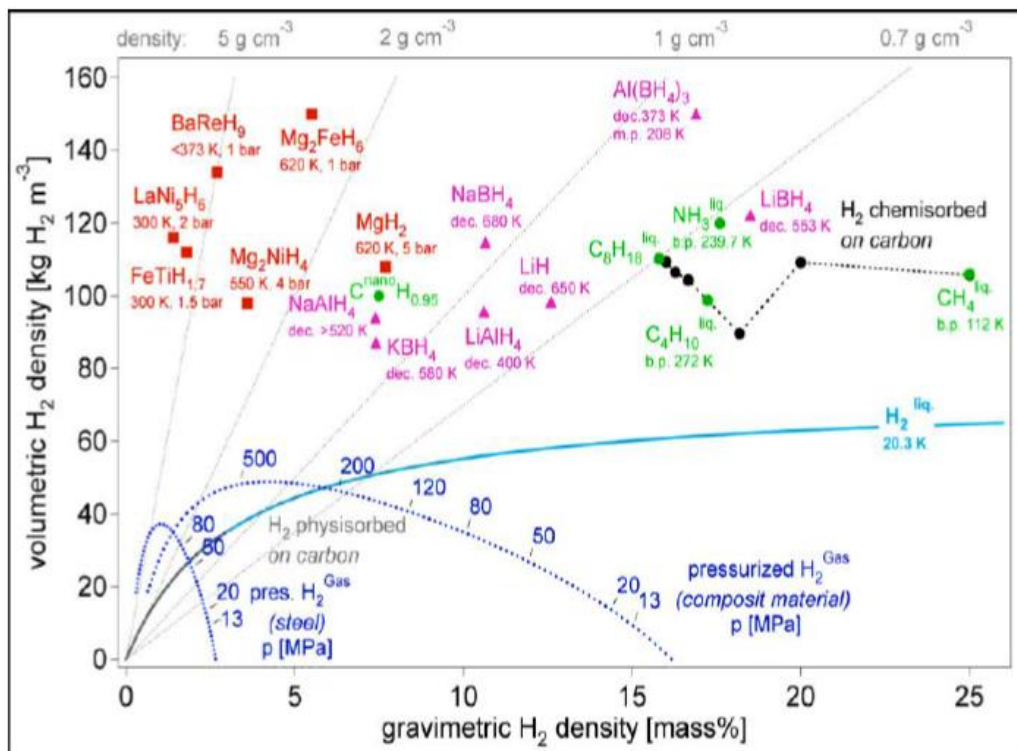


Figure 1.10: The volumetric and gravimetric H-densities for different hydrogen storage strategies and materials. [2]

The solid materials and their H-behaviors "from capacity and reversibility points of view" mainly depend upon the nature of the host solids. This based on two factors:

(I) The interaction type between hydrogen and the host solid.

These interactions ranging between the strong chemical "when the host atoms trapping with H-atoms after the dissociation of H-molecules" and weak physical interaction "when the interaction happened between host solid and H-molecules by van der Waals interaction" [18, 66].

(II) The structural "crystallite" of atoms into host solid.

Typically, the trapping of hydrogen on the host solid can be happened with a process known as sorption "adsorption and absorption", which includes:

(i) trapping of hydrogen with surface atoms of the host solid, almost a physical attraction "adsorption" will be occurred between H and the host-solid, i.e. highly porous materials [7, 16, 18, 67]. (ii) H-penetration inside lattices of the host solid with a process known as diffusion "mainly so-called absorption". In this case, the chemical interaction is the predominant interaction between H and host solid as metallic solids that can absorb H-atoms [67, 68].

In some materials, the adsorption and absorption processes can be happened simultaneously. This can be shown in spongy-like metals, i.e. Pt and Pd metals [67, 69-71].

The capacity and reversibility of these materials to uptake hydrogen depends mainly on the relative surface area and the defects "grains type and shape" along the surface, or on the porosity numbers, shapes and diameters for highly porous materials. Therefore, nano-structural materials were found to have extreme effective and different H-uptake performances than bulk materials. Where, in Pd-nanoparticles, the H-atoms trapped inside their lattices, which lead to form more stable Pd-H bonds than Pd bulk. Otherwise, non-hydride forming metals in the bulk, i.e. Fe, Rh, Pt, Ru and Ir have high H-storage capacity in nanosized structure, due to the nano-sized effect [19, 57].

1.2.2 Metals as Solid Materials for Hydrogen Storage

Most of metals and alloys "particularly, TM's" have a high capacity to uptake hydrogen at proper conditions "pressure and temperature" and the formation of binary ($M_{(1)}H_x$) or ternary ($M_{(1)}M_{(2)}H_x$) or higher metal hydrides with a stoichiometric numbers ($n = 1, 2, 3$) between metal and hydrogen elements [68, 72, 73]. However, most of them can't be affiliated the normal stoichiometry due to the defects in the lattice of their crystalline structures, therefore existed as multiphase systems [2, 72, 74].

The hydrogen atoms or molecules can be trapped on the defect sites (grains, grain boundaries ... etc.) of the crystalline structure for the metallic solids or may be occupied the O_h and T_d sites of the metal lattice to form a nonstoichiometric metal hydrides, known as interstitial hydrides [71, 75-78].

The reaction between the hydrogen and metal "hydriding the metals" can be occurred by two possible routes: First, direct dissociation of hydrogen molecules on the host lattice of the metal "dissociative chemisorption", as shown in the following reaction equation [7, 9]:



In this case, the stability of the formed metal hydrides is indicated by the value of standard enthalpy of formation for the metal hydride (ΔH_f). Where, larger absolute value of the ΔH_f ($\Delta H_f < 0$), means the more stable

hydride was formed. On the other hand, the dissociation of metal hydride was given by (ΔH_d), which has the similar absolute value and counter sign for ΔH_f ($\Delta H_d = -\Delta H_f$).

The temperature for dissociation (T_d) is simply given by the following equation, (eq. 1.1):

$$T_d = \frac{\Delta H^o}{\Delta S^o} \quad (1.1)$$

The direct proportionality is seemed between required dissociation temperature for metal-hydride and the enthalpy of formation, which means the most stable metal-hydrides need a higher temperature to release the adsorbed hydrogen. This is seemed clearly in Mg-H systems with ΔH_f about $-75 \text{ kJ.mol}^{-1}\text{H}$, the T_d is up to $\sim 300^\circ\text{C}$ [79, 80].

The second route was electrochemical dissociation of water molecules [7, 9], as shown in the following reaction equation:



In this case, the metal must be a catalyst, i.e. Pd-metal, to break down the water molecules [2].

The attraction process between H_2 and host-metal lattice is M-surface dependent in accordance to the efficiency of M-surface to dissociate the H_2 molecules into H-atoms as well as the H-mobility "diffusion" into M-lattice. Typically, the absorbed hydrogen with some metals, i.e. Pd, Ti, Zr

and V, can be formed solid solutions. Therefore, the amount of absorbed hydrogen can be described in term of hydrogen solubility [74].

The hydrogen absorption process can be described with simplified one-dimensional potential energy curve for H-molecules and H-atoms when dissolved in M-host, figure 1.11 [81].

The hydrogen molecules (H_2) approach the host-M surface and then physisorbed on the interface of the M-host by van der Waals interaction.

M-host activated the dissociation of the H-molecules to H-atoms by lowering and overcoming the dissociation energy of H_2 ($E_D \approx 218\text{KJ/mol H}$). Therefore, hydrogen atoms chemisorbed at the surface of M-host and the penetration "diffusion" of H-atoms into bulk may endothermically or exothermically happened and the hydride phase can be nucleated and grow.

In Accordance to the curve, the physisorption of hydrogen was ceased at the interface of M-surface as the increasing of their potential energy [82].

The more considerable aspect in metal hydrides is the thermodynamics of hydrogen dissociation and hydride formation, which can be described by pressure-composition-isotherm (PCI).

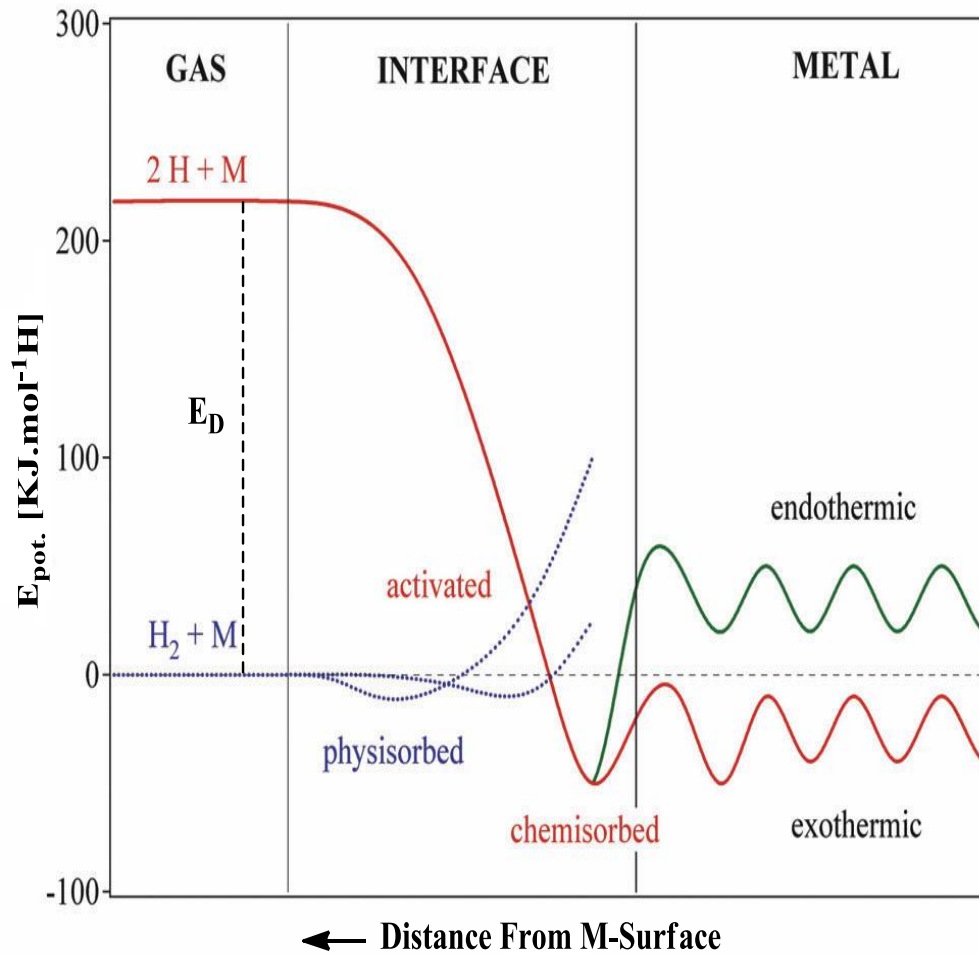


Figure 1.11: One-Dimensional Potential Energy Diagram according to the distance of the hydrogen gas from the metal surface. [72]

1.2.2.1 Thermodynamics of Metal Hydride Formation and Phase Transition

The absorption of hydrogen in the metals often causes some stresses in their crystalline structure. Hence, the expanding of their lattices and sometimes may be grounded to powder in order to lower the stresses and prevent the decrepitating of host metal [30, 57, 83]. Particularly, If two hydrogen atoms recombine to form hydrogen molecule in the interstitial sites, as represented in schematic image of figure 1.12 [7].

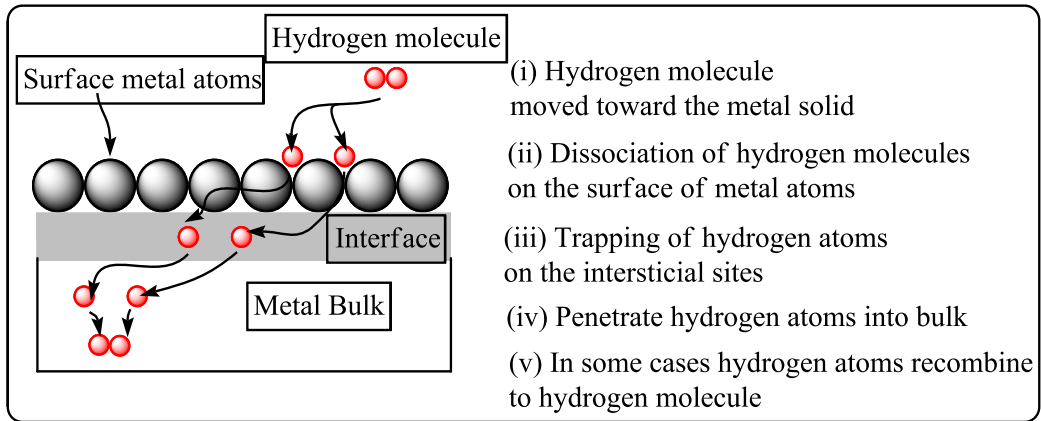


Figure 1.12: Schematic image describes the adsorption and diffusion of H-atoms in the interface and bulk of M-host solid.

In H-Pd systems, the hydrogen absorption process and followed expansion in the metal lattices. Thermodynamically, it passes through three phases. These phases can be described by pressure-composition-isotherm (PCI), figure 1.13, and the related pressure-lattice-temperature isotherm (P/T) figure 1.14, respectively [75, 83-85].

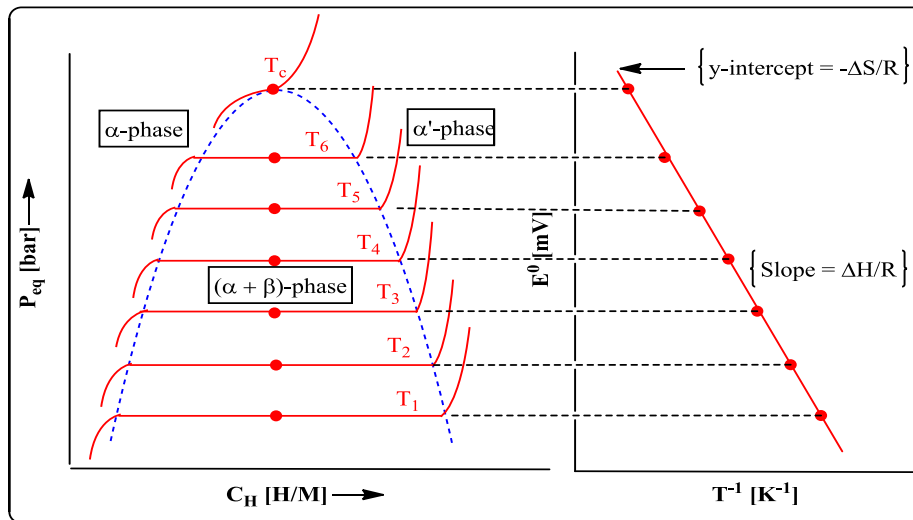


Figure 1.13: Pressure-Composition-Temperature Isotherm (PCI) curves (left hand side) and the resulting van't Hoff plot (right hand side) for thermodynamic metal-hydride formation.

The thermodynamic M-H phases are considered as a description for the metal hydride formation of their stability, H-uptake capacity and H-absorption-desorption reversibility.

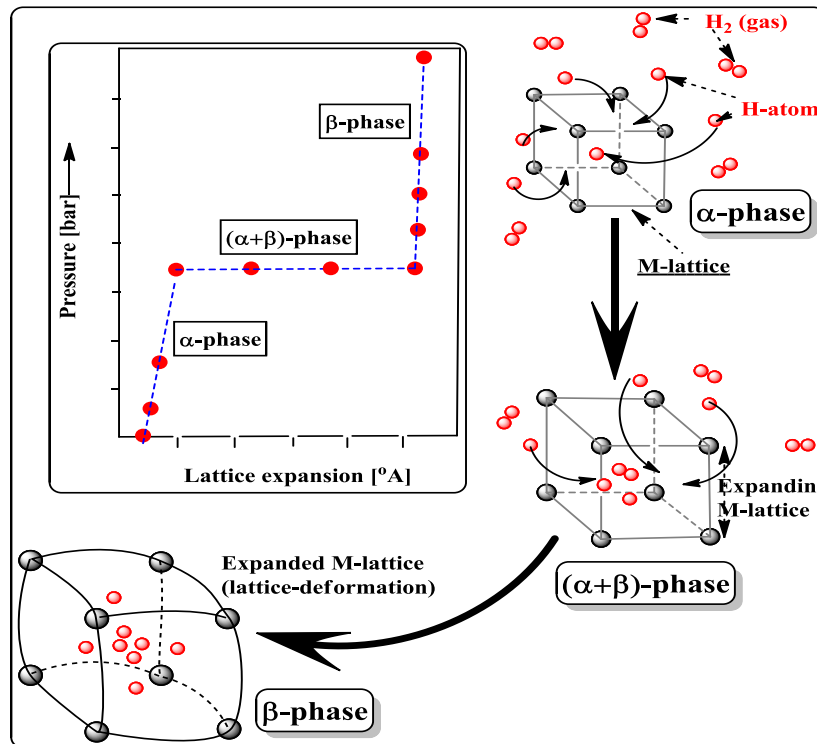


Figure 1.14: The *PIT* isotherm and schematic representative images for the relationship between H-diffusion and lattice constant during absorption of H-atoms.

The three phases in Pd-H system are: (i) α -phase, which corresponds to the anhydride phase "solid solution". (ii) β -phase (or α' -phase, which will be used as donation to the hydride phase instead of β , later) that is attributed to the hydride phase "saturated solid solution". (iii) The transition phase $(\alpha+\alpha')$ -phase "known as miscibility-gap region", where the two-phases coexist, figure 1.13. The two-phase region is the equilibrium phase between anhydride and hydride phases at equilibrium pressure (P_{eq}) [43].

At trivial amount of H/M-ratio (almost < 0.1), H is exothermically dissolved into M-host [72] and the solid solution begins in conformation. In this phase, the expansion of M-lattice is proportional to H-concentration (approximately $2\text{-}3^\circ\text{A}$ per H-atom) [72]. With regard to α -phase region at (PCI), it can be remarked with increasing H-concentration in accordance to pressure increases.

At higher H/M-ratio (almost > 0.1), further H-atoms are dissolved in metal lattice. In this case, the hydride phase is in growing and the interaction between H-atoms in H_2 -gas becomes significant because of the expanding in M-lattice. In PCI, it can be remarked as plateau between α and α' -phase regions and no pressure dependence on H-concentration. Actually, the width of miscibility-gap region " $\alpha+\alpha'$ -phase region" is the determinant region for the solubility and reversibility in formation of the Pd-H system [66].

Further increasing of H-concentration in the M-lattice and at H/M-ratio approximate to 1, the saturated solid solution " α' -phase" is achieved and in PCI the pressure increases steeply with increasing H-concentration in the M-host [82].

The two-phase region is temperature dependent and ends at critical point (T_c). Where, at higher temperature than T_c , the transition between the solid solution (α -phase) and saturated solid solution (α' -phase) happened immediately [57, 84, 86-88]. The T_c value is lowered at less sized particles,

which was obtained by A. Zuttel et-al. for H-Pd systems, as well as found by M. Yamauchi [30, 84].

In the PCI, the P_{eq} corresponds to the changes in the enthalpy (ΔH) and entropy (ΔS) in hydride formation, as a function of temperature that can be expressed by the van't Hoff equation (eq. 1.2):

$$\ln\left(\frac{P_{eq}}{P_{eq}^o}\right) = \frac{\Delta H}{RT} - \frac{\Delta S}{R} \quad (1.2)$$

Where, ΔH is the enthalpy of formation in ($\text{kJ.mol}^{-1}\text{H}$) of H_2 , ΔS is the entropy of formation in ($\text{J.K}^{-1}.\text{mol}^{-1}$) of H_2 , R is the gas constant and T is the absolute temperature.

Dependent on van't Hoff equation, the changes in entropy (ΔS) define the variations on the hydrogen phases "from H_2 -gas to dissolved H in M-solution". On the other hand, enthalpy (ΔH) defines the stability of the formed metal hydride.

In another way, the H-desorption process is similar to absorption-process and includes the three thermodynamic-phases, as shown in figure 1.15, the schematic image for the H-absorption and desorption in M-host.

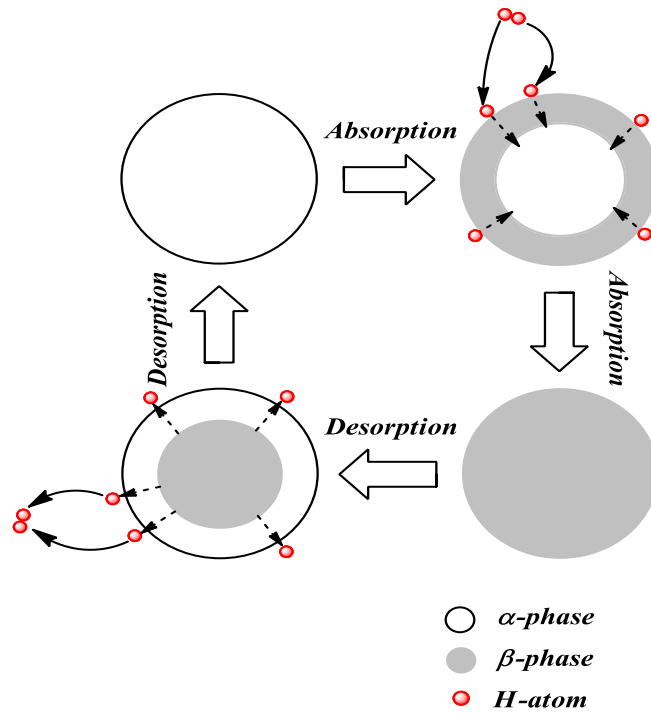


Figure 1.15: Schematic image describes the phase transition for M-H system and their stepwise of phase-transitions for H-absorption and desorption processes.

The PCI for desorption process often do not matches the PCI for absorption process at the two phase region "miscibility-gap region", as shown in figure 1.16. Where, the absorption happened at higher P_{eq} than desorption process. The difference between absorption and desorption-pressures is called hysteresis [89] and it is given as the following equation (eq. 1.3):

$$\mathbf{Hysteresis} = \ln\left(\frac{P_{abs}}{P_{des}}\right) \quad (1.3)$$

Where, P_{abs} and P_{des} are the equilibrium pressure for the absorption (hydrogenation) and desorption (dehydrogenation) of the M-host, respectively.

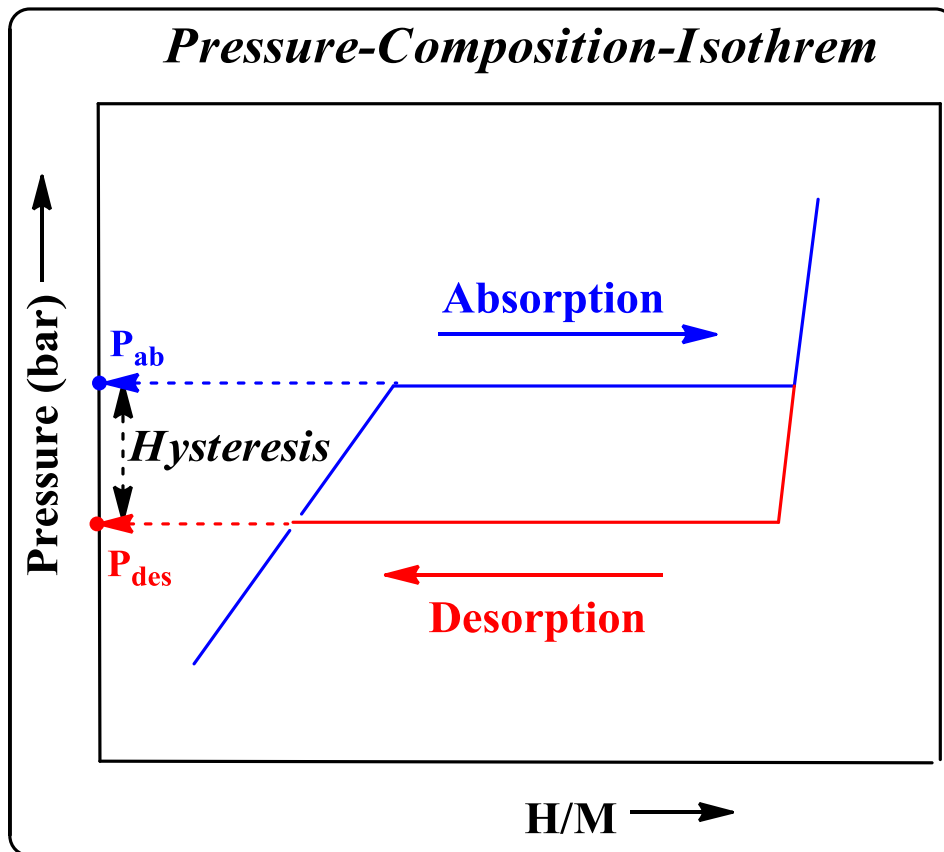


Figure 1.16: Hypothetical (PCI) for both H-absorption (blue curve) and desorption (red curve) processes that clarifies the Hysteresis.

In bulky metals, the hysteresis is usually explained as strains' reasons "Misfit deformation" on the M-host crystallite due to the expansion and relaxation of the M-lattice during the hydrogen absorption and desorption processes [57, 90, 91]. Unlikely, this explanation is not acceptable for nanosized clusters because the generation of misfit deformation in bulk needs up to 4 nm in size. This makes it invalid with small clusters [91].

The hysteresis in nanosized clusters was explained by Schwarz and Katchaturian as the result of differences in chemical potentials during hydrogen loading and unloading in Pd-H systems, which was the reason behind the formation of hysteresis loops [57].

In practical situations, the two phase region shows a bending "slope" into miscibility-gap region. Unlikely, it was still with no clear explanations except with several speculations:

- Because of the broad cluster size distribution and their variety of bend surface energy contribution, which was explained by E Salomons et-al. [92].
- Based on the site-energy distribution "different chemical potentials" of H-atoms through different mechanical stresses in the M-host [57, 91, 93].
- The stresses between the cluster and its externals i.e. stabilizers and surfactants, which have a different mechanical stresses during H-loading [57].

1.2.2.2 Kinetics of Metal Hydride Formation

H-storage capacity is often measured thermodynamically by the PCI in terms of H-weight per weight of hydride, which expressed in (H_2 wt %), or with the most fundamental term of the number of H-atoms per M-atoms as (H/M), which is the most interests because it is earned stoichiometric information about the formed hydrides.

In another way, the identification of the H-kinetic behaviors is the key of their reliability determination and if the metal hydride can be used in virtual applications [66].

In general, kinetics is defined as time dependent reactions. In metal hydride systems, the kinetic is the (rate) or required time for such metal to absorb (or desorb) amount of hydrogen "Metal hydride formation or deformation" [80].

Metal hydride "gas-solid reaction" kinetics is described by the following equation (eq. 1.4) [80, 94]:

$$\alpha(\tau) = 1 - e^{-(k\tau)^n} \quad (1.4)$$

Where; $\alpha(\tau)$ is the rate of reaction (transformed fraction for MH), τ is the time, k is the rate constant and n is the reaction order.

The rate constant is a temperature dependent term as the following equation "Arrhenius Equation" (eq. 1.5):

$$k = A e^{\left(\frac{-E_a}{RT}\right)} \quad (1.5)$$

Where; E_a is the activation energy, R is the gas constant and T is the temperature.

The activation energy (E_a) may be determined by obtained the α vs. time at variant temperatures, fitting k in the rate equation and plotting $\ln(k)$ vs. reciprocal temperature. Thereafter, the E_a value will be determined from the slope [80].

1.2.3 Experimental Techniques for Hydrogen Absorption/Desorption Measurements

There are two primary manners in measuring the potential of hydrogen absorption–desorption on metallic material, includes: Gravimetric and (ii) Manometric "Volumetric" manners [95].

In gravimetric manner, microbalance apparatus is the used setup for this purpose (details will be mentioned in chapter 3). The principle of this manner is the monitoring of the weight differences in the analyzed material, which are corresponding to the weight of hydrogen absorbed or desorbed at certain pressure values.

In another way, the fundamental principle for the volumetric manner is the monitoring of H-pressure changes in a system with fixed, known volume and temperature. This system is known as "Sievert's apparatus. Based on ideal-gas law (eq. 1.6) the weight of absorbed or desorbed hydrogen can be easily calculated [96].

$$PV = (nZ)RT \quad (1.6)$$

Where, P is the pressure, V is the volume, n is the number of moles, Z is the gas compressibility, R is the universal gas constant and T is the temperature.

CHAPTER (2)

LITERATURE REVIEW

2.1 Palladium as Hydrogen Storage Material

Palladium is one of the most promising metals for hydrogen storage. It was the first M-H systems have been investigated and studied since (1866) by Grahame [97].

Pd-metal is able to absorb up to 900 of its own volume of hydrogen at proper conditions (25°C and 1atm pressure) [87, 98]. It has also a remarkable reversibility for the hydrogen Absorption/desorption processes. Where, Pd uptake and release hydrogen more like the sponge when soaks water up and extract all amounts of the soaked water back again effectively [98]. For that, Pd-metal has undergone extensively in studies not only as H-storage system, but also as a catalyst for hydrogenation and dehydrogenation reactions [9, 99, 100] as well as sensing material for hydrogen in H₂ gas-sensors applications that was studied by Jin-Seo Noh et al. and Shih-Wei Tan et-al. [101, 102]. Moreover, the attractive properties of Pd-H system have extensively studied in regard to PdH_x formation and their physical thermodynamic and kinetic properties [87, 88, 103-105].

Thermodynamically, the hydriding of Pd-metal transformed through three-phases; anhydride phase (α -phase), transition phase ($\alpha+\alpha'$)-phase and the hydride phase (α' -phase), which was firstly, obtained by F. A. Lewis [86].

Palladium metal often forms a nonstoichiometric hydride ($\text{PdH}_{0.6}$) with gravimetric capacity (H/Pd) about 0.56 wt % [30, 84, 87]. This quantity enhanced up to 1.05 ± 0.01 wt % in the hyperstoichiometric hydride ($\text{PdH}_{1.12}$), which was formed at huge pressure (~ 1.6 MPa) and ambient temperature 298 K that was obtained by Sami-ullah Rather et al. [106].

Pd-H systems extensively studied for more understanding of the hydrogen diffusion mechanism and their impacts on Pd-crystallite during hydrogen absorption/desorption processes as well as the stability of Pd-hydride formation. These efforts have been started since 20th century, which was pursuit to understand the mechanisms of H-absorption and diffusion in Pd-H systems.

In 1995, it was found that the energy of H-H and H-M interactions is the main factors of the H-absorption and diffusion processes. Moreover, the H-atoms are preferably occupied the two neighbor O_h -sites for Pd-crystallite that were studied by B. Kang and K. Sohn [70]. In 1996, they also found that the hydrogen occupied 1/3 and 1/2 on surface and sup-surface layers, respectively [71].

In 1997, the grain size and grain boundary impacts on the H-diffusion in nano-crystalline Pd-clusters were studied by U. stuhr et al. They also assigned the high and fast H-diffusion in small sized-clusters to the increase of the volume fraction for grain-boundaries, which was also the

main impact to the narrowing of miscibility gap with size decreasing or temperature increasing [75].

Moreover, the lowering of the miscibility gap region with temperature increases for H-Pd systems; the same results were confirmed by M. Yamauchi et al, in 2008. Where, a stabilized nanosized Pd-particles was studied. In 2010, same results were obtained through studying a prepared Pd-cluster through spark-discharged technique [84, 107].

M. Yamauchi et al. found that the equilibrium pressure and T_c is lowered with decreasing the clusters size. Hence, a more stable hydride was formed than the larger sized particles. Where, ΔH_f and ΔS for Pd clusters with 2 nm size are $-34.6 \text{ kJ.mol}^{-1}$ and -83.1 J.K^{-1} , respectively, which are more stable hydride than 14 nm sized clusters with $\Delta H_f = -31 \text{ kJ.mol}^{-1}$ and $\Delta S = -67.3 \text{ J.K}^{-1}$ [84].

In 21st century, researches were turned to study the H-diffusion and absorption-desorption cycles' effects on the crystallite of Pd-clusters and their lattice expansion, most of these works were investigated by in situ XRD pattern. This, through the distinction between d-spacing of diffraction patterns during the H-loading or unloading on Pd-H systems and their constructed P/T isotherms. In addition to several other attempts to explain the hysteresis and slopes in miscibility gap by small sized clusters and the impacts of stabilizers types on the surface of prepared clusters and then on H-absorption, diffusion and on the crystallite expansion during H-loading.

These attempts have begun by A. Zuttel et-al. (1999), M. Suleiman et al. (2003, 2005), A. Pundt et al. (2004) and D.G. Narehood (2009) [30, 57, 83, 85]. Moreover, several simulation models to Pd-H systems were performed to investigate their H-absorption and desorption isotherms in order to estimate the phase transformations in different Pd-clusters sizes and shapes [88, 89].

2.2 Magnesium as Hydrogen Storage Material

Magnesium (Mg) is an alkaline earth metal with very low atomic weight $24.31\text{g}\cdot\text{mol}^{-1}$ compared to Pd-metal ($106.42\text{g}\cdot\text{mol}^{-1}$). Mg is considered one of the light metals for H-storage materials with large gravimetric and volumetric capacity ($\sim 7.6\text{ wt\%}$ and $\sim 109\text{ g}\cdot\text{L}^{-3}$, respectively), for its stoichiometric hydride with formula MgH_2 [66]. Unlikely, Mg-H systems suffer from numerous of drawbacks:

- (I) Mg forms a very stable hydride according to the bond nature between magnesium and hydrogen (strong ionic bonds), which resulting in a high enthalpy of Mg-hydride formation ($\Delta H_f \sim -75\text{ kJ}\cdot\text{mol}^{-1}$). This means high temperature (ca. 300°C) is required for hydrogen desorption [7, 97].
- (II) The oxide layer on Mg-surface, due to the high affinity of magnesium to oxygen that acts as a diffusion barrier. This leads to lowering of hydrogen absorption, not fully Mg-hydrogenation as well as lowering in the H-absorption/desorption rate [97, 108].

(III) Magnesium surface has a poor ability to dissociate H-molecules and a shell of hydride phase leads to prevent the hydrogen diffusion into magnesium lattice [7, 97, 108].

The ball-milling or spark discharged generation methods of Mg to its nano-sized particles is one of the resolved manners for Mg drawbacks by lowering the grain size and thus the diffusion path, which leads to improve the hydrogenation kinetic that was performed by Zaluski et al and V.A. Vons et al, respectively [97, 109], or by changing their structure, as forming Mg-powders, thin films ... etc.

The other available manner to resolve the poor diffusion and low rate hydrogen absorption/desorption processes is by catalyzing the hydrogenation of Mg through alloying, or by formation a shell surrounding Mg-metal by other chemical compound particularly, transition metals, e.g. Ni, Sc, Pd, Nb... etc. [110-114]. Where, the alloying of Mg may change the lattice structure of magnesium, hence increasing the H-diffusion and/or by improving the hydrogen dissociation on Mg-surface. Alloying also may be affected on the H-desorption process by lowering the stability of Mg-H system through lowering the bond strength between Mg and H [111].

The remains problem in this case is the significant lowering of hydrogen density of metal hydrides, especially if heavy metals were used, but this field of science is inactive and still needs more extensive researches.

Several Mg alloys have been studied [112, 115-117], some of these were summarized in table 2.1 with their gravimetric and volumetric storage capacities.

Table 2.1: Volumetric and gravimetric hydrogen content of different materials. [97]

Material	H-atoms per cm ³ ($\times 10^{22}$)	Weight % hydrogen
H ₂ gas, 200 bar (2850 psi)	0.99	100
H ₂ liquid, 20 K (-253°C)	4.2	100
H ₂ solid, 4.2 K (-269°C)	5.3	100
MgH ₂	6.5	7.6
Mg ₂ NiH ₄	5.9	3.6
FeTiH _{1.95}	6.0	1.89
LaNi ₅ H _{6.7}	5.5	1.37
ZrMn ₂ H _{3.6}	6.0	1.75
VH ₂	11.4	2.10

2.3 Combined Palladium and Magnesium Solids as Hydrogen Storage Material

One of the most recent metal was intensively investigated to improve hydrogenation of Mg is Pd-metal.

Many variant morphological nano-structural material and shapes of Mg-Pd systems have been synthesized and their hydrogenation-dehydrogenation processes were investigated, i.e. Pd/Mg film, Pd/Mg/Pd three-layers nano-composites (Sandwich film), alloys and decorated nano-structural (Core-Shell morphology) [95, 118-123].

In 2002, K. Higuchi et al. investigated of the H-sorption (under 373 K and 0.1 MPa) and the effects of their structural properties for nano-composite three-layered Pd(50nm)/Mg(xnm)/Pd(50nm) films that were prepared by RF-associated magnetron sputtering method. They found that the Pd-layer Mg-film contain ~5.0 mass% of H and the dehydrogenation rate remarkably shifted to lower temperature value with thicker Mg-film (456K for x=25nm and 360K for x=800nm) that was explained as cooperative elastic interaction between nano-structured Mg and Pd layers [118].

In 2010, Same results for K. Higuchi were confirmed by S. Barcelo, et al. as well as the measurements for the formation energy of (50nm) Pd/Mg/Pd film, which was less than of bulk MgH₂ ($\Delta H_f = -68\text{kJ}\cdot\text{mol}^{-1}$) [72]. In 2005, contrast results were obtained by J. Paillier and L. Rone. Where, the maximum H/Pd for Pd-layer was lower than the usually observed in bulk Pd (0.67), which was explained as lattice anisotropic strain of the Pd-layer that induced the broadening in the interstitial site energy distribution as well as the restrict of lattice expansion by substrate. Moreover, they found that the Mg-layer has no impacts on hydrogenation or dehydrogenation processes, which was explained as an indication for oxide surface formation in Mg-layer or as the MgH₂ that located near to Mg/Pd interface and was acting as barrier for H-diffusion [119].

The core/shell nano-structural materials of magnesium and palladium have been investigated in few literature which showed promising hydrogen storage capacity enhancements.

One of these attempts was carried out by X. Xu et al. [95]. Where, micrometer-sized of Mg was catalyzed by doping with Pd. The H-absorption/desorption properties were investigated using Tapered Element Oscillation Microbalance (TEOM) and the H-storage capacity was compared with traditional volumetric method [95]. The H-kinetics were studied at (T=613K and ambient pressure) and was found that Pd-doping Mg has the faster kinetic and reversible process in comparing with pure-Mg, as well as with fully desorption process of all absorbed H in 40 min in comparing with only 50% of absorbed H in pure-Mg was released.

Each of E. Callini, et al. (2009) and L Pasquini, et al. (2013) [94, 123] prepared Mg with a coating of oxide layer and decorated by Pd using inert-gas condensation method. The formed particle sizes were around 50-1000 nm and their H-absorption and desorption kinetics were investigated under conditions of (T ~550-600 K and high pressure ~ 0.3-0.5 MPa). Fast and reliable reversibility of H-in prepared particles were observed with 0.5 wt. %, the lowering of gravimetric capacity from 7 wt. % of MgH-system were attributed to the formed alloying layer (2-3 nm in size) of Pd-Mg [94,123].

In-situ XRD for Mg/Pd core/shell cluster was obtained by M. Suleiman et al., which was showed higher lattice expansion in their crystallites during H-loading process in comparison with same sized Pd-clusters [124].

The literary result of H-kinetics and isotherms, for variant Mg-Pd systems Shows that, they are promising reliable hydrogenation-dehydrogenation processes with large enhancements of their gravimetric capacity. But this field of science still requires more and more attentions for more understanding of their H-behaviors on its microscopic perspective.

2.4 Objectives of This Work

- 1- Selective synthesis of CS bimetallic clusters from Mg and Pd metals by reliable, simple and cheap preparation technique using the electrolysis cell.
- 2- Investigating the size, structures, shapes and morphological structure of the as-prepared clusters.
- 3- Investigating the effect of imposed current density and the concentration of the core precursor salt on as-prepared cluster's size, structure and morphology.
- 4- Investigating the optical properties and band gap energies of the as-prepared clusters and the dependence on clusters size and morphology.
- 5- Investigating the hydrogen storage capacity and the hydride formation from both points of views; thermodynamic and kinetic by using volumetric and gravimetric techniques.

CHAPTER (3)

EXPERIMENTAL TECHNEQUES

In this work, the preparation of tetraoctylammonium bromide (TOAB) stabilized magnesium/palladium core/shell (MgPd CS) clusters were performed by combined salt-reduction electrochemical technique. Then, the measurements for hydrogen storage capacity on as-prepared clusters are obtained by gravimetric and volumetric techniques.

In this chapter, details about the experimental and characterization techniques that were used to prepare and investigate cluster samples, in order to estimate their sizes, size-distributions, shapes, structures, morphologies and elemental compositions will be presented. Thereafter, the gravimetric and volumetric experimental methods were used to investigate the hydrogen storage capacity from both points of view, thermodynamic and kinetic which will be presented herein.

3.1 Chemicals and Materials

All the chemicals are purchased in their pure and dry form. Anhydrous Magnesium Sulfate (MgSO_4) was purchased from Frutarom LTD Company. Palladium foil (0.05mm thickness) and the tetraoctylammonium bromide ($\text{C}_{32}\text{H}_{68}\text{BrN}$) were purchased from Aldrich Company. Acetonitrile (CH_3CN) solvent was purchased from C.S. Company.

3.2 Equipments and Apparatus

The preparation of MgPd CS clusters was achieved by using a constructing electrolysis setup as shown in the photographic image, figure 3.1. The setup made of 100 mL electrolysis cell. The cell is well-covered with four-slots Teflon lid: Two of them for carrying the electrodes (cathode and anode), one for the gas (nitrogen) inlet and the other for charging and discharging the cell with reaction mixtures and behaves as gas outlet.



Figure 3.1: Photographic image for the setup that was used in the preparation of samples. Composed of three main parts: (I) electrolysis cell (Pd-anode, counter cathode and nitrogen inlet/outlet system), (II) power supply for current generation and (III) ultrasonic shaking system.

The electrodes were connected with dual tracking (5 Volt fixed) Laboratory DC-Power Supply GW (Model, GPC-3030D) and compliance with Regulation (Model, EN61010-1).

The mixing of solution contents were carried out ultrasonically in a 120 W ultrasonic vibrator that vibrates at frequency (400 kHz), which was obtained by Sonicator MRC (Model, AC-120H).

The analysis of size, structure, morphology, and elemental composition of the as-prepared cluster samples were performed with Fourier-Transform Infrared Spectroscopy (FT-IR), Scanning Electron Microscope (SEM), X-ray Diffraction spectroscopy (XRD), Transition Electron Microscope (TEM), Energy Dispersive X-Ray (EDX), atomic absorption spectroscopy (AAS) and UV-VIS Spectrophotometer.

3.2.1 Fourier-Transform-Infrared Spectrophotometers (FT-IR)

The FT-IR that was used in studying the surface of as-prepared clusters and the effect of stabilizing agent on the clusters surface were performed by using Nicolet iS5 FT-IR spectrophotometry, which is a Thermo-Scientific Corporation product attached to iD3-ATR sampling accessory.

3.2.2 Scanning Electron Microscope (SEM)

The highlight microscopic image for co-agglomerate and solid dispersion of as-prepared clusters was performed with SEM type Jeol (Model, JMS-840), with acceleration voltage equivalent to 20 KV, probe current 45 nA and counting time 60 sec.

The specimen were prepared by coating the film "substrate" with carbon before the solids were dispersed over the film in order to prevent electron beam accumulation.

3.2.3 Powder X-Ray Diffraction (XRD)

The studying of crystallite and the size of as-prepared clusters were performed by using solid-dispersion powder XRD type Philips (Model, PW1710). Diffractometer attached to Bragg-Brentano Geometry (0.2) and Ni-filtered Cu-K α 1 radiation ($\lambda=1.54051 \text{ \AA}$), with steps of 0.05° and counting time of 5 sec.

3.2.4 Transmission Electron Microscope (TEM)

The studying of morphology, size, and size-distribution of as-prepared clusters were performed by using TEM, type Philips EM 420-ST Microscope, with resolution limit 0.3nm, information limit 0.2 nm and acceleration voltage 120 kV.

The spacemen were prepared by using sol-gel deep coating technique, where scooping of cluster from its solution on a carbon-coated copper grid ($\Phi=3 \text{ mm}$ and 400 mesh), and left to dry at room temperature for 7 h's.

3.2.5 Energy Dispersive X-Ray Spectroscopy (EDX)

The elemental compositions of as-prepared clusters were performed by using EDX attachment on SEM (EDX-SEM) and TEM (EDX-TEM).

3.2.6 Atomic Absorption Spectroscopy (AAS)

The analysis of the metallic composition of cluster samples by measuring the exact amount of (Mg and Pd) in the cluster sample were performed by using AAS Flam, type of ICE 3000 AA spectrometer a product of Thermo Scientific Co.

For this purpose, four stock solutions of the four cluster samples were prepared by weighing (ca. 0.01 g) and dissolving them in 4 mL of aqua-regia acid under ultrasonic shaking for 15 min, before the solution was transferred in 10 mL volumetric flask (VF) and filled to the mark with Deionized Water (DW), except sample No.1, which required 8.0 mL of aqua-regia acid to dissolve all amounts of sample, under ultrasonic shaking to 20 min, then diluted with DW in 50 mL VF. These diluted solutions directly were measured by AAS with using Pd and Mg hollow-cathode lamps, wavelengths 247.6 and 285.2 nm, respectively.

3.2.7 UV-VIS Spectroscopy

The studying of the optical properties and Surface Plasmon Resonance (SPR) of as-prepared clusters were performed by using UV-VIS-NIR

scanning spectrophotometer type TCC-260 (220 V and ~50/60 Hz) a product of Shimadzu Corporation.

The solutions were prepared by dissolving of 0.05 g of as-prepared clusters in 10 mL of acetone, and then the solution was transferred into 1 cm of Quartz cell before analysis.

3.2.8 Volumetric and Gravimetric Hydrogen Storage Measurements

The volumetric analysis of H-storage capacity was performed by Sieverts' apparatus that was designed and furnished for this MSc. work in An-Najah Laboratories.

The gravimetric analysis for H-storage capacity was performed by high-vacuum electronic microbalance (M-25-DV) a product of the Sartorius company-Goettingen, with highly pure hydrogen gas (99.9999%).

All the H-storage experiments were performed at ambient temperature (25°C) and under loading-pressure up to 1 bar.

3.3 Preparation of Cluster Samples

The clusters were prepared by electrochemical technique under purging of inert gas (nitrogen). The magnesium salt (MgSO_4) was dissolved in acetonitrile (CH_3CN), and then the solution was charged to the electrolysis cell in the presence of TOAB as stabilizing agent.

Two identical Pd-plates were used as electrodes. Then the produced precipitates were collected after supernatant have been siphoned off by vacuum setup.

3.3.1 General Procedure for the Preparation of Magnesium-Palladium Clusters

3.3.1.1 Electrochemical Preparation of Cluster Samples

In the typical procedure for the preparation of TOAB stabilized CS-MgPd clusters was carried out by preparing 75 mL solution of 0.1 M of surfactant (TOAB) in acetonitrile solvent (CH_3CN) and charging the electrolysis cell. Then, a specific weight of MgSO_4 salt is added to the solution.

Two pure sheets of palladium were used as electrodes for the cell, with geometric surface area equal to ($5.1 \times 1.2 \text{ cm}^2$) and 0.05 mm in thickness, and distance between both Pd-electrodes equal to 15 mm.

After purging the solution about 15 min with nitrogen, and thermally set at 25°C , a constant current density was then allowed to pass through the cell. After about 60 min the electrolysis was stopped and the electrolyte was transferred to 250 mL Erlenmeyer flask, and then the product was left to set for 24 hours before the supernatant siphoned off.

3.3.1.2 Vacuum Drying for Prepared Solids

In order to siphoning off the supernatant and drying the precipitating solids, after the electrolysis reaction was stopped, a vacuum setup was used for

this purpose as shown in the scheme in figure 3.2. The cluster's solids were rested at the bottom of the flask. The connected rotational pump at the end side of the setup was used for drawing the supernatant out. The trapping flask with ice cooling jacket was used to enhance the vacuum process, as well as a capture trap for extracted vapor. After the whole solvent was removed, the rested solids were dried in oven for 1h at 35°C.

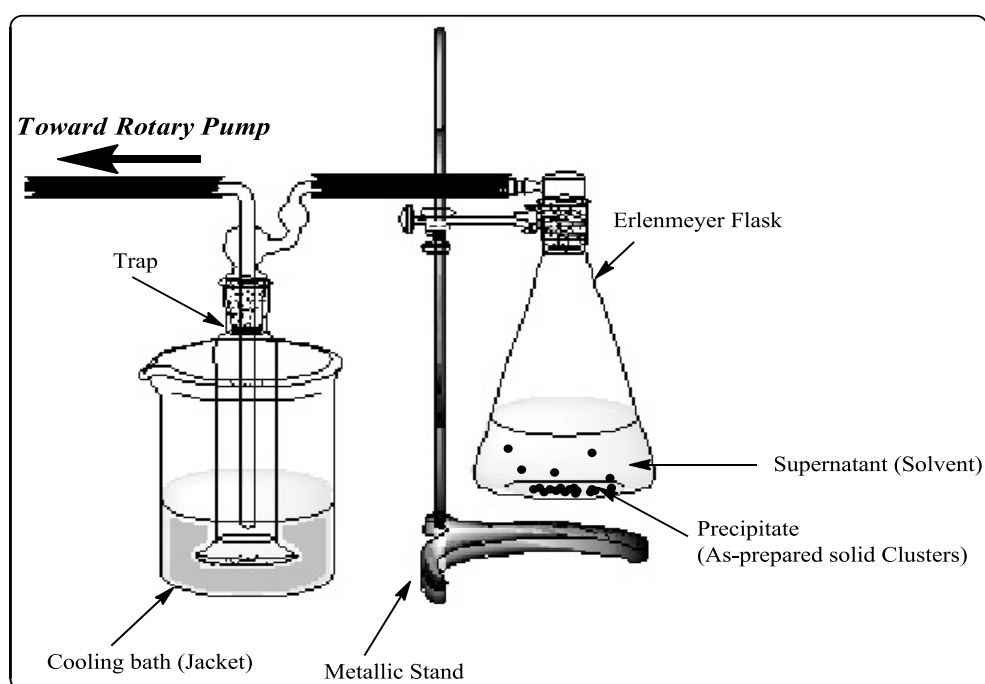


Figure 3.2: Schematic image for the drying vacuum setup of as-prepared clusters through extracting the clusters from the reaction solution by siphoned off the supernatant.

3.4 Hydrogen Storage Capacity Measurements

3.4.1 Gravimetric Measurements

Hydrogen storage measurements from kinetic and thermodynamic points of view were performed with a high-vacuum electronic microbalance

apparatus. The schematic image for its compartments is displayed in figure 3.3.

Typically the electronic microbalance consists of two main systems: (i) Gas-handling system. Where, the handling with entered H-pressure will be loaded toward the sample can be accomplished. (ii) Microbalance system. It is the part, which is responsible for measuring the amount of hydrogen that absorbed (or desorbed) by the sample. Based on, monitoring the changes in the sample's weight.

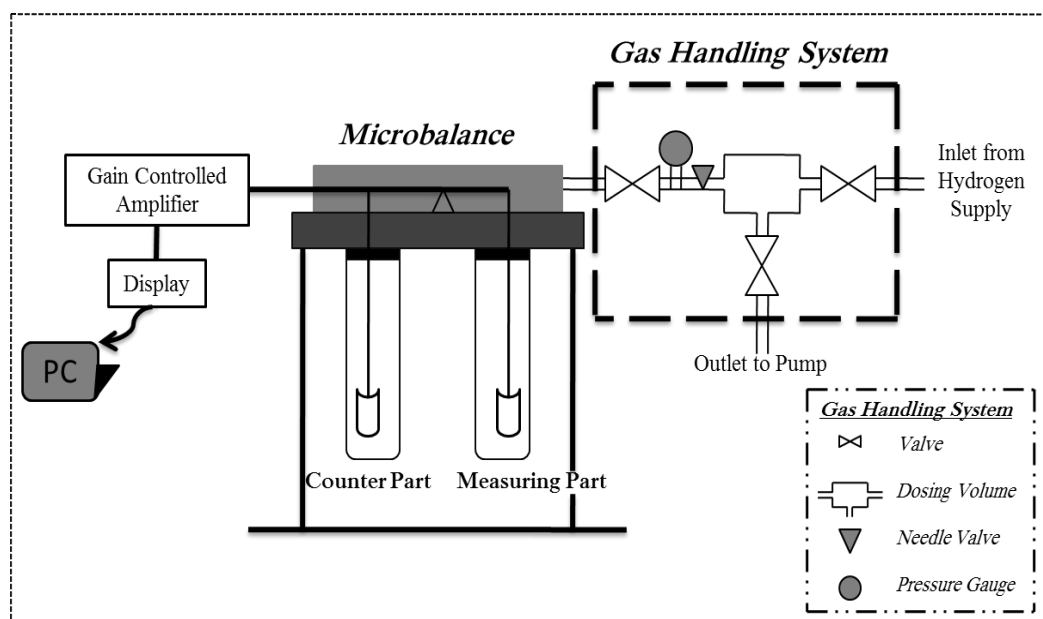


Figure 3.3: Schematic image of High-Vacuum Electronic-Microbalance was used in Hydrogen gravimetric measurements. [43]

3.4.1.1 General Procedure for the Hydrogen Measurements

3.4.1.1.1 Sample Pre-Treatment

In the typical procedure, the measuring part of the microbalance was charged with 0.1g of the cluster sample through stacking them into

tesa-film ($2.5 \times 15 \text{ cm}^2$), while the counterpart was charged with an equal weight of hydrogen non-adsorbing material, which composed of non-magnetic steel. Both of tesa-film and non-magnetic steel are not adsorbing any amount of hydrogen. Therefore, they will never effect on the H-gravimetric measurements.

The pre-treatment of the cluster sample is an important step before H-measurements, the cluster surfaces usually have a thin oxide layer and in order to remove or reduce, it requires evacuating then loading with hydrogen pressure (10^5 Pa) for 24 hours and subsequent evacuation again for about 36 hours twice times at least.

3.4.1.1.2 H- Absorption/Desorption Thermodynamic Measurements

H-absorption (or desorption) pressure-concentration isotherm of cluster sample is obtained by variant H-loading (or unloading) steps into sample. As represented in the schematic draw in figure 3.4.

Each loading (or unloading) step with known value of pressure was corresponding to the amount of hydrogen adsorbed (or desorbed) from the sample at that pressure value. Therefore the increasing or decreasing in the weight and pressure will be monitored during the time for each step with the aid of computer program.

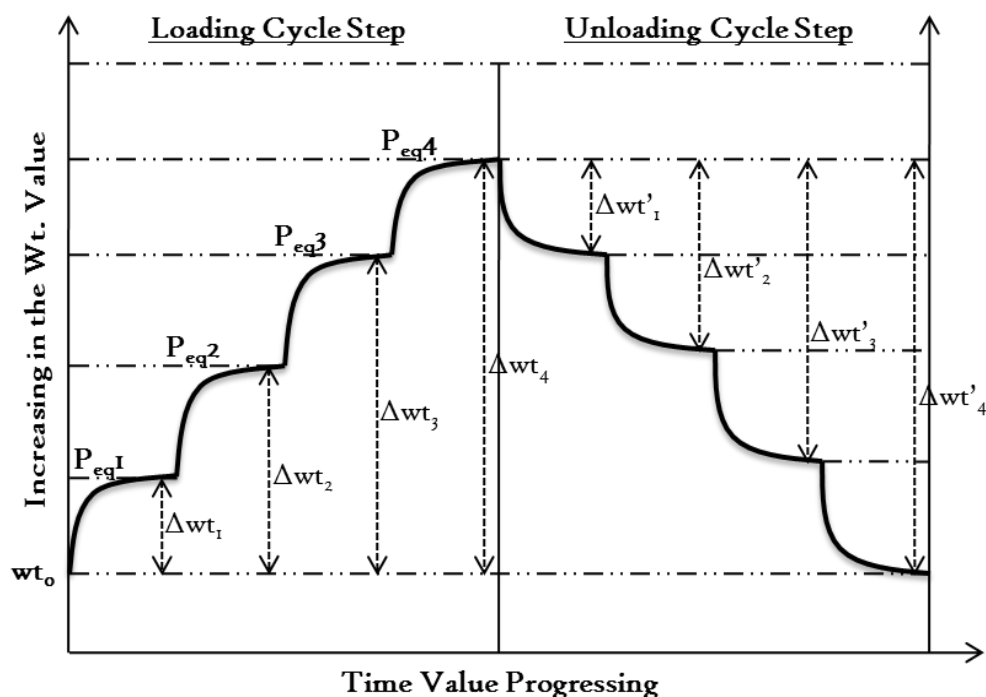


Figure 3.4: Schematic draw image of hydrogen gravimetric loading-unloading steps which was going to use for constructing the pressure-composition isotherm. [43]

3.4.1.1.3 Hydrogen Absorption/Desorption Kinetics

H-isothermal kinetics for absorption (or desorption) process is obtained by loading (or unloading) of 90 mbar (or 180 mbar) of H-pressure per min on the measuring chamber.

The hydrogen absorption (or desorption) kinetic was measured by monitoring the increasing (or decreasing) in the sample's weight during the time. The increase (or decrease) of sample's weight corresponds to the weight of H-absorbed (or desorbed) by the sample during that time.

3.4.2. Volumetric Measurements

The volumetric hydrogen apparatus (also known as a Sieverts' apparatus) is a gas manifold with a series of tubes and valves connecting the sample chamber to one or more pressure reservoirs of known volume, and pressure transducers for measuring reservoir pressure, see figure 3.5.

The apparatus described here is designed and furnished volumetric apparatus for this work, that includes a 316-stainless steel tubes and reservoirs (pre-loading reservoir and measuring reservoir (sample chamber) with approximate volumes 1L and 0.144L, respectively, gland-gasket fittings, manual valves, two capacitance pressure transducers and the electronic parts (i.e. PLC, data-recorder, .. etc.).

A typical measurement of H-volumetric consists of a series of steps: (i) the sample was pre-treating with hydrogen loading and evacuating for few hours. (ii) the valve between the sample and reservoir was closed in order to introducing gas into the reservoir to bring it to the pressure of interest. (iii) The valve between the sample and reservoir was opened and monitoring the reservoir (sample's chamber) pressure changes. The amount of gas uptake (or release) by the sample is deduced from the resulting reservoir pressure drop (or rise).

The kinetics of hydrogen absorption (or desorption) by a pre-weighting sample can be measured by loading (unloading) a specific pressure in measuring chamber and monitoring the drop (rise) in pressure during the time. Based on ideal gas formula and the pressure difference the weight of hydrogen absorption (desorption) during that time can be calculated.

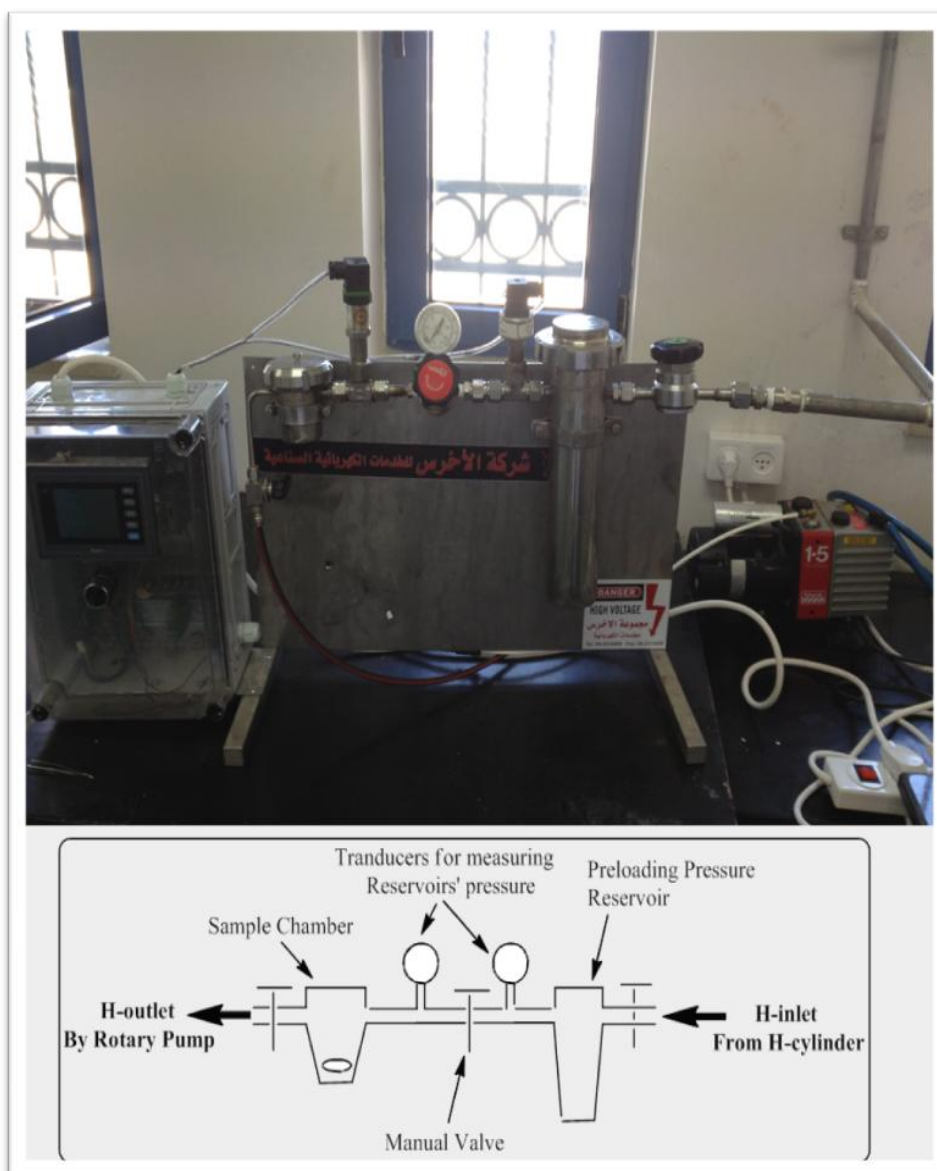


Figure 3.5: Photographic image (upward) and schematic image (downward) for the designed volumetric apparatus and its main compartments.

CHAPTER (4)

Results and Discussion

The characterization of the as-prepared cluster samples was performed by using different characterization techniques: FT-IR, UV-Vis, SEM, XRD, TEM, EDS and AAS. Thereafter, their hydrogen absorption and desorption behaviors from both points of view "kinetic and thermodynamic" were investigated.

4.1 Samples Preparation and Characterization

In this section, all the results that are obtained by using the characterization techniques: IR, SEM, TEM, XRD, UV-Vis, EDS and AAS to estimate the size, size distribution, shape, optical properties, morphology and structural composition of the as-prepared cluster samples will be presented and discussed.

Four cluster samples have been prepared by combined salt reduction-electrochemical technique as maintained in section (3.3). The four samples were prepared under different preparation conditions, which are summarized in table 4.1. The four samples were prepared at constant temperature of 25°C by using two geometrically equivalent Pd-electrodes with surface area equivalent to (5.1x1.2) cm² and thickness equal to 0.05 mm. The both electrodes (anode and cathode) were separated by a distance equal to 15 mm. The reaction was run for 1h before the solution was rest and the precipitate was collected and dried.

Table 4.1 summarizes the imposed current density (J) values "in mA.cm⁻²", the weight (wt.) "in grams" and molar concentration of stabilizer, the TOAB (C_{TOAB}) and magnesium metal (C_{Mg}) that has been used in the preparation of each cluster sample.

The theoretical amount of the palladium in the reaction was measured from the anodic weight difference before and after the reaction. These values are also found in table 4.1.

Table 4.1: The preparation conditions of the four as-prepared cluster samples (1-4) and their metallic composition wt. %.

Sample No.	No.1	No.2	No.3	No.4
J [mA.cm ⁻²]	5.2	3.0	3.0	1.5
Wt. TOAB [g]	3.00	3.00	3.00	3.00
C _{TOAB} [M]	0.124	0.124	0.124	0.124
Wt. Mg [g]	0.04	0.04	0.09	0.04
C _{Mg} [M]	0.022	0.022	0.049	0.022
Wt. Pd [g] [*]	0.5027	0.1259	0.1133	0.1052
% Pd in sample [wt%] ^{**}	12.879	3.497	2.873	3.363
% Mg in sample [wt%] ^{***}	0.974	1.111	2.384	1.311
% M in sample [wt%] ^{****}	13.853	4.608	5.257	4.674
Wt. of Precipitate [g] [‡]	3.903	3.600	3.943	3.128

* The theoretical yield of Pd metal in the samples, which was obtained by calculating the weight difference of the anode before and after the reaction.

** (***) The weight percent (wt%) of palladium (or magnesium) in the collected precipitate, which was measured by dividing Pd (or Mg) weight (wt.) by the weight of precipitate.

**** The weight percent of total metal-contents (Mg and Pd) in the collected precipitate.

‡ The weight of product (precipitate) that was collected after the reaction was finished.

Wt. (weight) – Wt. % (weight percent) – C (Molar concentration) -M (Total metal content)

Based on the summarized data in table 1.1, it is noted that the amount of dissolved Pd-atoms increases (0.11, 0.13 and 0.50) with increasing of imposed current density (1.5, 3.0 and 5.2), respectively. The amount of collected product "precipitate" from each sample after the end of the reaction was found to be about (3.1-3.9 g), review table 4.1.

The wt. % of metallic component(s) of (Pd, Mg and PdMg) in each cluster sample is also observed in table 4.1, and was measured by dividing the weight of metallic component(s) over the weight of collected precipitate.

Samples "1, 2 and 4" were prepared at different current density as estimating to the current density effect on the size and morphological structure of the formed clusters. Samples "2 and 3" were prepared at different concentrations for Mg-content to estimate their effects on the formed clusters.

4.1.1 Fourier Transform–Infrared Spectroscopy of as-Prepared Cluster Samples

The Fourier Transforms - Infrared (FT-IR) Spectroscopy was used to probe the surface of the as-prepared clusters and the organic portion "stabilizer" on their surfaces.

Figure 4.1 shows FT-IR spectrum for the TOAB "stabilizer" in its pure-solid form. While, figure 4.2 shows the FT-IR spectra for the four TOAB stabilized cluster samples "1, 2, 3 and 4", respectively.

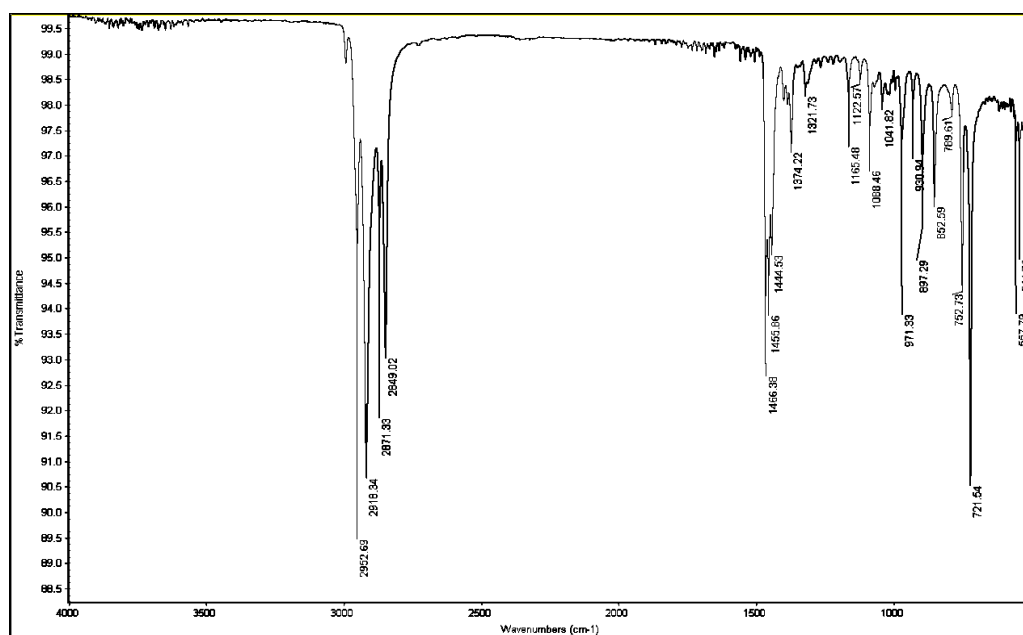


Figure 4.1: FT-IR spectrum for the TOAB in its pure solid form.

The FT-IR spectrum for TOAB in its solid form shows spectral regions at wavelengths that are summarized in table 4.2. The spectral regions around $2500\text{-}3000\text{ cm}^{-1}$ belongs to the vibrational modes of the asymmetrical-symmetrical C-H stretching, these regions are important as they indicate the orientation and integrity variances of the methylene chain before and after stabilization of the clusters' surface [125, 126].

Spectral regions at 1466 and 1374 cm^{-1} corresponds to the vibrational bending modes of scissoring deformation for methylene and methyl groups, respectively [126, 127].

The spectral region at 721 cm^{-1} almost attributes to the rocking mode of the methylene group [126, 128], which are related to the long chain hydrocarbon "octyl-group", these results are summarized in table 4.2.

Table 4.2: The spectral regions for TOAB in its pure-solid form.

Beak Wavelength (cm^{-1})	Assignment	Ref.
2952.69	C-H (Stretch) for methyl-group	125-127
2918.34	C-H (Stretch) for asym. methylen-group	125-128
2849.02	C-H (Stretch) for sym. methylen-group	125-128
1466.38	H-C-H (Scissoring deformation) for methylene-group	126,127
1374.22	H-C-H (Scissoring deformation) for methyl-group	126
Bunch of (1000-1300)	C-C (Wagging mode) for methylene-group	126,129
721.54	H-C-H (Rocking mode) for methylene-group	126,128

The FT-IR spectra for the TOAB stabilized clusters show similar spectral regions for TOAB, but some broadening and higher intensity bands with $\sim 1\text{cm}^{-1}$ shifting to the higher wavenumber are observed. These observations on the TOAB spectral regions in the stabilized clusters' IR-spectra can be attributed to physical adsorption of TOAB on the clusters' surface with no remarkable defects in the chains of the stabilizer during the stabilization process of the formed clusters [126].

There are another new observed spectral regions in the FT-IR for TOAB stabilized clusters compared with FT-IR spectral for TOAB in its pure and solid form, which are:

- (i) Two broad bands near the region of 3325 and 3199 cm^{-1} , which corresponds to the O-H stretching for chemical and physical adsorption of water on the clusters' surface.
- (ii) Spectral regions at 2359 and 2171 cm^{-1} , which corresponds to carbon dioxide and cyano group stretching modes, respectively [130,131].

The cyano vibrational spectral can be attributed to acetonitrile used as solvent in the reaction, which is expected to be adsorped on the clusters' surface.

- (iii) Spectral regions at 1667 and 1568 cm^{-1} , which belongs to the C=O stretching for carbonyl group, which is attributed to the carbonate mono-dentate and bi-dentate on the clusters' surface, respectively [130,132]. It is believed that the carbonate was formed by a reaction between the adsorbed CO_2 and H_2O (humidity) with a catalyzing from the clusters surface. This is due manly to reactive Pd-surface [132].

All of these new observed specral regions in TOAB stabilized clusetrs are demonstrating to the clusters' surface reactivity and catalytic activity by Pd-surface metal with their surrounding.

The metal-oxide by FT-IR uaually observed as a band around 650 cm^{-1} . In this work no band near 650 cm^{-1} was obsarved. This is an indication for merly metal atoms at the clusters surface with no metal-oxide formation.

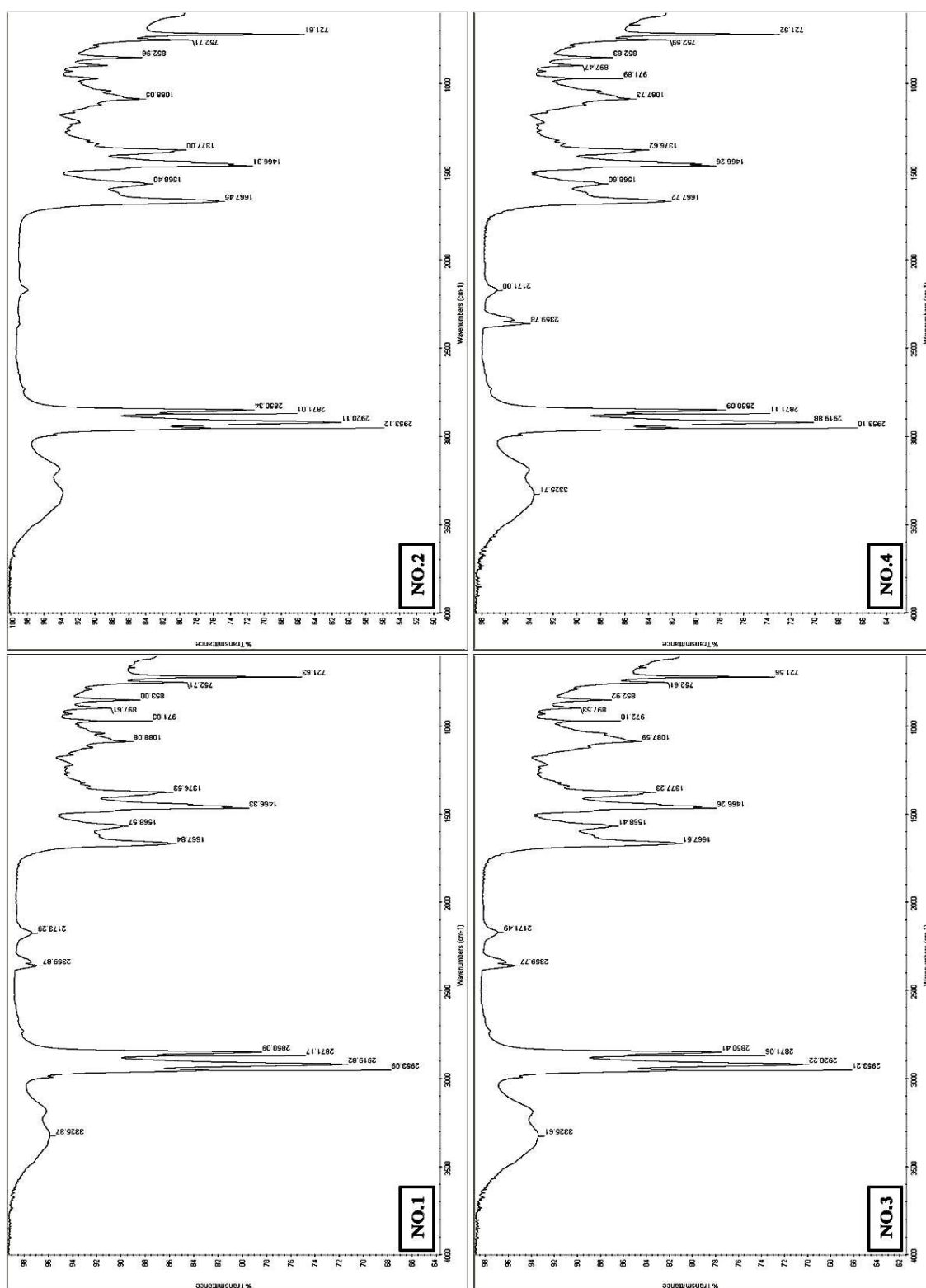


Figure 4.2: FT-IR spectrum of the as-prepared cluster samples (No. 1-4) for TOAB-stabilized MgPd CS Clusters.

4.1.2 Scanning Electron Microscopy of as-Prepared Cluster Samples

Figure 4.3 shows the scanning electron microscopy (SEM) images of the four as-prepared cluster samples.

The four cluster samples seemed like clouds under microscope (SEM), without a clear observation to the shapes of co-agglomerate particles. It is believed because of the small massive sized clusters, as will be confirmed by TEM in section (4.1.3). In addition to their highly attractive surface with the surrounding molecules, i.e. water molecules from environmental humidity, carbon dioxide gas and preparation solvent (acetonitrile), which are in agreement with obtained FT-IR, in section (4.1.1). These adsorbate molecules by clusters lead to the amorphous appearance by SEM.

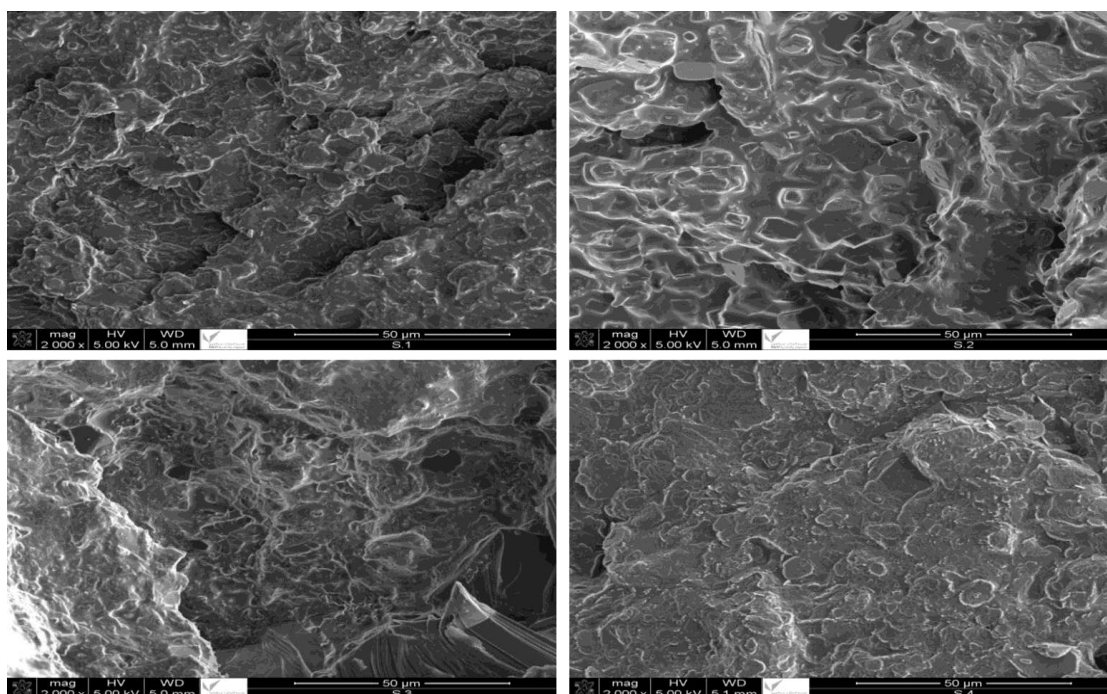


Figure 4.3: SEM images of the as-prepared cluster samples (No. 1-4) for TOAB-stabilized MgPd CS Clusters.

4.1.3 Transmission Electron Microscopy of as-Prepared Cluster Samples

The four cluster samples were analyzed by transmission electron microscopy (TEM) for estimating their sizes, shapes, and size-distributions. Figures 4.4-4.7 shows the TEM images of the as-prepared cluster samples, their specimen were prepared as mentioned in section (3.2.3).

The TEM images for as-prepared clusters shows co-agglomerate clusters with non-uniform distribution that may refers to nonhomogeneous-evaporation of the solvent, which was used to disperse the clusters over Cu-grid [133]. On the other hand, the specimen for sample No.2, the solvent was allowed to evaporate for 7 hours. This leads to more organized clusters distribution.

TEM images for the cluster samples shows a quasi-spherical clusters, with size lower than 5 nm and near to mono-sized distribution.

The core-shell morphology is hard to be observed by TEM. Because as-prepared clusters composed from couple of metals (Pd and Mg), with contrast penetration efficiency for the electron beams, and is expected that Pd-metal (the denser metal) is on the shell of the formed clusters with darker color appearance than Mg atoms. This prevents the characterization of the core Mg-metal [134, 135].

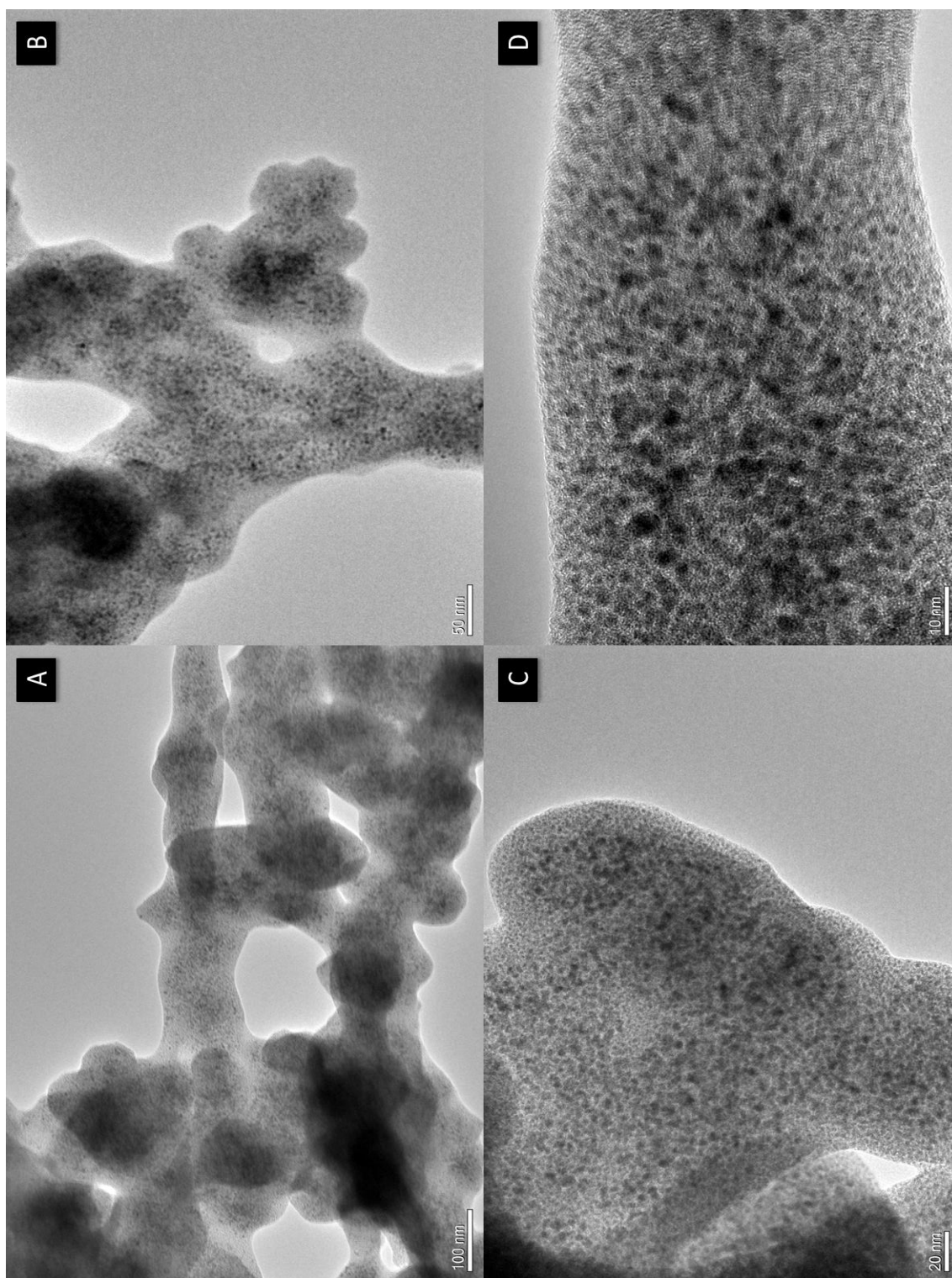


Figure 4.4: TEM images of the as-prepared cluster sample (No. 1), which was prepared at $J = 5.2 \text{ mA.cm}^{-2}$ and $C_{\text{Mg}} = 0.022 \text{ M}$. The scale bar is: (a) 100 nm, (b) 50 nm, (c) 20 nm and (d) 10 nm.

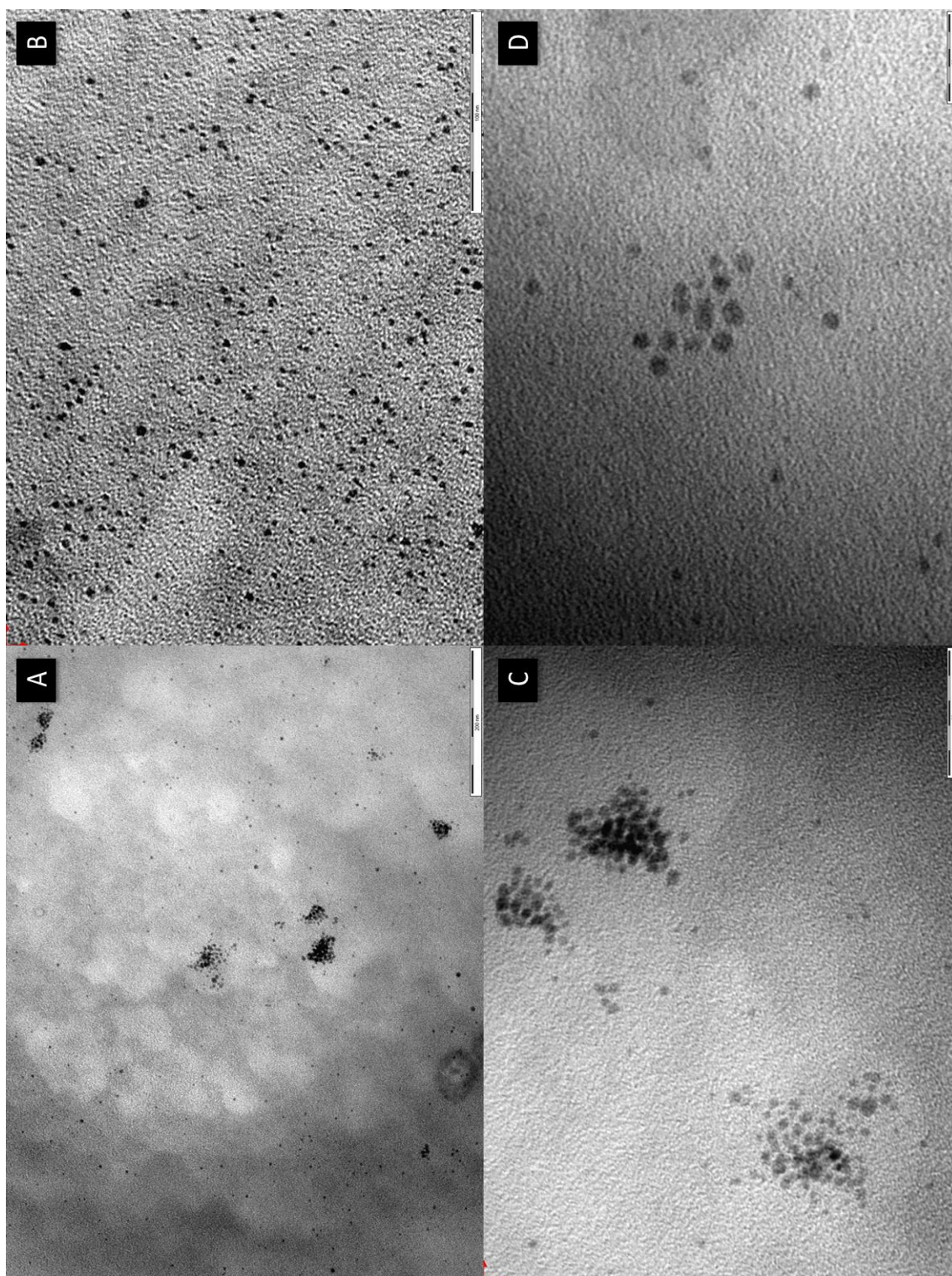


Figure 4.5: TEM images of the as-prepared cluster sample (No. 2), which was prepared at $J = 3.0 \text{ mA}\cdot\text{cm}^{-2}$ and $C_{\text{Mg}} = 0.022 \text{ M}$. The scale bar is: (a) 200 nm, (b) 100 nm, (c) 50 nm and (d) 20 nm.

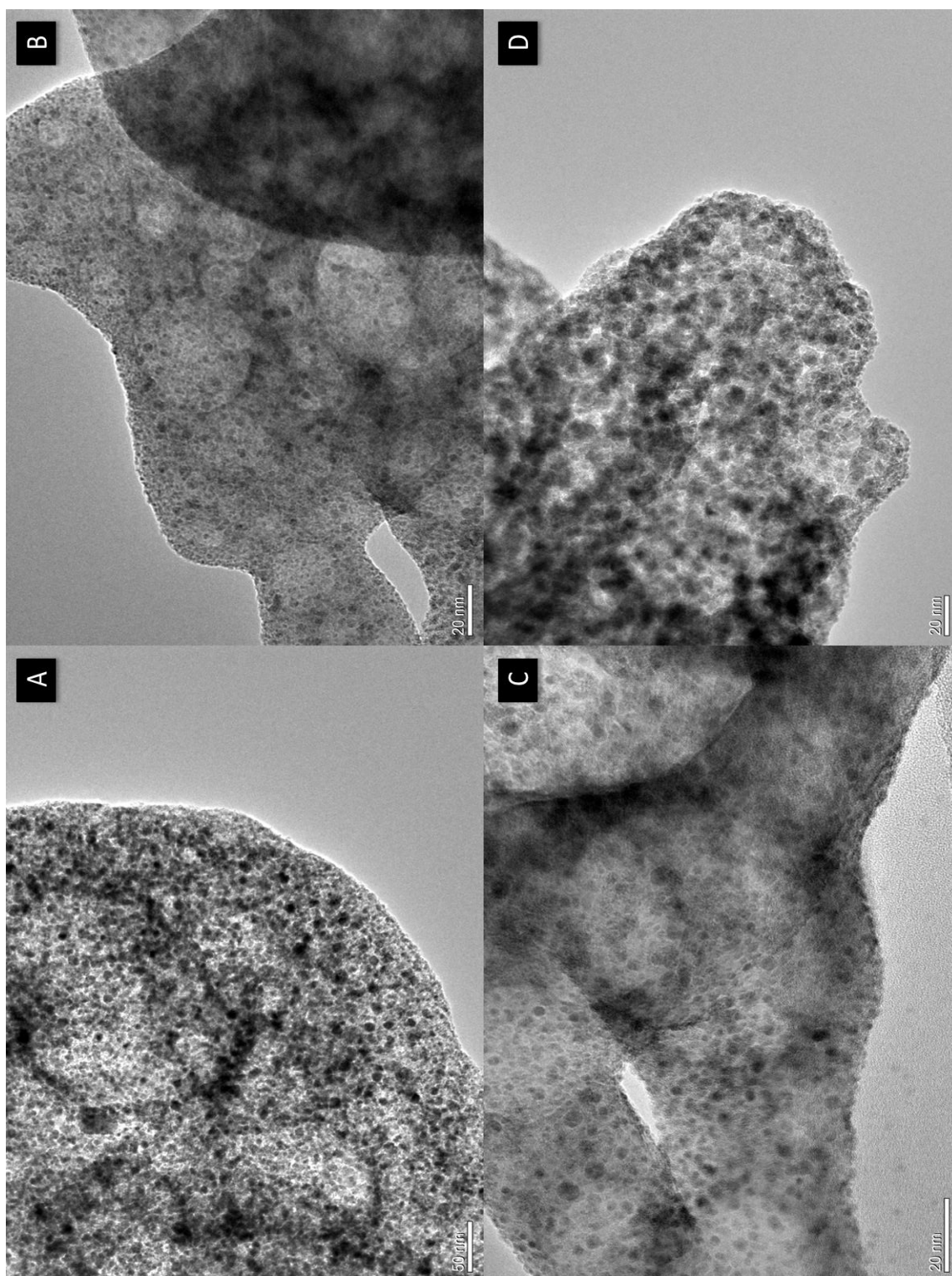


Figure 4.6: TEM images of the as-prepared cluster sample (No. 3), which was prepared at ($J = 3.0 \text{ mA}\cdot\text{cm}^{-2}$ and $C_{\text{Mg}} = 0.049 \text{ M}$). The scale bar is: (a) 50 nm, (b), (c) and (d) 20 nm.

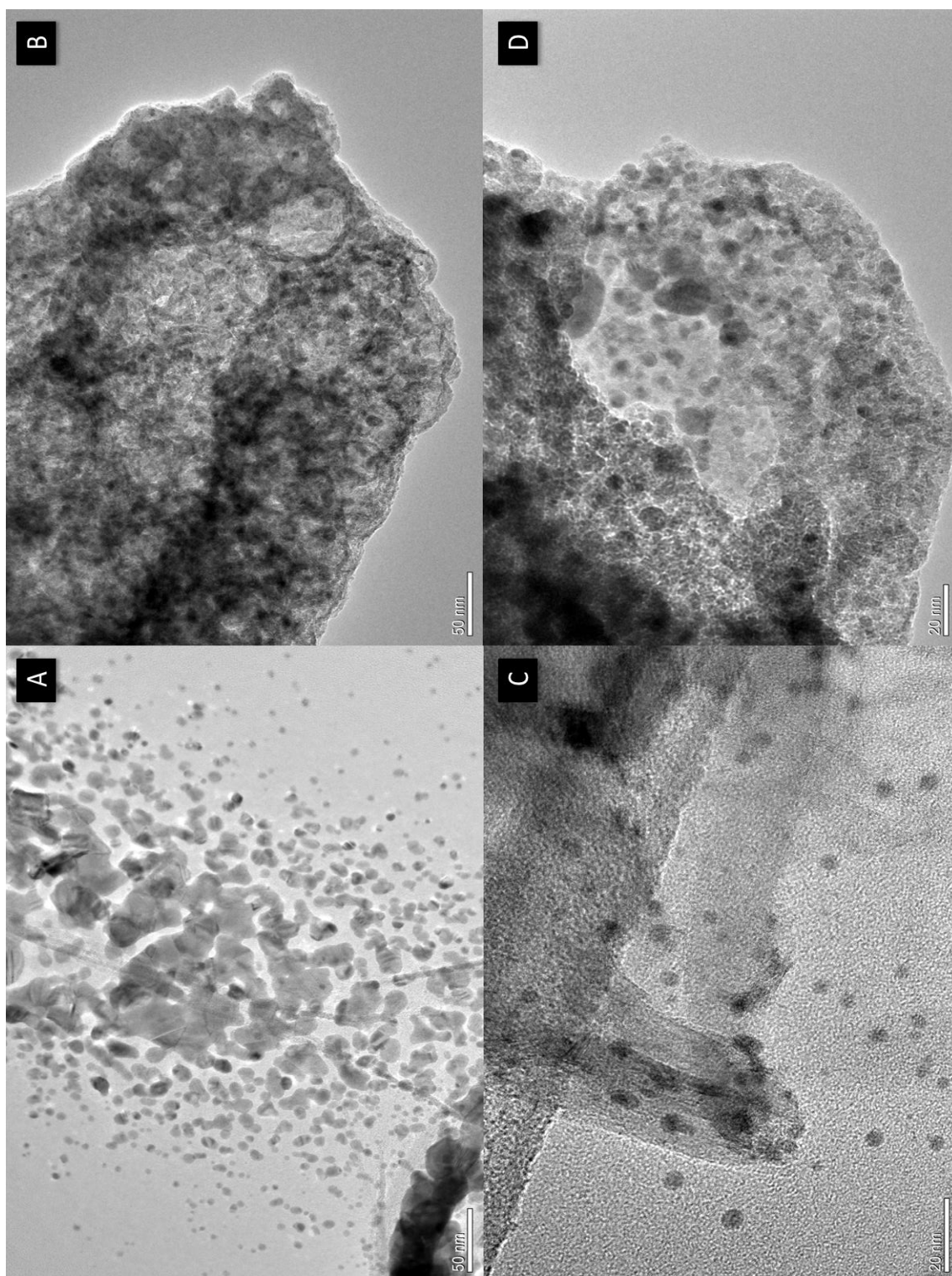


Figure 4.7: TEM images of the as-prepared cluster sample (No. 4), which was prepared at $J = 1.5 \text{ mA.cm}^{-2}$ and $C_{\text{Mg}} = 0.022 \text{ M}$. The scale bar is: (a) and (b) 50 nm, (c) and (d) 20 nm.

TEM images show a small sized particles "Clusters" (size < 5 nm) and very narrow size-distribution. The size and size-distribution of the as-prepared clusters were obtained by counting the most clarified particles with different sizes. Thereafter, a histogram would be constructed by estimating the number of clusters is in the same size range, as shown for sample No.2, in figure 4.8.

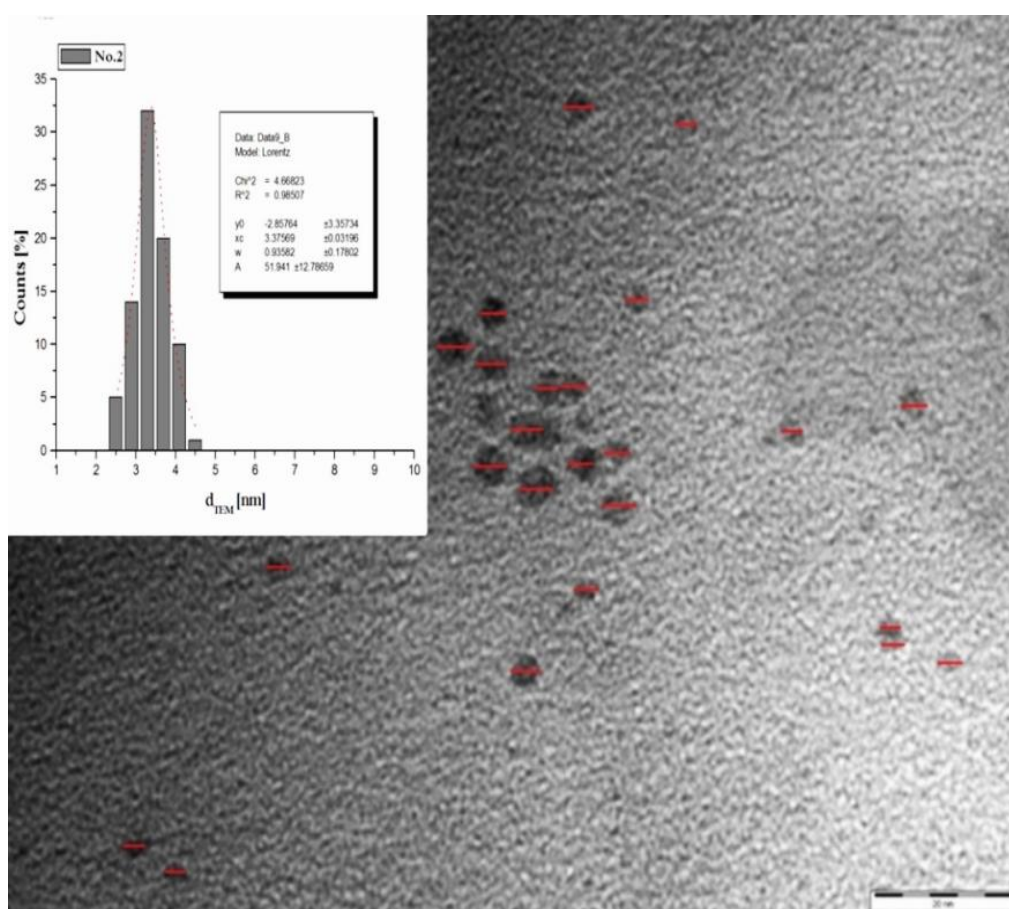


Figure 4.8: Size and size-distribution of as-prepared cluster sample (No. 2).

The peak and FWHM of the fitted histogram for each cluster sample, which was fitted by using a Lorentzian function, are attributed to the clusters' size and size-distribution, respectively.

In figure 4.9, the size and size-distribution of the as-prepared cluster samples "1, 2, 3 and 4" are shown. Dependence on Lorentzian-fitted histograms, the prepared clusters on cluster samples have very massive size (ca. 1.65, 3.48, 3.60 and 4.56 nm, respectively) and their size-distribution are near to mono-sized distribution (approximately to 1 nm), as shown in table 4.3.

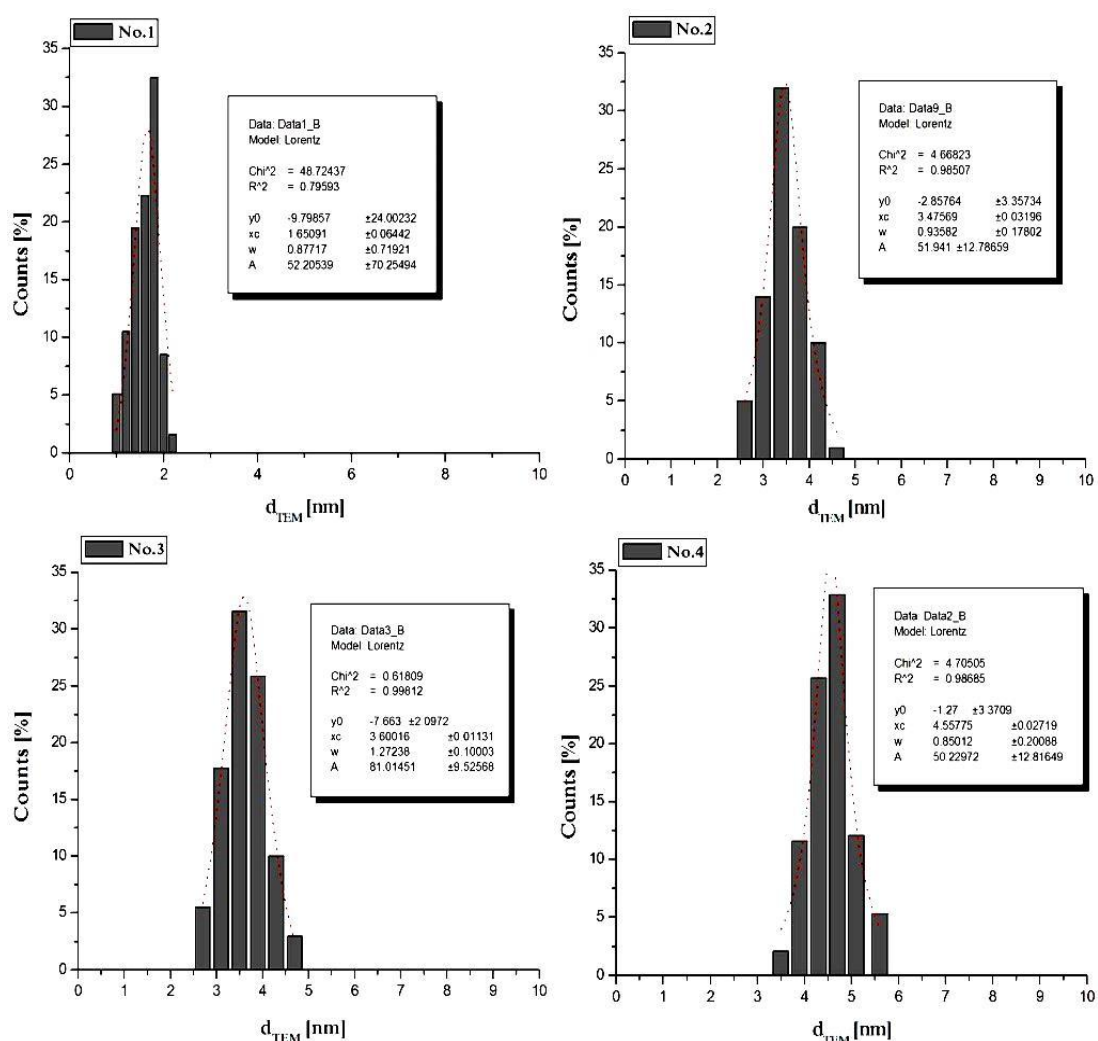


Figure 4.9: Constructed size-histograms for the size and size-distribution of as-prepared clusters (No.1-4) that obtained by the TEM.

Table 4.3: The size and size-distribution of as-prepared clusters that was obtained by the analysis of TEM.

Sample No.	D_{TEM} [nm]	Size-Distribution [nm]
		(FWHM)
No.1	1.651 (± 0.064)	0.878 (± 0.719)
No.2	3.476 (± 0.032)	0.936 (± 0.178)
No.3	3.600 (± 0.011)	1.272 (± 0.100)
No.4	4.558 (± 0.027)	0.850 (± 0.201)

4.1.4 X-Ray Diffraction of as-Prepared Cluster Samples

The X-ray diffraction (XRD) patterns of the as-prepared clusters are shown in the figure 4.10. XRD patterns were treated by Origin-Lab Program. The (111) diffraction peak, the most intense (main) peak was fitted by using Lorentzian function to estimate the FWHM, as shown in, figure 4.11.

XRD patterns of the as-prepared clusters show inordinate broadening in their diffraction patterns, which almost argued to the small sized clusters that are composed from multi-metallic constituents [117, 136-138]. Where, bimetallic clusters usually shows more broadening in their diffraction patterns in comparison with the patterns for monometallic clusters [139]. Therefore, the broadening in the XRD patterns strongly estimates the bimetallic constituents (of Mg and Pd metals) in the as-prepared clusters that can't be defined by TEM, in section (4.1.3).

The conventional XRD technique "X-ray from metal source, i.e. Cu- $K_{\alpha 1}$ " has low intensity beam and low resolution. On the other hand, nanosized particles have a large fraction of atoms located at or near to the surface and have large fluctuations in their crystalline structures [110, 135, 140, 141]. Therefore, these reasons can clearly explain the defacements into diffraction patterns of as-prepared clusters.

Two diffraction peaks can be observed clearly by XRD patterns of as-prepared clusters. These peaks are located at (2θ -values) near to 40° and 45° that are well-attributed to the Pd-(111) and Pd-(200) plane orientations (Miller-planes), respectively. These are near to the cubic (fcc-type) crystalline structure of Pd-bulk.

The fact, that the diffraction pattern of Mg is not observed has evidence about Mg-core and Pd-shell morphological structure, in term of heavy metal effect. Where, the heavier metallic atoms "i.e. Pd-atoms" shield the crystallography of the lighter metals (i.e. Mg-atoms) [135, 141, 143].

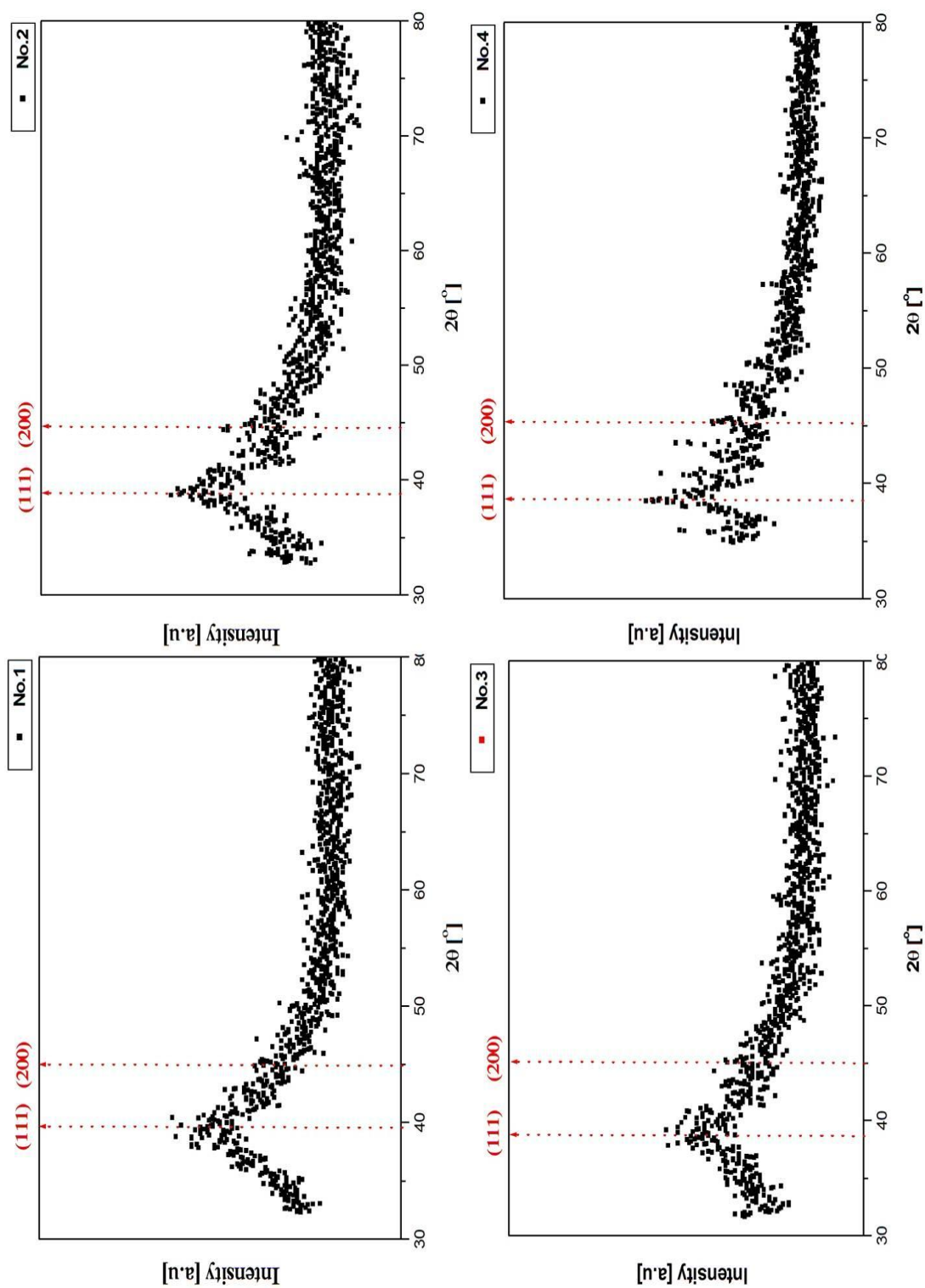


Figure 4.10: The XRD-patterns of the as-prepared cluster samples (No.1-4).

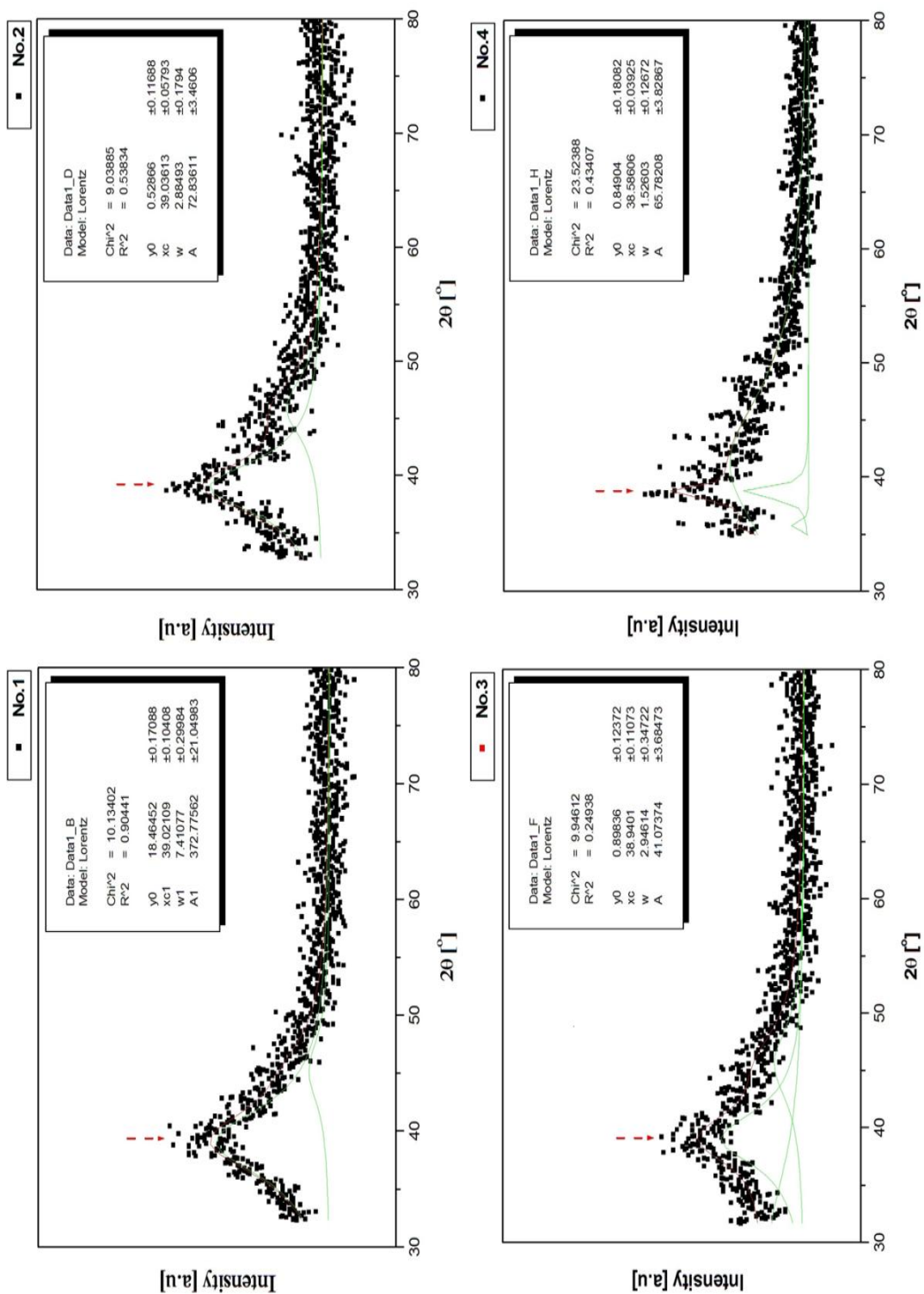


Figure 4.11: Lorentzian fitted function of XRD-patterns of the as-prepared cluster samples (No.1-4) that was performed with Origin-Lab program in order to estimate the position of the diffraction peaks and FWHM-values.

Table 4.4: The XRD-diffraction peaks; the orientations for (111) and (200) planes of the as-prepared cluster samples (No. 1-4).

Sample No.	Position of (2θ) for Miller Planes	
	(111)	(200)
No.1	39.5587	44.7793
No.2	38.8698	44.5425
No.3	38.7513	45.0054
No.4	38.5145	45.2422

Table 4.4 shows the exact orientations for these two planes, (111) and (200) for cluster samples "1, 2, 3 and 4". Where, a small shifting to lower 2θ for the (111)-diffraction peaks is observed. The small shift may be attributed to the increase in the lattice parameter (d-spacing), which caused by the increase in the number of Mg (core) atoms, or by the increase in the clusters' size [57, 83, 144, 145].

The size of the clusters can be estimated by using Scherrers' formula [146]. In this work, the size is also estimated by using Scherrers' formula, (eq. 4.1) based on measuring the FWHM by Lorentzian fitted function of the main (111) diffraction peak in each XRD-pattern, figure 4.11. The estimated size in (nm) for as-prepared cluster of samples "1, 2, 3 and 4" are "ca. 1.2, 2.8, 2.9 and 5.5 nm", respectively. See table 4.5.

$$d = \frac{k\lambda}{\beta \cos \theta} \quad (4.1)$$

Where: the d estimates the diameter for the cluster in (nm), k is the shape factor and for dimensionless shape factor which has typical value to 0.94, λ is the X-ray wavelength which is here for CuK- α' (equal to 0.154051nm), β is the line broadening which is determined via FWHM of the most intense peak in radians, θ is the position of intensity maximum diffraction peak after divided by 2.

Table (4.5): The estimated size (in diameter) of as-prepared clusters; obtained from using Scherrers' formula for the fitted peak of (111) plane.

Sample No.	d_{XRD} [nm]
NO.1	1.188 (± 0.300)
NO.2	2.844 (± 0.179)
NO.3	2.860 (± 0.347)
NO.4	5.515 (± 0.127)

4.1.5 Energy Dispersed X-Ray of as-Prepared Samples

The elemental composition of the as-prepared cluster samples were analyzed by using line-profile EDX attached with SEM (SEM-EDX) and TEM (TEM-EDX).

Figure 4.12 shows the SEM-EDX of the four cluster samples. Qualitatively, SEM-EDX reveals: (i) Intense carbon and bromine peaks that corresponds

to the long chain of four "octyl-groups" and bromide anion for stabilizer (TOAB), respectively and (ii) Peaks for palladium metal.

No other elements (metals) were detected in cluster samples by this technique, except a trace of sulfur and oxygen elements, which is expected from precursor MgSO_4 -salt that was used in clusters preparation.

The absence of Mg-peaks from detection by SEM-EDX and the detecting of Pd-metal with (O and S) the counter ionic constituents of Mg precursor salt (MgSO_4) are in agreement with Mg-core and Pd-shell morphological clusters. This, may be because the (SEM) as a scanning technique is limiting for surface detection [147].

In figure 4.13, TEM-EDX shows all the peaks for all elements, originally has been detected by the SEM-EDX as well as the detection of Mg-metal that was not detected by SEM-EDX. This has a further evidence and additional proof of the Mg-core and Pd-shell morphology of the as-prepared clusters.

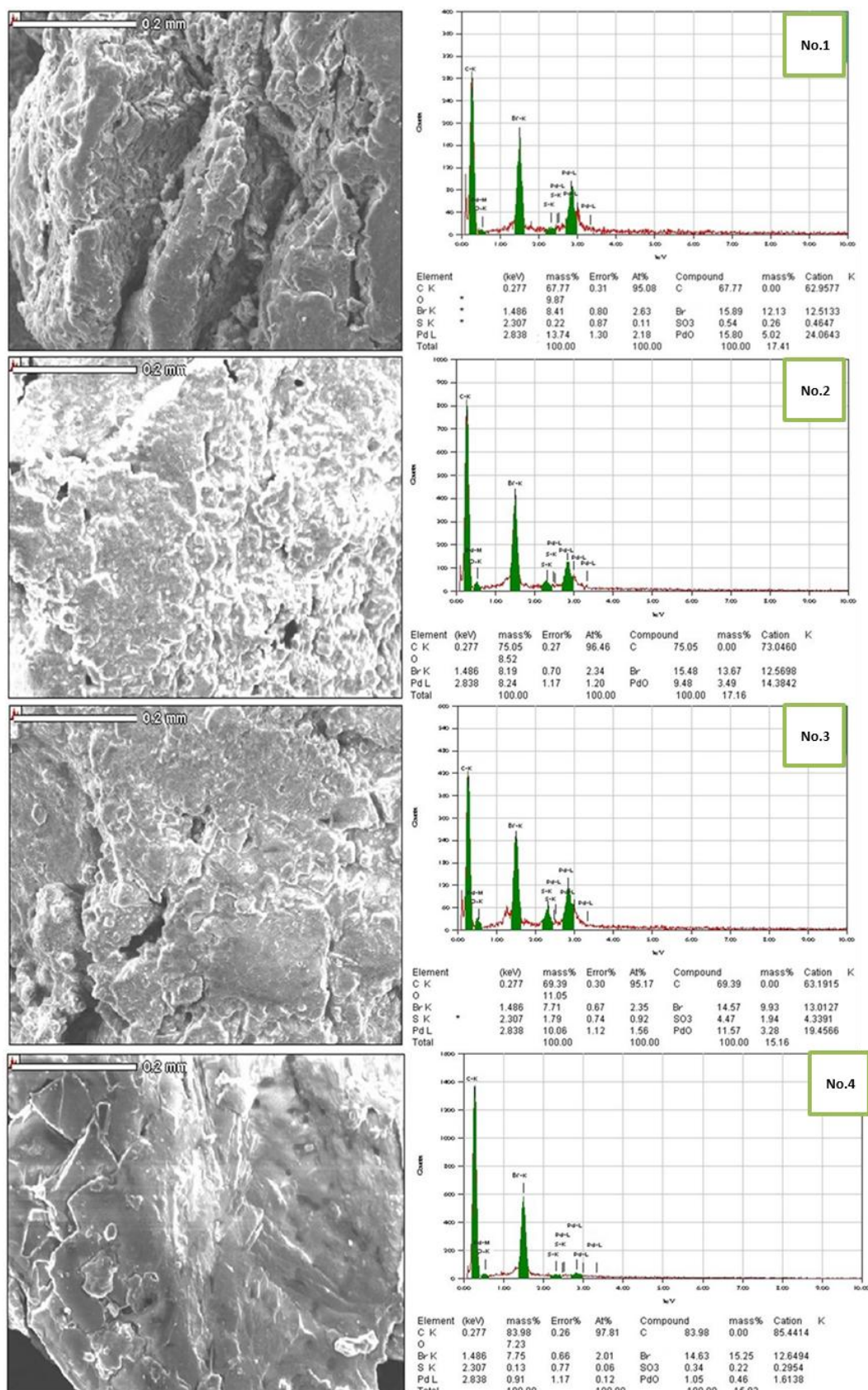


Figure 4.12: SEM-EDX profile of the as-prepared cluster samples (No.1-4).

Quantitatively, TEM-EDX can be used to estimate quantities and ratios of the elemental composition in cluster samples. Unlikely, the carbon detection peaks not only originated from the stabilizer (TOAB) but also from the Cu-TEM grid and the detected carbon is also from thin layer supports as from the TOAB, which makes the using of TEM-EDX as a quantitative method unreliable. Particularly, the calculations of one or more of the cluster component(s) quantities and ratios. Therefore, it will be limited "in this work" for the qualitative analysis of as-prepared cluster samples.

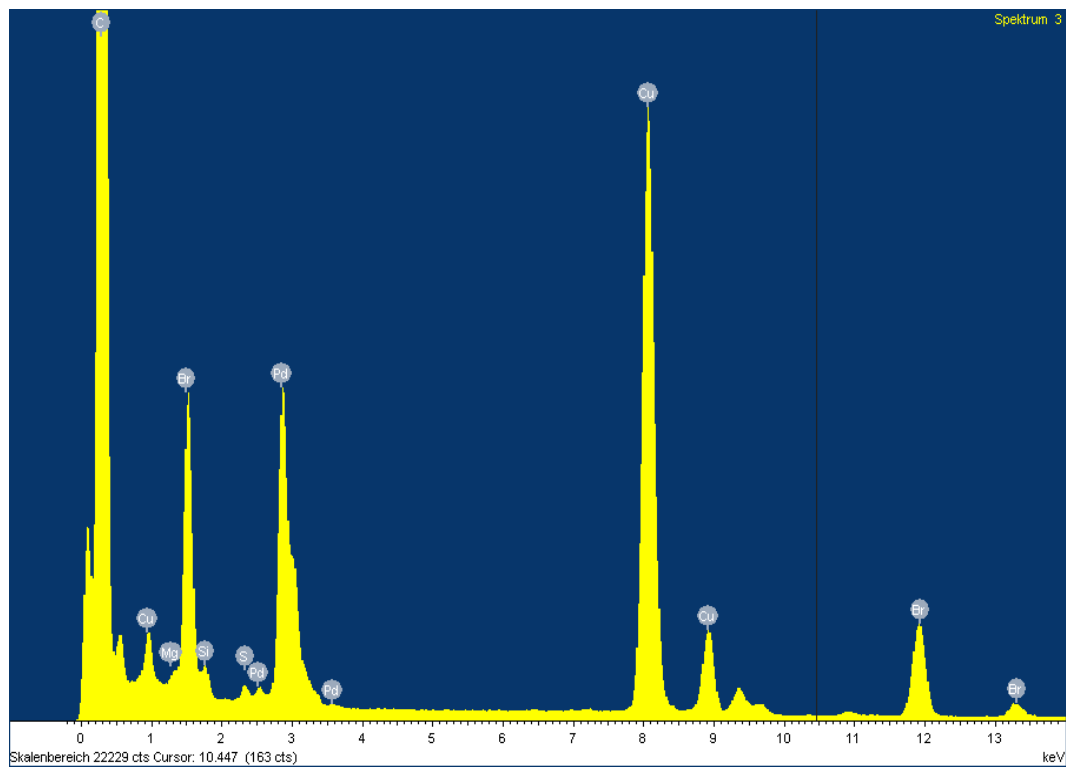


Figure 4.13: TEM-EDX profile of the as-prepared cluster sample (No. 2).

4.1.6 Atomic Absorption Spectroscopy of as-Prepared Cluster Samples

The quantitative elemental analysis, particularly the metal-compositions (of Mg and Pd) in the cluster samples are measured and obtained by atomic absorption spectroscopy (AAS).

Table 4.6 shows the pre-weight of each cluster sample that was used in preparation of the stock solutions and the obtained amounts (in ppm) of Pd and Mg in the clusters.

Table 4.7 shows the exact calculated weights (mg) and moles of Pd and Mg in the stock solutions of the as-prepared clusters. While, table 4.8 summarizes the weight percent (wt. %) of M-composition(s) of (Mg, Pd, and both metals Mg-Pd) and their mole-ratio (Pd:Mg) in each cluster sample, respectively.

Table 4.6: The exact wt. of as-prepared cluster samples was used in preparing the stock solution for analysis and the amounts of Pd and Mg have been detected (in ppm) by AAS.

Sample No.	Exact wt. cluster in the stock Solution[mg]	ppm of Pd	ppm of Mg
No.1	17.0	24.5304	0.8343
No.2	11.0	64.7079	4.9544
No.3	12.8	69.1808	11.9080
No.4	10.5	22.6698	4.0025

Table 4.7: The amounts of Pd and Mg (in mg) and (mmoles) that were obtained by AAS in as-prepared cluster samples.

Sample No.	Wt. Pd [mg]	Wt. Mg [mg]	Moles Pd [mmol]	Moles Mg [mmol]
No.1	1.22652	0.041715	1.15242×10^{-2}	1.7162×10^{-3}
No.2	0.647079	0.049544	6.07986×10^{-3}	2.0383×10^{-3}
No.3	0.691808	0.119080	6.50012×10^{-3}	4.8992×10^{-3}
No.4	0.226980	0.040025	2.1327×10^{-3}	1.6467×10^{-3}

Table 4.8: The wt. % of each metal (Pd and Mg) and the wt. % of the metallic composition in as-prepared cluster samples and their Pd:Mg mole-ratios.

Sample No.	Pd [wt.%]	Mg [wt.%]	Mg and Pd [wt.%]	Pd:Mg (mol ratio)
No.1	7.2148	0.2454	7.4602	6.71:1.00
No.2	5.8825	0.4504	6.3329	2.98:1.00
No.3	5.4048	0.9303	6.3351	1.33:1.00
No.4	2.1617	0.3812	2.5429	1.30:1.00

The % abundance ($(\text{moles of } M_1 / \text{moles of } M_{\text{Total}}) \times 100\%$) for Pd (and Mg) the metallic portion of clusters in the samples "1, 2, 3 and 4" were calculated and found to be equal to: 87.04% (12.96%), 74.89% (25.11%), 57.02% (42.98%) and 56.43% (43.57%), respectively.

The weight of organic portion "the stabilizer (TOAB)" was calculated by abstract of the weight of metallic portion from the total weight of cluster sample and found to be: 15.73, 10.30, 12.05 and 10.23 mg, which corresponds to % abundance: 68.93%, 69.88%, 65.91% and 88.19%, respectively.

Based on the calculated quantities of the both (Metallic and organic) contents of the as-prepared clusters. It was found that the most of the prepared clusters refers to the stabilizer with (% abundance) around 65-80 % with very low metallic "Mg and Pd" contents that increases with increasing either of the imposed current density (J) (which refers to Pd-metal with percent of 56-87 %) and/or the concentration of M-precursor (which refers to Mg-metal with percent of 44-13 %). Where, the samples "1, 2 and 4" with ($J = 1.5, 3.0$ and 5.2 mA.cm^{-2}) and the samples "2 and 4" with concentration of Mg-precursor equals to (0.022 and 0.049M) show an increasing in their M-contents, respectively.

Based on the AAS-calculations and the obtained Pd and Mg mole-ratio with the morphological structure of "Core/Shell (CS) type" that was defined for as-prepared clusters models were constructed to represent the stoichiometry between Mg-core and Pd-shell metals in the clusters. This is acceptable only with assuming that all formed clusters are not randomly alloying or monometallic clusters and just the CS-type coexists in our samples. This assumption is in agreement with the obtained

characterization of as-prepared cluster samples as confirmed by (TEM, XRD and EDX), sections (4.1.3 – 4.1.5).

Figure 4.14 shows the schematic image for our models that represented the stoichiometric CS-clusters and their TEM-obtained sizes of as-prepared clusters in our samples.

The Samples (1, 2, 3 and 4) were found to have clusters size with Mg-core and Pd-shell stoichiometry corresponds to: (1.65 nm with $\text{Mg}_{1.0}\text{Pd}_{6.7}$), (3.48 nm with $\text{Mg}_{1.0}\text{Pd}_{3.0}$), (3.60 nm with $\text{Mg}_{1.0}\text{Pd}_{1.3}$) and (4.56 nm with $\text{Mg}_{1.0}\text{Pd}_{1.3}$), respectively.

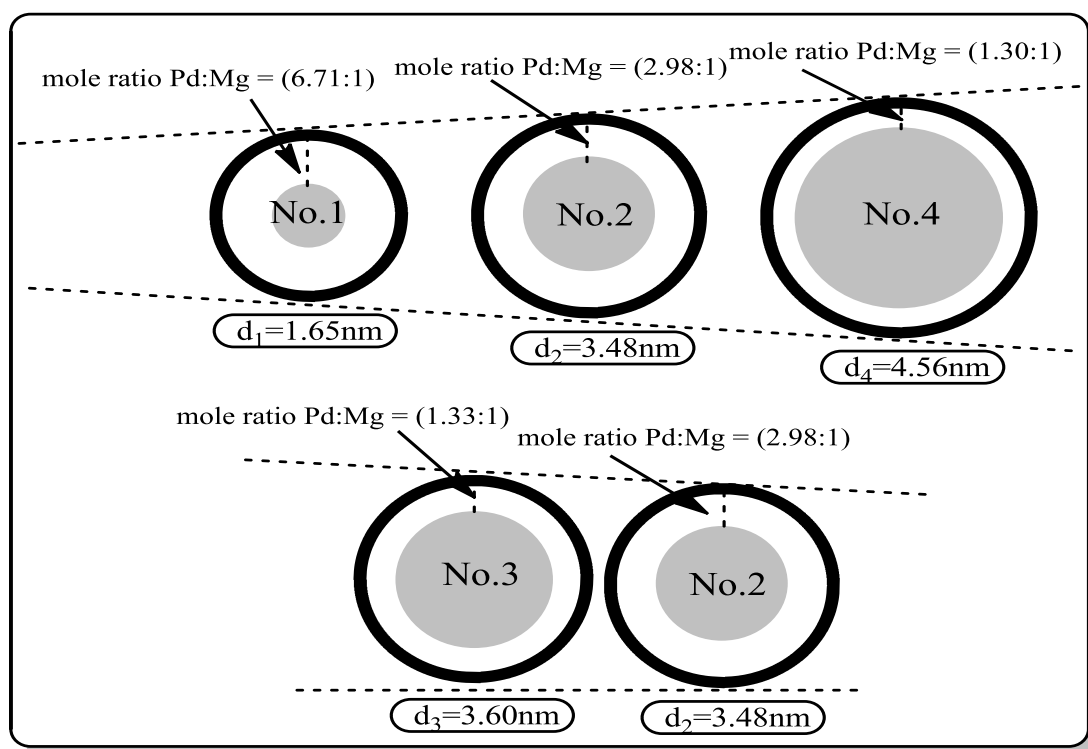


Figure 4.14: Schematic image describes the constructed models for the sizes and core to shell stoichiometry of the as-prepared clusters in samples (No. 1-4) that was obtained by TEM and AAS-data analysis, respectively.

4.1.7 UV-VIS spectroscopy of as-Prepared Cluster Samples

UV-Vis spectroscopy provides large evidences for the composites of clusters' surface and their optical and electrical properties that are through investigating the position and intensity of Surface Plasmon Resonance Band (SPRB) and by determination of their band gap energy (E_g).

The Theory of SPRB in colloidal nanosized particles is the resonance between the collective oscillations of the excited conduction electrons in the metal surface and the incident electromagnetic radiation., which was explained by Mie Scattered theory for the extinction coefficient (C_{ext}) "absorption and scattering" of the electromagnetic waves on the colloidal particle surfaces, which has direct proportional to the rather cubical of colloidal particles' size (d) and inversely proportional to irradiation wavelength (d^3/λ) [148].

The position of the SPRB depends mainly on the size and shape of the particles as well as the dielectric constant of the medium in which they are dispersed.

The band gap energy (E_g) is assumed to be plot at the maximum absorption band. It can be calculated by using the following formula (eq. 4.3) for the maximum absorbance peak of the UV-Vis spectra profile:

$$E_g \cong hc/\lambda \quad (4.3)$$

Where; E_g is the band gap energy, h is Plank's constant (6.6261×10^{-34} J.s), c is the velocity of light (2.9979×10^8 m.s⁻¹) and λ is the band gap's wavelength.

Suspension solutions from colloidal clusters were prepared, as mentioned in section 3.2.7, in order to study the optical properties of the as-prepared cluster samples.

The four colloidal clusters show ranging colored solutions from pale to dark brown, Figure 4.15. The brown color in the solutions was attributed to the zero-valent Pd-atoms as reported by N. Abderrafik and J. L. Rehspringer [149].

The absorption intensity of UV-Vis spectral profile of dark colored solution was higher than the lighter colored solution. The variances in absorption intensity can be explained by two factors: (i) increasing in the Pd-content and (ii) decreasing in the clusters size [35]. This is in agreement with the obtained data by TEM and AAS of the as-prepared clusters about their sizes and Pd-contents.

In figure 4.15, the whole UV-Vis spectra profile of the four cluster samples shows a broad and continues absorption rises in the background towards higher energies (lower wavelength), which highly matched the Pd UV-Vis spectrum was reported in literature. [125, 140, 149, 150].

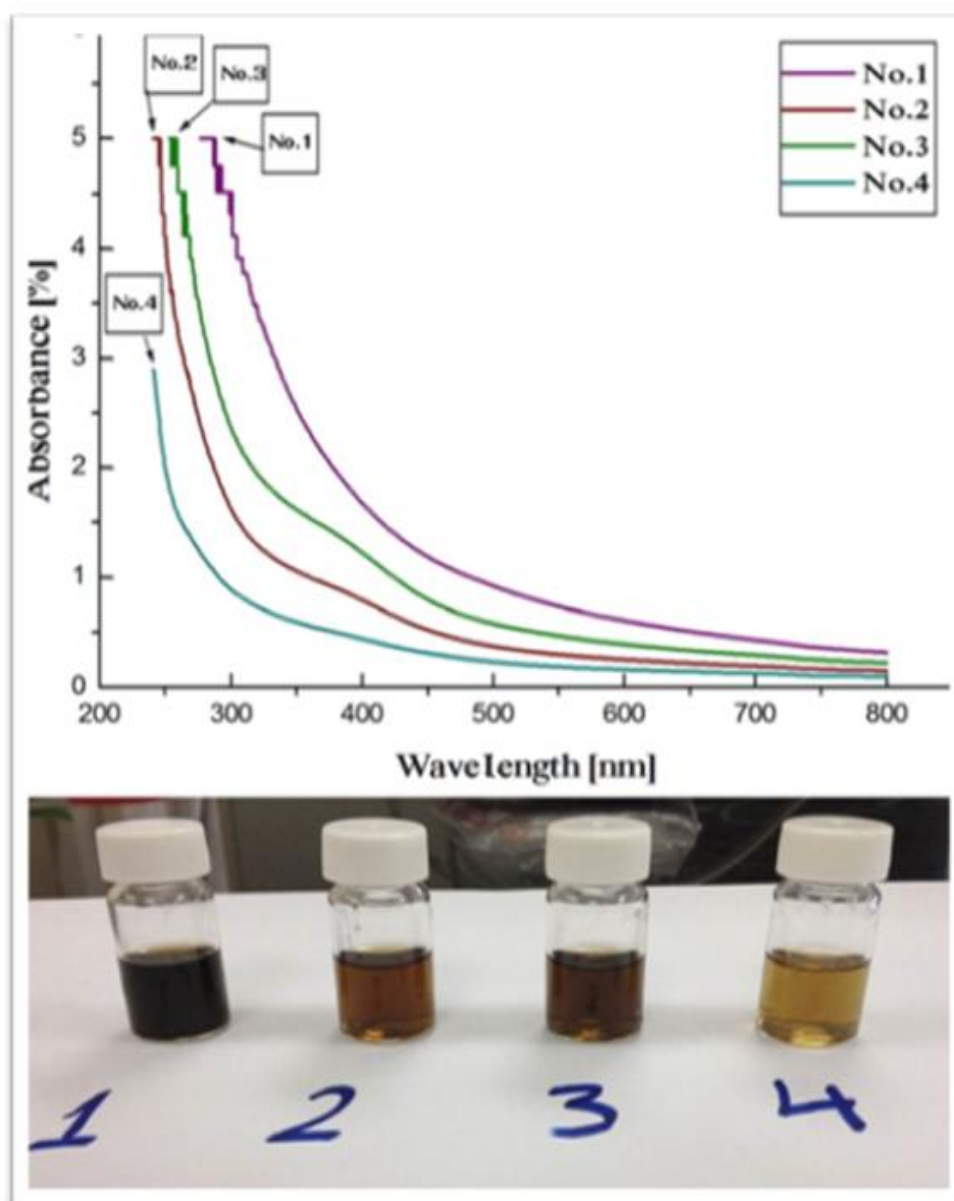


Figure 4.15: UV-Vis spectra profile of the as-prepared cluster samples (No. 1- 4), and downward the image for the solutions of the four cluster samples were prepared at same concentration.

Magnesium absorption profile often shows a wide and intense absorption band belongs to their SPRB at wavelength about 260-325 nm dependent on the particles' size, shape, structure, and if the surface of particles are merely of Mg-atoms or if it is oxidized [151, 152]. On the other hand, palladium has no absorption band in the bulk, but it observes a wide-small intense

band around 330-530 nm region upon the particles' size and shapes (cube, icosahedron ...etc.) [140,150].

Bimetallic nanoparticles (alloys) often show one characteristic plasmon band based on their composition [153]. In contrast, core/shell type is shown by two and more intense bands compared to their monometallic composites, the core metal plasmon band damped until disappeared if the shell layer is very thin (ca. 3-4 nm) and the only characteristic band in this case is for the shell metal, which is related to the excitation happening through the interactions between core and shell metals, in a model of formation a hybridized plasmon excitation between a sphere (core) and cavity (shell), that was obtained by Prodan et al., figure 4.16 [35, 153, 154]. On the other hand, as the shell is thick, the interactions between core and shell metals decreases even completely damped and in this case the two separate plasmon bands can be observed.

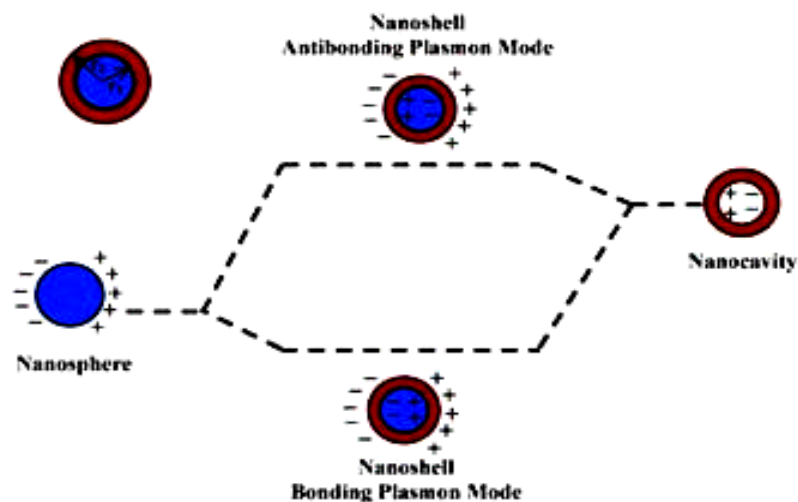


Figure 4.16: Schematic image for the hybridization model that describes the interaction between Core-sphere and Shell-cavity Plasmons and the formation of bonding and anti-bonding Plasmon modes. [35]

In figure 4.17, the UV-Vis spectra for as-prepared clusters is observed separately, their band's wavelength are determined and summarized in table 4.9 as well as the calculated band gap energy of as-prepared clusters bases on ($E=hc/\lambda$) equation was also summarized in table 4.9.

After extrapolation the UV-Vis spectra of the as-prepared clusters, only one absorption band for each spectral profile is shown. For cluster samples "2, 3, and 4" the wavelength of absorption band are 398.99, 392.41 and 382.48 nm, respectively. In the spectrum for cluster sample No. 1 no band was observed, which is expected because of its very small size ~ 1.6 nm, in which the quantum effect is predominant and no SPRB is observed for Pd-shell [148].

The observation of one plasmon band in the spectral profiles of as-prepared cluster samples, which was attributed for Pd-metallic clusters is in agreement with the CS-morphology with very thin Pd-shell, based on hybridization model that was obtained by Prodan et al. [35].

The blue shift in plasmon band by the samples "2, 3 and 4" is attributed to the high of interaction between Pd-shell and Mg-core as lowering of Pd-shell, which are in agreement with our model for the stoichiometry between Pd-shell and Mg-core, see figure 4.14. Otherwise, the clusters' size has an impact on the band gap energy, in which less sized particles show a blue shifting in the absorption band due to rising in their band gap energy [35].

In cluster samples "2 and 4" with size "ca. 3.5 and 4.6 nm", respectively, a red shift was observed. This contrast behavior of the size impact can be argued to the predominant core-shell hybridization effect. Particularly, if the difference between two clusters is narrow (~ 1 nm), hence the size impact is negligible.

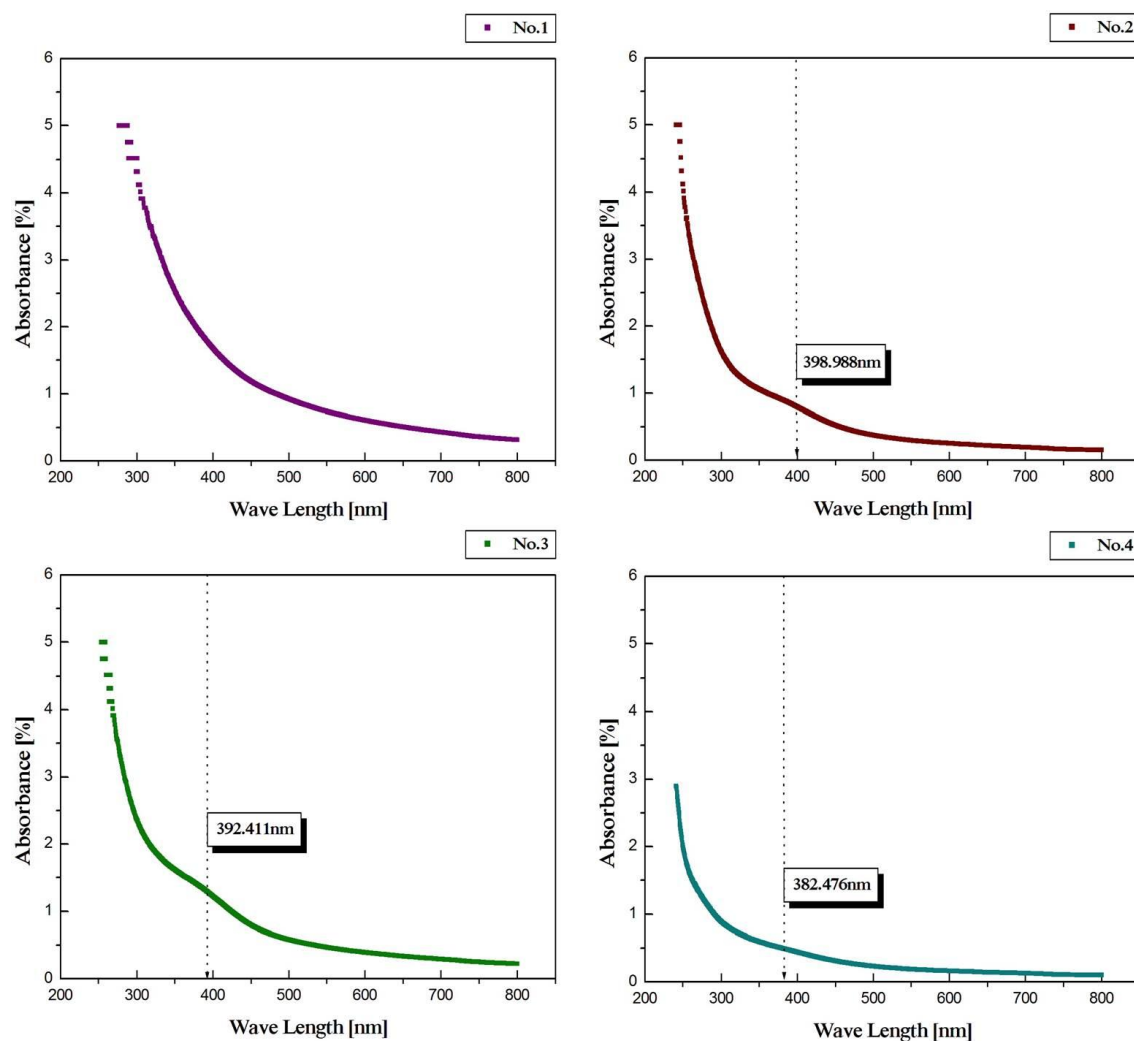


Figure 4.17: UV-Vis spectra profile the as-prepared cluster samples (No.1-4), the wavelength values of absorption band are characterized in order to use in measuring band gap energy.

Table 4.9: The wavelength of absorption band and the calculated band gap energy (in eV) of acetone dispersed as-prepared clusters.

Sample No.	Wave length [nm]	E_g [eV]	Size [nm]
No.1	-	-	1.6
No.2	398.988	3.108	3.5
No.3	392.411	3.160	3.6
No.4	382.476	3.242	4.6

4.1.8 Structure, Morphology and Crystallite of as-Prepared Clusters

In this work, the clusters morphology were investigated with combining and extrapolation all obtained results from characterization techniques "TEM, XRD and qualitatively by AAS, UV-Vis spectroscopy and (TEM and SEM) attached EDX" together.

TEM (in section 4.1.3) showed spherical small sized clusters almost attributed to the MgPd CS clusters, but the distinction of their morphology is impossible, because Pd (in the shell) are heavier metal and has more dense compact atoms than Mg (in the core) that shield the Mg from characterizing.

XRD-patterns almost attributed to the Pd crystallite, by the (111) and (200) diffraction planes for Pd cubic crystallite and the disappearance of the Mg-diffraction peaks are in agreement with CS-morphology, based on phenomenon of heavy atom effect.

Moreover, the shifting of the diffraction peaks to lower 2θ -values "increasing in the d-spacing" can be attributed to the increase in Mg-core atoms. The Mg leads to the enlargement and deformation on Pd-crystallite, review section (4.1.4).

TEM-EDX and AAS confirmed the CS-morphology in as prepared clusters, through the detection of the Mg-atoms that had not detected by SEM-EDX and did not confirmed by TEM or XRD, this is an indirect evidence for CS-morphology with Mg in the core.

Moreover, UV-Vis spectroscopy has farther evidences for CS-morphology by UV-Vis spectral profiles for Pd and one SPRB observation located at wavelengths that was attributed for Pd, review sections (4.1.5, 4.1.6 and 4.1.7).

All of the previous obtained feedbacks from the characterization techniques clearly confirm the CS morphology of as-prepared clusters with Mg-rich core and Pd-rich shell.

The quantitative analysis of the core to shell sized ratio were estimated by mole-ratios between Pd and Mg with stoichiometry of ($\text{Mg}_1\text{Pd}_{6.7}$, $\text{Mg}_1\text{Pd}_{3.0}$, $\text{Mg}_1\text{Pd}_{1.3}$ and $\text{Mg}_1\text{Pd}_{1.3}$ for cluster samples "1, 2, 3 and 4", respectively. This only, if assumed that all the formed cluster samples have the CS morphology, with no alloying or monometallic formation. This analysis is in well-agreement with the extrapolation of the characterization techniques.

4.1.9 Size and Size-Distribution of as-Prepared Clusters

The sizes of as-prepared clusters were estimated by two methods, the TEM and XRD.

The obtained size by XRD was estimated using Scherrers' equation, after measuring the full width at the half maximum (FWHM) of the most intense diffraction peak, the (111) orientation plane, section (4.1.4). While, the obtained size and size-distribution of as-prepared clusters by TEM were measured by counting the diameters of the most clarified and visible particles. Thereafter, a size-histogram was constructed. The peak and FWHM of the constructed histograms are corresponding to the clusters size and size-distribution, respectively.

Table 4.10 summarizes the sizes "in diameter" of the as-prepared clusters that was obtained and measured by using TEM and XRD. The differences between the size-values that obtained by both methods can be assigned to the broadening in the fitted diffraction peak for XRD Patterns, which causes a slight deviation for the size calculations.

Depending on the obtained results by TEM and XRD, in table 4.10, it is noted that the clusters' size are up to 5 nm with near to mono-sized distribution (approximately 1 nm)

Table 4.10: The Clusters' size and size-distribution of the as-prepared clusters that obtained by TEM and XRD.

Samples	d_{TEM} [nm]	d_{XRD} [nm]	(TEM-obtained) Size-Distribution [nm]
NO.1	1.651 (±0.064)	1.188 (±0.300)	0.877 (±0.719)
NO.2	3.476 (±0.032)	2.844 (±0.179)	0.936 (±0.178)
NO.3	3.600 (±0.011)	2.860 (±0.347)	1.272 (±0.100)
NO.4	4.558 (±0.027)	5.515 (±0.127)	0.850 (±0.201)

4.1.10 Influence of the Electrolysis Parameters

In present, selective clusters preparation methods with manipulating to their sizes and shapes are an attractive field of science. One of these selective methods is the electrochemical technique. Where, the selective clusters preparation will be achieved by manipulating in one or more of their parameters, i.e. current density, concentrations of solution mixtures, reaction time and distance between electrodes ...etc.

In this work, only two parameters were studied, the current density and the concentration of Mg "the core metal" precursor.

Figure 4.18 shows the varying in the current density impact on the size of as-prepared clusters in samples (1, 2 and 4). In which increasing the current density (1.6, 3.0 and 5.2A.cm⁻²) leads to the production of smaller sized clusters (ca. 4.5, 3.5 and 1.6nm), respectively. (See figure 4.18 and table 4.11).

The effect of Mg-precursor concentrations on the clusters size was investigated. In this work we found that, duplicate the magnesium salt

concentration with fixing all other parameters increase the clusters size. In samples "2 and 3" increasing the concentration of Mg (0.022 and 0.049M) leads to a slight increase in clusters size (3.5 and 3.6 nm), respectively. See table 4.11.

The interpretation of these two parameters are as follows; the low imposed current density leads to low reaction rate (by slow anode oxidatively dissolution), which caused to the formed ad-atoms at a later period to collide with the nuclei that have already formed instead of forming new nuclei "Recrystallization due to inelastic collisions". This in turn leads to the formation of larger sized particles. On the other hand, as the imposed current density increases due to the increasing into reaction rate, a greater number of nuclei will be formed. This leads to the formation of smaller sized particles [26]. These interpretations are in agreement with the increasing in d-spacing or the blue-shift observed by XRD and UV-Vis spectral profiles, respectively. Moreover, are also in agreement with the stoichiometry of Pd and Mg obtained by AAS, and was summarized as a model in figure 4.14.

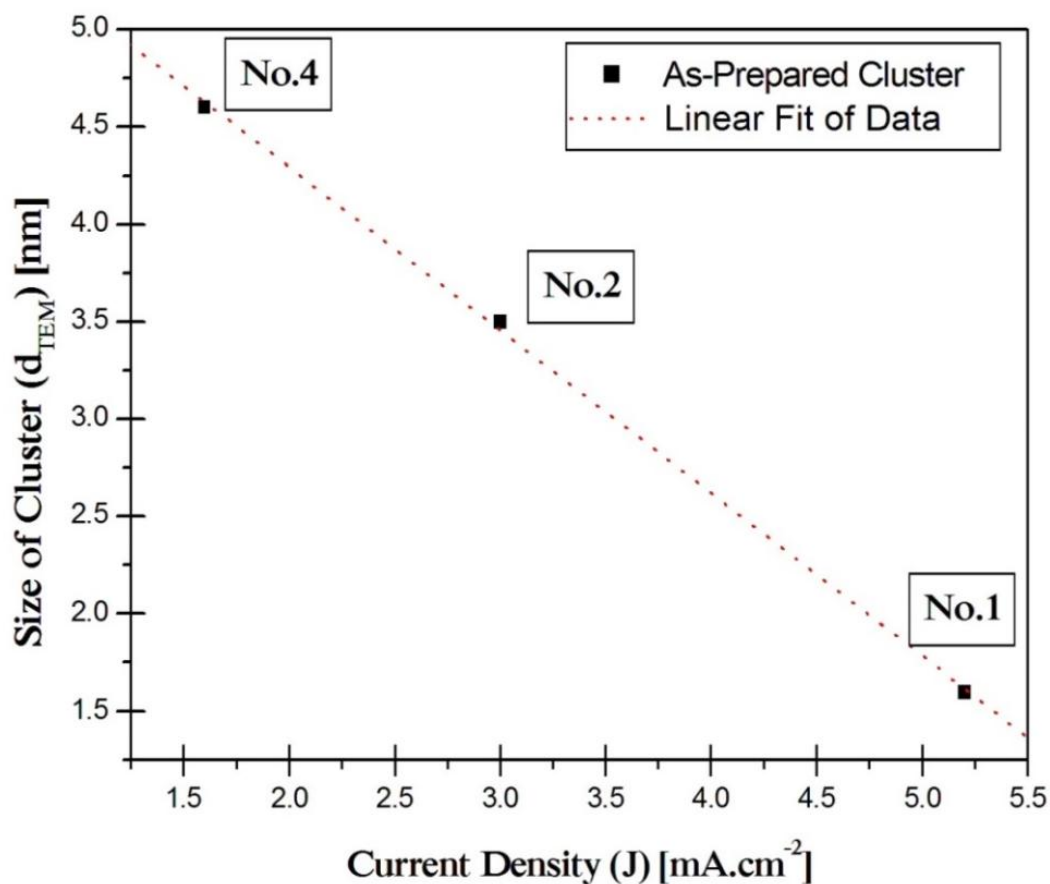


Figure 4.18: The effect of the current density (J) on the TEM-obtained size of the as-prepared clusters.

Table 4.11: The electrochemical preparation parameters (J and C_{Mg}) and the obtained characterization properties (size, E_g , and Pd:Mg mol-ratio) by different characterization techniques (TEM, UV-Vis spectroscopy and AAS) of the four as-prepared clusters.

	J [mA.cm ⁻²]	C_{Mg} [M]	Size[nm]	E_g [eV]	Pd:Mg [mol-ratio]
1	5.2	0.022	1.7	-	6.71:1
2	3.0	0.022	3.5	3.108	2.98:1
3	3.0	0.049	3.6	3.160	1.33:1
4	1.5	0.022	4.6	3.242	1.30:1

4.2 Hydrogen Storage Measurements of as-Prepared Clusters

The hydrogen storage measurements of as-prepared clusters were obtained by using a couple of manners "Volumetric and Gravimetric", which were performed by using the designed and furnished Sieverts' (Volumetric) apparatus that was done for this work and ultra-high vacuum electronic microbalance (UHVEM), respectively.

The volumetric apparatus was used to investigate the H-storage capacity of as-prepared clusters (in (H/M) wt %) after loading about 1 bar of H-pressure and monitoring the amount of pressure decline after a period of time (~2 h's), where the equilibrium of hydride formation has not accessed. On the other hand, UHVEM was used to investigate the H-storage measurements from both points of view "Thermodynamic by PCI and Kinetic" that was obtained from sample No. 2 their clusters' size (ca. 3.5 nm) and stoichiometry of (Mg_1Pd_3).

4.2.1 Hydrogen Volumetric Measurements

The volumetric measurements of hydrogen absorption in as-prepared clusters were obtained by using high-vacuum apparatus that was designed and furnished for this MSc. work, section (3.4.2).

The stability test for the apparatus under loading about 1bar of H-pressure is shown in figure 4.19, which shows a stable hydrogen loading into the setup during time progressing (about 2 h's) with no leakage in or out.

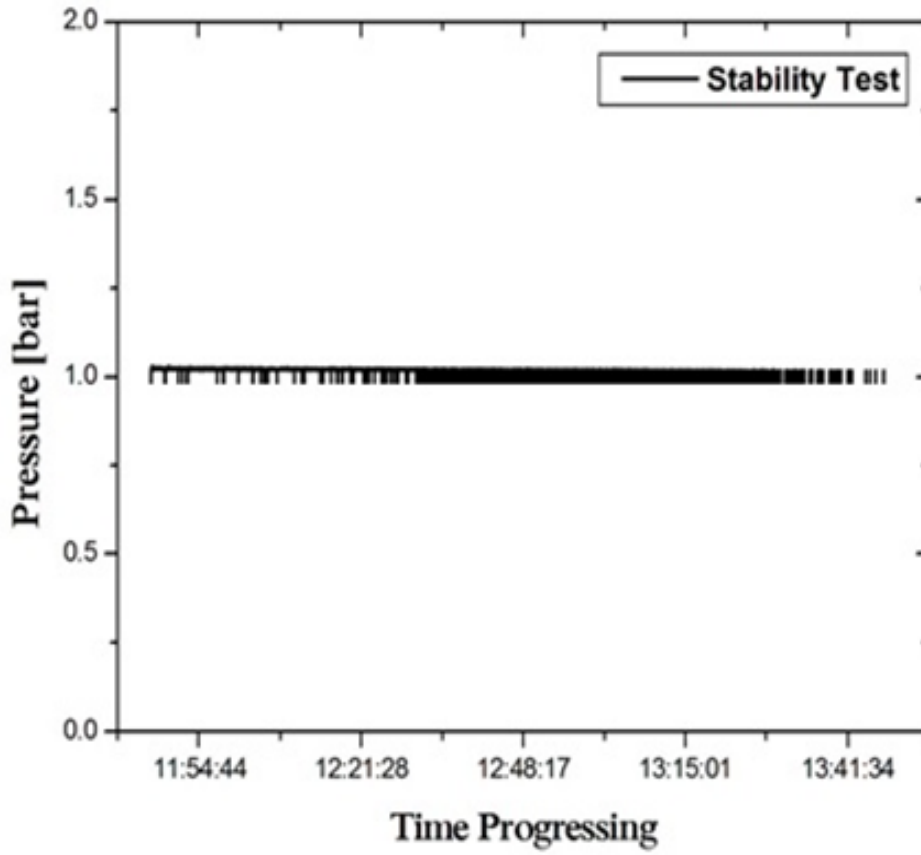


Figure 4.19: The stability profile for the volumetric apparatus under approximate 1bar of H-loading.

Figure 4.20 shows the hydrogen absorption on cluster samples at ambient temperature (about 25°C) and pre-treated (evacuated) for 5 h's before the H-loading. About 1bar of hydrogen gas was loaded to cluster samples "1, 2, 3 and 4" with weight of "0.989, 1.101, 1.018 and 0.853 g", respectively. After about 2 h's the pressure drop was measured and the amount (weight) of absorbed hydrogen was calculated by using the ideal gas law, (eq. 4.4).

$$W_H = \frac{\Delta PV}{RT} \times Mwt_H \quad (4.4)$$

Where: W_H is the weight of absorbed hydrogen, V is the dead volume of the measuring chamber (equal to 0.144 L), R is a constant (0.08205 atm.L.mol⁻¹.K⁻¹), T is the absolute temperature and Mwt_H is the molecular weight of hydrogen atom.

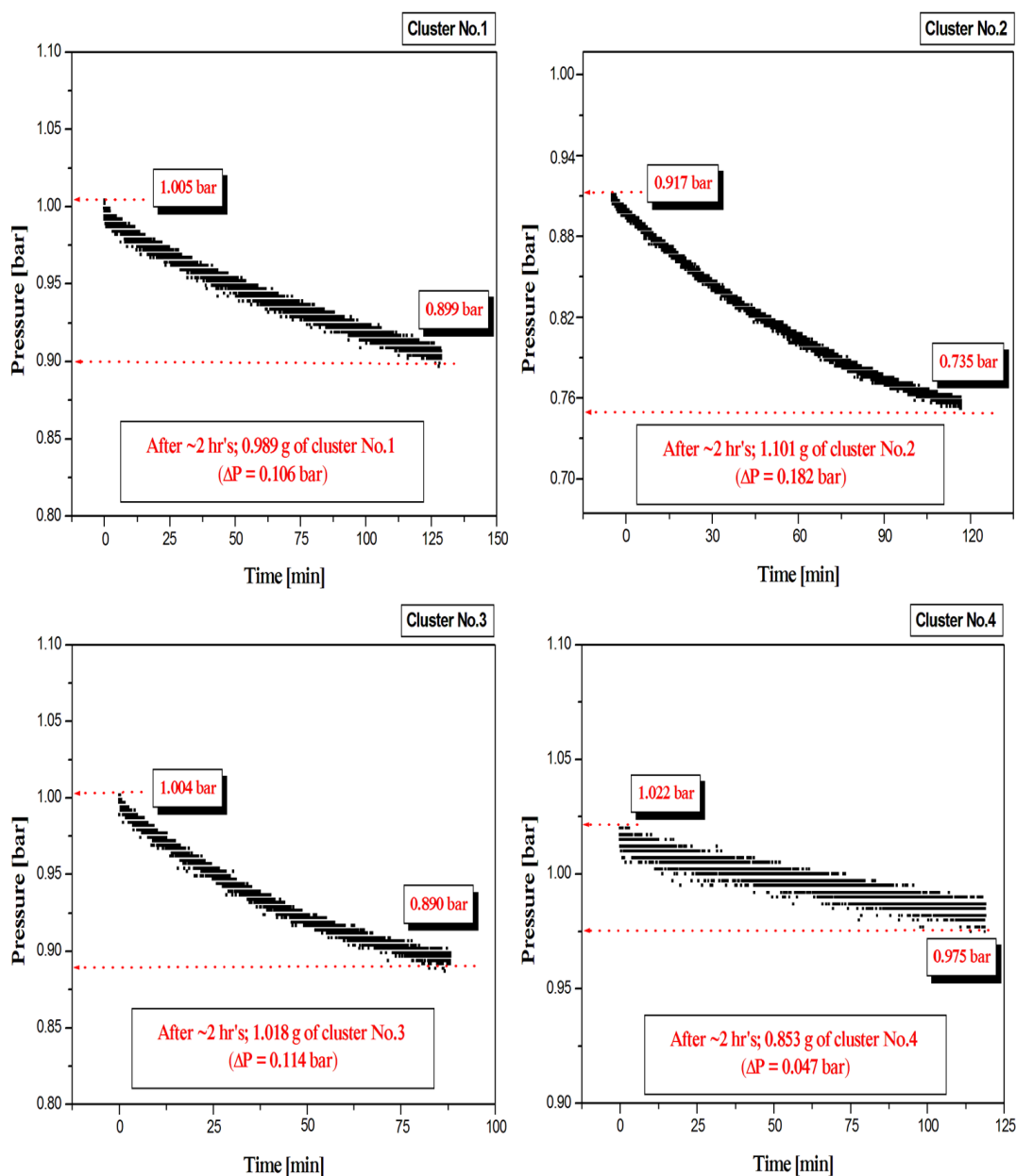


Figure 4.20: Volumetric profile of H-absorption of the as-prepared cluster samples (No.1- 4) after loading with approximate 1bar of H_2 gas at ambient temperature. The drop in the pressure value during time progressing are corresponding to the amount of absorbed hydrogen by a certain weight of cluster sample.

Table 4.12 summarizes the details about the conditions of each cluster sample and the calculated weight of absorbed hydrogen by the clusters as well as the used weight of clusters and their metal-contents, which

calculated dependent on the wt. % of Mg and Pd in the cluster samples that was obtained by using AAS, in section 4.1.6.

Table 4.12: The properties "size and stoichiometry" of the as-prepared clusters and the obtained pressure difference and (H/MgPd) wt % of these studied clusters.

	No.1	No.2	No.3	No.4
Wt. of Cluster [g]	0.989	1.101	1.018	0.853
Wt. of M-Content [g]	0.074	0.070	0.065	0.022
ΔP [atm]	0.105	0.180	0.113	0.046
Wt. of H_{abs} [g]	6.230x10 ⁻⁴	1.068x10 ⁻³	6.705x10 ⁻⁴	2.729x10 ⁻⁴
Wt% of (H/M)	0.84%	1.53%	1.03%	1.24%
d_{TEM} [nm]	1.7	3.5	3.6	4.6
Pd:Mg - stoichiometry	6.7:1	3.0:1	1.3:1	1.3:1

Table 4.12 shows that the obtained (H/M) wt % of cluster samples "1, 2, 3 and 4" are "0.84, 1.53, 1.03 and 1.24 %", respectively.

The less H-storage capacity was in sample No.1 that can be attributed to their very small size (ca. 1.7 nm). The lowering in H-storage capacity with decreasing the size is in accordance to other reports [83, 84].

In the samples "2 and 3" that have approximately the same clusters size "ca. 3.5 and 3.6 nm and shell to core mole-ratio of 3.0:1 and 1.3:1, respectively", the lowering in H-storage capacity can be attributed to the

lowering of the shell thickness "lowering the core to shell ratio", which we attribute to the influence of the interface between the core –shell and to its composition and size.

The increasing in H-storage capacity for sample No.4 (clusters' size ca. 4.5 nm with stoichiometry of Mg_1Pd_3) in comparison with sample No.3 (clusters' size ca. 3.6 and stoichiometry of Mg_1Pd_3) can be explained by the size effect, where larger sized clusters uptake higher amounts of hydrogen.

4.2.2 Hydrogen Gravimetric Measurements of as-prepared Clusters **" Size of 3.5 nm and Mg_1Pd_3 stoichiometry"**

In this section, all the experimental results for the hydrogen absorption and desorption kinetics and pressure-concentration isotherms for clusters in sample No.2, which was performed gravimetrically by using ultra high-vacuum electronic microbalance will be presented and discussed.

4.2.2.1 Pressure-Concentration (Composition)-Isotherm (PCI)

The pressure-concentration isotherm (PCI) for hydrogen absorption (or desorption) in cluster sample No.2 was obtained using gravimetric method by loading (or unloading) stepwise of particular hydrogen pressure in the measuring chamber.

Monitoring of the variation in the specimen's weight during time progressing; a plateau in the curve "no changing in the sample weight during time progressing" for each loading (or unloading) step that can be

detected after a period of time corresponds to the reached equilibrium between hydrogen absorption (or desorption) at that particular pressure. When equilibrium is reached, the amount of absorbed (or desorbed) of H-atoms "in mass unit" can be measured by the weight difference before and after each loading (or unloading) step, which will be used to construct the PCI isotherm.

Figure 4.21 shows a snapshot image for the real experimental profiles of (A) hydrogen loading and (B) hydrogen unloading steps. The weight difference in each loading (or unloading) step denoted with ($\Delta wt.$) are corresponding to the amount of hydrogen has absorbed (and desorbed) by cluster sample, respectively.

Figure 4.22 shows the PCI for H-absorption (and desorption) that constructed from the reached equilibrium points of each loading (and unloading) steps, respectively.

The loading pressure is (up to ~ 1 bar) on (0.128 g) of cluster sample with weight of M-contents "Mg and Pd" (ca. 8.1062 mg) corresponds to (9.4466×10^{-2} mmol), which was done isothermally at constant temperature (about 25°C).

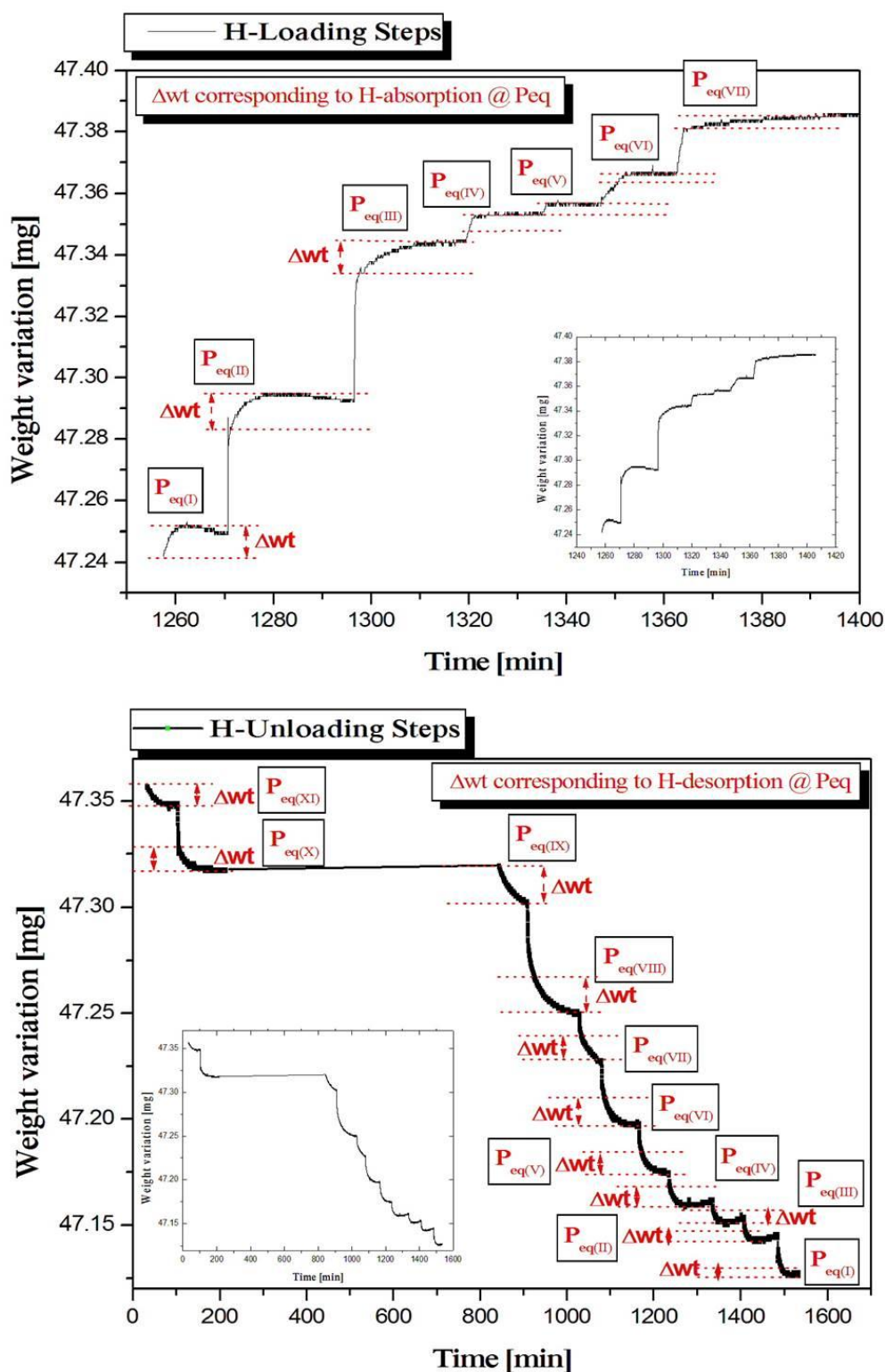


Figure 4.21: H-loading (A) and Unloading (B) profiles of the Gravimetric measurements for as-prepared cluster sample (No.2) have (clusters' size ca. 3.5 nm and Mg_1Pd_3 stoichiometric formula). The left y-axes show the amount of hydrogen absorbed and desorbed at different hydrogen pressure loading and unloading steps per time progress in minutes (x-axes).

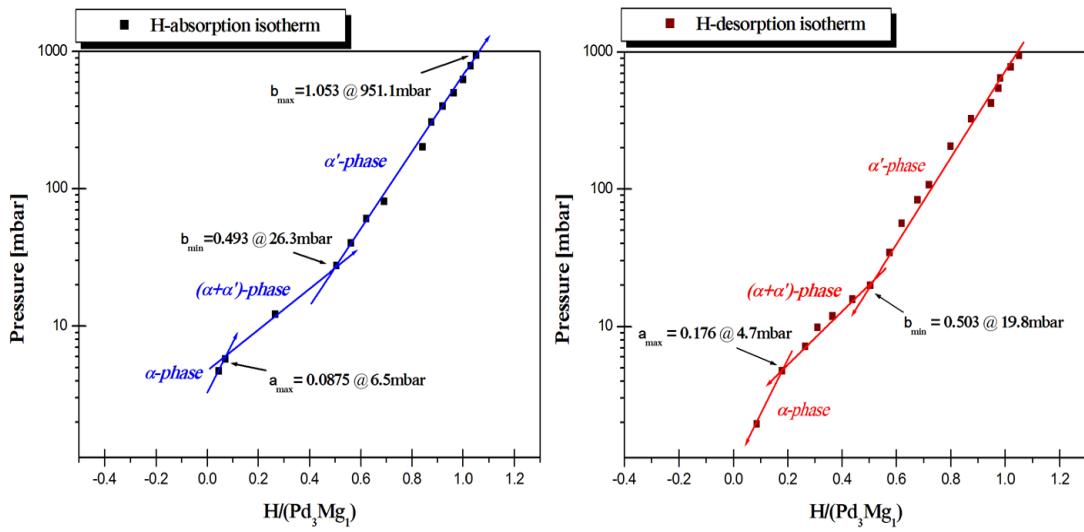


Figure 4.22: PCI of the as-prepared cluster sample (No. 2) with (clusters, size ca. 3.5 nm and Mg₁Pd₃ stoichiometric formula). The blue-colored curve is H-absorption isotherm. The red-colored curves for the H-desorption isotherm.

The constructed PCT-isotherms of MgPd-H systems of cluster sample No. 2 (with size ca. 3.5 nm and Mg₁Pd₃ stoichiometry) indicates the three phase regions coexists: (α -phase, transition ($\alpha+\alpha'$)-phase and α' -phase regions) that are similar to Pd-H systems, figure 4.22.

The anhydride phase (α -phase) is observed up to 6.5 mbar, with α_{\max} ca. 0.0875. Then, the hydride phase (α' -phase) starts in growing with a significant H-absorption by the clusters at slight pressure loading. In this case the transition phase between α -phase and α' -phase are in growing and two-phase region (the miscible gap ($\alpha+\alpha'$)-phase region) are observed.

After the absorption has reached the pressure value of 26.3 mbar, all the anhydride phase has been transformed into the hydride phase, with α'_{\min} ca. 0.493. Thereafter, the metal hydride was formed and α' -phase is observed as slight H-absorption with high pressure loading. The maximum

H-absorption (α'_{\max}) at pressure up to 951.1 mbar corresponds to (H/M) ca. 1.053.

The H-desorption isotherm is highly similar to H-absorption isotherm about three phase regions coexists. Except in the miscibility gap region, this occurred at lower pressure than the H-absorption isotherm. Where, it started at α'_{\min} and α_{\max} corresponded to H/M ca. 0.503 and 0.176 at pressures up to 19.8 and 4.7 mbar, respectively, figure 4.23.

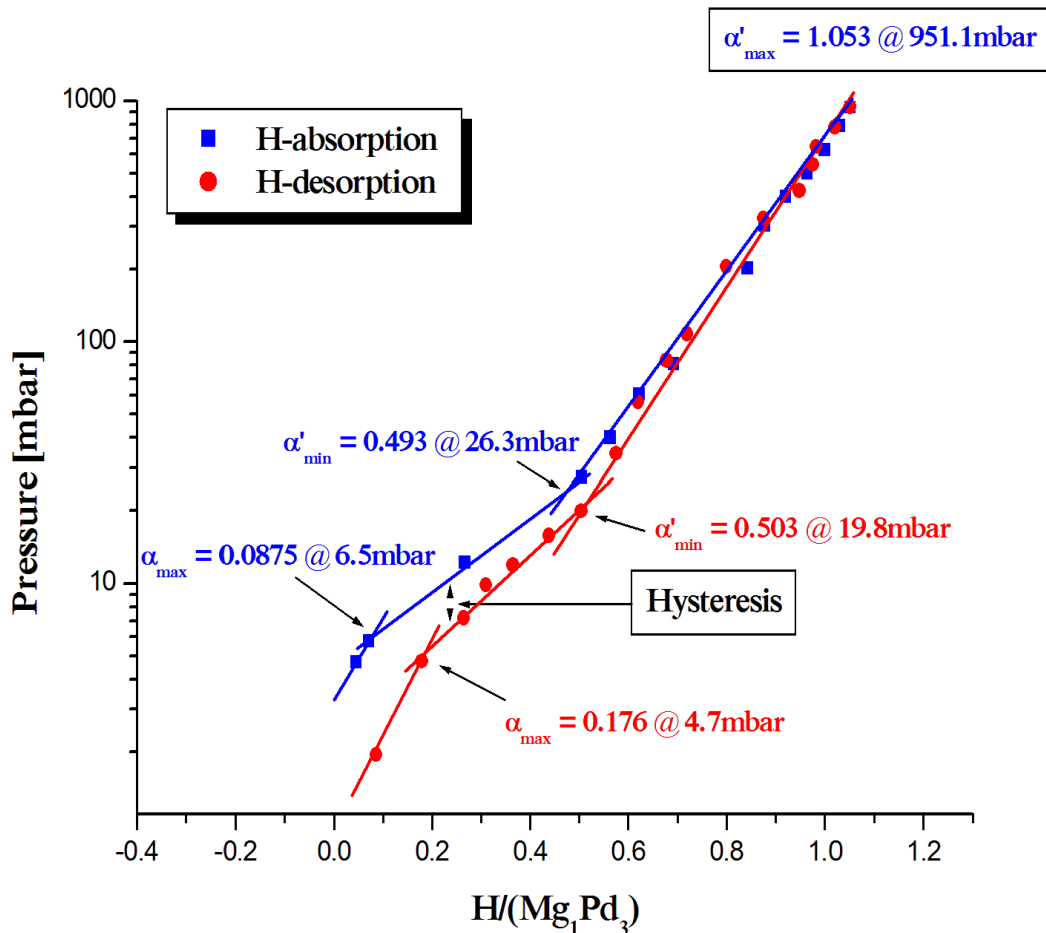


Figure 4.23: The hysteresis between the absorption-desorption isotherms of the as-prepared cluster sample (No. 2).

A sloped plateau in miscibility gap region is observed in both of hydrogen absorption and desorption isotherms. This is in the PCI for small sized systems "nanoparticles and clusters" and is reported in several literature [30, 57, 83, 85]. The reasons behind this sloped plateau in miscibility gap region were mentioned in the introduction of this thesis with some details, as reported in section (1.2.2.1, p 38).

The hysteresis between the absorption and desorption isotherm is considered the check point for the phase transitions that was reported by M. Suleiman et.al [57, 85]. Therefore, our M-H systems shows a small hysteresis between both isotherms (H-absorption and desorption) and this confirms the (α - α') phase transition in PdMg-H system, which is typical for Pd-H system. All the obtained data from hydrogen absorption and desorption isotherms are summarized in table 4.13.

The hydriding of the cluster sample No.2 is in hydride stoichiometric formula of ($\text{Mg}_1\text{Pd}_3\text{H}_{4.2}$) with hydrogen gravimetric storage capacity (H/M) wt. % (ca.1.22 %), which is higher than the storage capacity of Pd-H system (ca. 0.56 %) that was reported in literature [30, 84, 87] with an enhancement up to 2 folds in the H-storage capacity.

The hydriding of as-prepared cluster "size 3.5 nm and Pd:Mg equal to 3:1" happened with phase transition from anhydride phase (α -phase) to hydride phase (α' -phase) with α_{\max} and α'_{\min} (ca. 0.09 and 0.49, respectively) which are larger than the obtained for Pd-H systems that was reported by

Suleiman et al., the α_{\max} and α'_{\min} of 3.6 nm Pd-clusters are (ca. 0.07 and 0.15), respectively [43].

Higher miscible-gap pressure for H-absorption and desorption P_{abs} and P_{des} equal to (1.6×10^3 and 1.2×10^3 Pa, respectively) and lower hysteresis amplitude " $P_{\text{abs}}/P_{\text{des}}$ " of (ca. 0.134) for Mg_1Pd_3 system are also observed when compared with Pd-H systems with P_{abs} and P_{des} are (ca. 1.3×10^3 and 7.1×10^2 Pa) and hysteresis ranging from (0.183-1.950), respectively [43].

Table 4.13: The H-properties for the (as-prepared cluster No.2) with clusters size 3.5 nm and M-stoichiometry of Mg_1Pd_3 that was obtained from the PCI for Hydrogen absorption-desorption processes.

	<i>H-absorption Isotherm</i>		<i>H-desorption isotherm</i>	
	$\frac{\text{molH/molM}}{\text{(H/Pd}_3\text{Mg)}}$	P_{abs} [mbar]	$\frac{\text{molH/molM}}{\text{(H/Pd}_3\text{Mg)}}$	P_{des} [mbar]
α_{max}	0.0875	6.5	0.1760	4.7
α'_{min}	0.4930	26.3	0.5030	19.8
α'_{max} (max H_{abs})	1.0530	951.1		

Moles H_{abs} in Cluster	4.1909
(Wt. H / Wt. M)%	1.2176%
hydride	$\text{MgPd}_3\text{H}_{4.2}$

	$\theta_{\text{(abs)}}$	P_{abs}	$\theta_{\text{(des)}}$	P_{des}
Miscibility gap slop (θ°)	88.83°	16.40	88.76°	12.25
Hysteresis ($P_{\text{abs}}/P_{\text{des}}$)	1.3388			

4.2.2.2 Hydrogen Absorption and Desorption Kinetics

In this section, the gravimetric measurements for hydrogen absorption-desorption kinetics in as-prepared cluster with stoichiometry of (Mg_1Pd_3) and (size = 3.5 nm) will be presented.

The kinetic measurements were performed under pressure up to 1 bar and ambient temperature (25°C).

Figure 4.24 shows the loading and unloading processes with about 1bar of hydrogen, the loading and unloading rates are (90 and 180 mbar per

minute, respectively) for sample No.2, (with weight of M-content's about 8.106 mg).

The cluster sample absorbs the maximum weight of hydrogen (ca. 0.098 mg) in approximately (8 min) and desorbs effectively in just (4 min). These measurements reflects the high efficiency of as-prepared clusters to absorb and desorb hydrogen reversible with high rate under ambient conditions (pressure and temperature) in comparison with other M-H systems (M= Mg and Pd) reported in literature [30, 57, 83, 85].

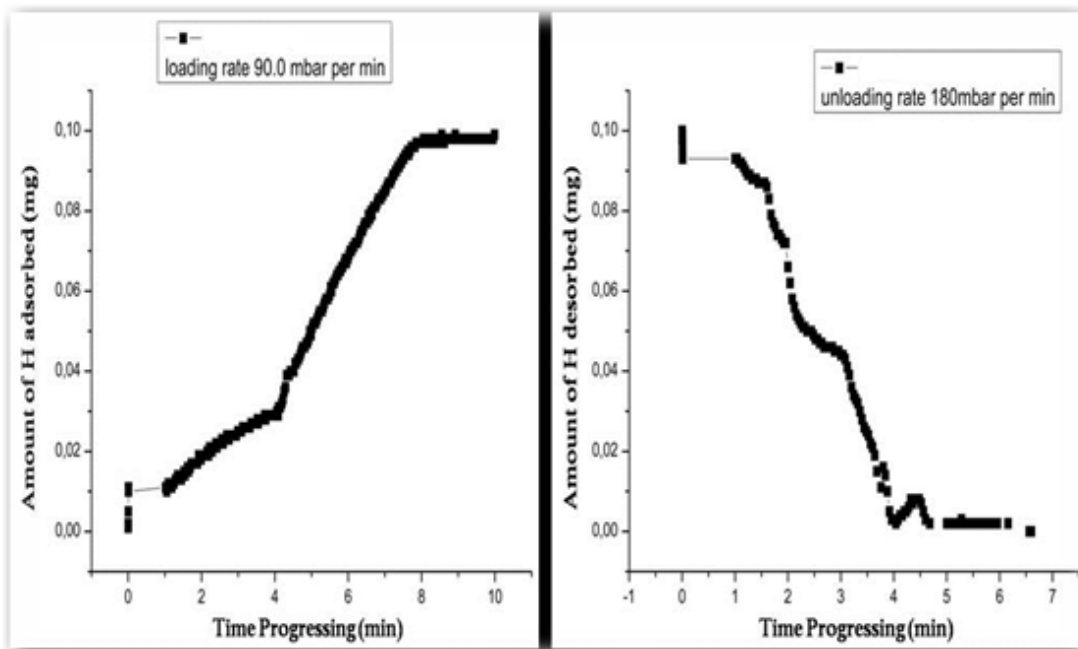


Figure 4.24: H-absorption (left-hand side) and desorption (right-hand side) of as-prepared Cluster sample (No. 2) with (Mg_1Pd_3) stoichiometry and size ca. 3.5 nm) that obtained at ambient conditions 298 K and 1bar (0.1MPa).

Finally, hydrogen "volumetric" studies on as-prepared clusters can be concluded as the prepared clusters of "MgPd CS-morphological structure" and sizes up to 4.6 nm absorbs hydrogen with (H/M) wt. % ranging from

0.89 % - 1.52 % depending on the clusters size and/or metallic composition under proper conditions (1 bar and 25°C).

The thermodynamic and kinetic studies were performed by gravimetric measurements on cluster with size ca. 3.5 nm and stoichiometric formula of Mg_1Pd_3 , which absorbed about 1.22 (wt. %) of hydrogen and formed a metal hydride with stoichiometric formula of $\text{Mg}_1\text{Pd}_3\text{H}_{4.2}$.

The constructed PCI showed that the cluster has three characteristic phase regions well-known for Pd-H systems with slightly extended miscibility gap to higher pressure and less hysteresis amplitude than Pd-H systems. Moreover, the kinetic study showed that the cluster has high efficiency and reversibility for hydrogen absorption and desorption processes. Where, it absorbs and disorbes the total amount of hydrogen completely during few minutes under ambient conditions.

To the best of our knowledge, H-storage capacity in as-prepared clusters of Mg-Pd CS morphology shows large enhancements for their H-storage capacity (more than 2 folds) than monometallic Pd-clusters or any other Mg-Pd systems reported in literature [72, 94, 95, 118-123], as indicated in the sections (2.1-2.3).

Conclusions

1- Core-Shell Mg-Pd bimetallic clusters were successfully synthesized in this work:

- Size selective synthesis in range of "1.6-4.5 nm" with very narrow size-distribution was obtained by varying the preparation parameters: current density and Mg content.
- The size and structure determination of the obtained samples were achieved by: analysis of X-ray diffraction "XRD" and transmission electron microscopy techniques "TEM". XRD confirm (*fcc*) structure for all prepared clusters.
- The elemental composition determination was done by energy dispersive X-ray "EDX" and atomic absorption spectroscopy "AAS" techniques, shows Mg-rich core and Pd-rich shell.
- The optical properties and band gap energy " E_g " for cluster samples were determined by using UV-Vis spectroscopy technique. Shows a blue shift for band gap energy that was attributed to the core/shell effect. Clusters with size up to 1.6 nm no absorption band was observed, due to quantum size effect.
- The core-shell structure of obtained clusters was confirmed by:
 - XRD: A diffraction pattern for cubic Pd was observed with no observations for Mg. due to phenomenon of heavy metal effect.

- TEM: A small sized dark particles was observed that attributed to the Pd with no observed of Mg (lighter colored particles), which confirm the Mg is in the core.
- UV-Vis analysis: one SPRB was observed. The obtained E_g -value that attributed for Pd in accordance to the hybridization theory of the plasmonic modes between core and shell.
- AAS and EDX: The detection of both metals Pd and Mg in cluster samples was observed.

2- H-storage capacity was studied by volumetric and gravimetric techniques and showed that:

- H-absorbed and desorbed reversibly by the cluster samples.
- H-storage capacity of the samples is:
 - Size dependent: small clusters absorb less hydrogen.
 - Shell composition dependent: More Pd-shell absorbs more hydrogen.
- Kinetic study shows that hydrogen can be absorbed and desorbed reversibly at ambient temperature within few minutes.
- Thermodynamic study from PCI shows three characteristic regions that are well-known for Pd-H system: anhydride phase (α -phase), transition phase ($(\alpha+\alpha')$ -phase) and hydride phase (α' -phase).

Suggestions for Farther Works

1- Studying farther parameters and their impacts on the preparation of MgPd CS clusters (i.e. reaction time, pH, and distance between electrodes ...etc.).

2- Using variant stabilizers than TOAB in stabilization the clusters and investigation their optical properties and hydrogen storage behaviors.

3- Synthesis of CS-clusters with other metallic composites and studying their optical properties and H-storage behaviors.

References

1. Li, C., et-al. **"Research progress in LiBH₄ for hydrogen storage: A review"**. *International Journal of Hydrogen Energy* 2011; 36(22):14512-14526pp.
2. Züttel, A. **"Hydrogenstorage methods"**. *Naturwissenschaften* 2004; 91(4): 157-172pp.
3. Schlapbach, L., & Züttel A. **"Hydrogen-storage materials for mobile applications"**. *Nature* 2001; 414(6861): 353-358pp.
4. Chen, X., et-al. **"Semiconductor-based photocatalytic hydrogen generation"**. *Chemical Reviews* 2010; 110(11): 6503-6570pp.
5. Corain, B., Schmid G. & Toshima, N. (Eds.) **"Metal Nanoclusters in Catalysis and Materials Science: The Issue of Size Control: The Issue of Size Control"**. Amsterdam: *Elsevier*; 2008. 67p.
6. Ni, M., et-al. **"An overview of hydrogen production from biomass"**. *Fuel processing technology* 2006; 87(5): 461-472pp.
7. David, E. **"An overview of advanced materials for hydrogen storage"**. *Journal of Materials Processing Technology* 2005; 162: 169-177pp.
8. Oriňáková, R. & Oriňák A. **"Recent applications of carbon nanotubes in hydrogen production and storage"**. *Fuel* 2011; 90(11): 3123-3140pp.
9. Sakintuna, B., Lamari-Darkrim, F. & Hirscher, M. **"Metal hydride materials for solid hydrogen storage: A review"**. *International Journal of Hydrogen Energy* 2007; 32(9): 1121-1140pp.
10. Zhou, Li. **"Progress and problems in hydrogen storage methods"**. *Renewable and Sustainable Energy Reviews* 2005; 9(4): 395-408pp.
11. Eberle, U., Felderhoff, M. & Schüth, F. **"Chemical and physical solutions for hydrogen storage"**. *Angewandte Chemie International Edition* 2009; 48(36): 6608-6630pp.

12. Klerke, A., et-al. "**Ammonia for hydrogen storage: challenges and opportunities**". *Journal of Materials Chemistry* 2008; 18(20): 2304-2310pp.
13. Aricò, A. S., et-al. "**Nanostructured materials for advanced energy conversion and storage devices**". *Nature materials* 2005; 4(5): 366-377pp.
14. Broom, D. P. "**Assessing the Performance of Potential Hydrogen Storage Materials**". Russian: *World Alternative Energy magazine*; 2012 Aug: 18-25pp.
15. Fichtner, M. "**Preface to the viewpoint set: Nanoscale materials for hydrogen storage**". *Scripta Materialia* 2007; 56(10): 801-802pp.
16. Gogotsi, Y., et-al. "**Tailoring of nanoscale porosity in carbide-derived carbons for hydrogen storage**". *Journal of the American Chemical Society* 2005; 127(46): 16006-16007pp.
17. Rowsell, J. L. C. & Yaghi, O. M. "**Strategies for hydrogen storage in metal-organic frameworks**". *Angewandte Chemie International Edition* 2005; 44(30): 4670-4679pp.
18. Niemann, M. U., et-al. "**Nanomaterials for hydrogen storage applications: a review**". *Journal of Nanomaterials* 2008; 1-9pp.
19. Kobayashi, H., et-al. "**Nanosize-Induced Hydrogen Storage and Capacity Control in a Non-Hydride-Forming Element: Rhodium**". *Journal of the American Chemical Society* 2011; 133(29): 11034-11037pp.
20. Ju-Nam Y. & Lead, J. R. "**Manufactured nanoparticles: an overview of their chemistry, interactions and potential environmental implications**". *Science of the Total Environment* 2008; 400(1): 396-414pp.
21. Bönemann, H., & Richards, R. M. "**Nanosopic Metal Particles—Synthetic Methods and Potential Applications**". *European Journal of Inorganic Chemistry* 2001; (10): 2455-2480pp.

22. Altavilla, C., & Ciliberto, E. (Eds.) **"Inorganic nanoparticles: synthesis, applications, and perspectives"**. NW: CRC Press; 2010.
23. Pradeep, T. (Ed.) **"Nano: the essentials"**. New Delhi: Tata McGraw-Hill Education; 2007.
24. **Online:**
http://depts.washington.edu/solgel/documents/class_docs/MSE502/Ch_3_Section_3.2.1-3.2.5.3.pdf; Accessed (2013 Aug. 26; 6:34am).
25. López-Lorente, A. I., Simonet, B. M. & Valcárcel, M. **"Electrophoretic methods for the analysis of nanoparticles"**. *TrAC Trends in Analytical Chemistry* 2011; 30(1): 58-71pp.
26. Chaudhuri, R. G. & Paria, S. **"Core/shell nanoparticles: classes, properties, synthesis mechanisms, characterization, and applications"**. *Chemical reviews* 2011; 112(4): 2373-2433pp.
27. Guzzi L., Paszti, Z. & Peto, G. **"Metal Nanoclusters: Electronic Aspects and Physico-Chemical Characterization"**. [Book auth.] Corain, B., Schmid, G. & Toshima, N. (Eds.) **"Metal Nanoclusters in Catalysis and Materials Science: The Issue of Size Control"**. Amsterdam: Elsevier; 2008. 77p.
28. Aiken III, J. D. & Finke, Richard G. **"A review of modern transition-metal nanoclusters: their synthesis, characterization, and applications in catalysis"** *Journal of Molecular Catalysis A: Chemical* 1999; 145(1): 1-44pp.
29. **Online:**
<http://en.wikipedia.org/wiki/Nano->; Accessed (2013 Aug. 26; 7:26am).
30. Züttel, A., et-al. **"Pd-cluster size effects of the hydrogen sorption properties"**. *Journal of alloys and compounds* 1999; 293: 472-475pp.
31. Hussain, S. T., Iqbal, M. & Mazhar, M. **"Size control synthesis of starch capped-gold nanoparticles"**. *Journal of Nanoparticle Research* 2009; 11(6): 1383-1391pp.
32. Przeniosło, R., et-al. **"Studies of the fractal microstructure of nanocrystalline and amorphous chromium obtained by**

- electrodeposition**". *Journal of alloys and compounds* 2001; 328(1): 259-263pp.
33. Mørup, S., Hansen, M. F. & Frandsen, C. (Eds.) "**Comprehensive Nanoscience and Technology**". *Elsevier*; 2011. 153-201pp.
34. Niu, W., & Xu, G. "**Crystallographic control of noble metal nanocrystals**". *Nano Today* 2011; 6(3): 265-285pp
35. Kalele, S., et-al. "**Nanoshell particles: synthesis, properties and applications**". *Current science* 2006; 91(8): 1038-1052pp.
36. Liu, J. Ping, et al., (Eds.) "**Nanoscale magnetic materials and applications**". NW: *Springer*; 2009. 35-65pp.
37. Nilus, N., Wallis, T. M. & Ho, W. "**Development of one-dimensional band structure in artificial gold chains**". *Science* 2002; 297(5588): 1853-1856pp.
38. Woodruff, D. P. (Eds.) "**Atomic clusters: from gas phase to deposit**". Vol.12. Amsterdam: *Elsevier*; 2007. 271-297pp.
39. Wu, B. & Zheng, N. "**Surface and interface control of noble metal nanocrystals for catalytic and electrocatalytic applications**". *Nano Today* 2013; 8: 168-197pp.
40. Rao, C. N. R., Thomas, P. J. & Kulkarni, G. U. (Eds.) "**Nanocrystals: synthesis, properties and applications**". Vol.95. NW: *Springer*; 2007.
41. Toshima, N., Yan H. & Shiraishi, Y. "**Recent progress in bimetallic nanoparticles: their preparation, structures and functions**". [Book auth.] Corain, B., Schmid G. & Toshima N. (Eds.) "*Metal Nanoclusters in Catalysis and Materials Science: The Issue of Size Control*". Amsterdam: *Elsevier*; 2011. 49-75pp.
42. Schmid, G. (Ed.) "**Clusters and colloids**". NW: *VCH Weinheim*; 1994.
43. Shtaya-Suleiman, M. A. M. "**Size-selective synthesis of nanometer-sized Palladium clusters and their hydrogen solvation behavior**". [Diss. Ph.D. Thesis]. *Goettingen University*, Goettingen, Germany, 2003.

44. Mallick, K., Witcomb, M. J., & Scurrall, M. S. "**Self-assembly of the metal nanoparticles: formation of the highly oriented, core-shell type, bimetallic gold–silver film**". *Journal of Nanoparticle Research* 2007; 9(2): 323-330pp.
45. Faraday M. & Trans, P. R. Soc. 1857; 147: 145-181pp.
46. Thomas, J. M. "**Colloidal metals: past, present and future**". *Pure Appl. Chem.* 1988; 60(10): 1517-1528pp.
47. Turkevich, J., Stevenson P. C. & Hillier, J. "**A study of the nucleation and growth processes in the synthesis of colloidal gold**". *Discussions of the Faraday Society* 1951; 11: 55-75pp.
48. Turkevich, J. "**Colloidal gold. Part II**". *Gold Bulletin* 1985; 18(4): 125-131pp.
49. Turkevich, J. & Kim G. "**Palladium: preparation and catalytic properties of particles of uniform size**". *Science* 1970; 169(3948): 873-879pp.
50. Peng, X., Pan, Q., & Rempel, G. L. "**Bimetallic dendrimer-encapsulated nanoparticles as catalysts: a review of the research advances**". *Chemical Society Reviews* 2008; 37(8): 1619-1628pp.
51. Cui, H., et-al. "**Strategies of large scale synthesis of monodisperse nanoparticles**". *Recent Patents on Nanotechnology* 2009; 3(1): 32-41pp.
52. D'Souza, L. "**Synthesis, Characterization and Applications of Metal and Metal Oxide Nanoparticles**". [Diss. Ph D. Thesis]. *International University Bremen*, Bremen, Germany, 2005.
53. Liz-Marzan, L. M., et-al. "**Core-Shell nanoparticles and assemblies thereof**". [Book auth.] Kreibig, U., Bönnemann, H. and Hormes, J. (Eds.) "*Nanostructured metal clusters and colloids*". *Handbook of surfaces and interfaces of materials* Vol.3. 2001. 198-235pp.

54. Watt, J., Cheong, S., & Tilley, R. D. "How to control the shape of metal nanostructures in organic solution phase synthesis for plasmonics and catalysis". *Nano Today* 2013; 8: 198-215pp.
55. Kraynov, A., Müller, T. E. & Handy S. "Concepts for the Stabilization of Metal Nanoparticles in Ionic Liquids". *Application of Ionic Liquids in Science and Technology*; 2011.
56. Fu, X., et al. "Shape-selective preparation and properties of oxalate-stabilized Pt colloid". *Langmuir* 18.12 (2002): 4619-4624.
57. Pundt, A., et al. "Hydrogen and Pd-clusters". *Materials Science and Engineering: B* 2004 108(1): 19-23pp.
58. Cookson, J. "The preparation of palladium nanoparticles". *Platinum Metals Review* 2012; 56(2): 83-98pp.
59. Pachón, L. D., et-al. "Palladium-coated nickel nanoclusters: New catalysts for Hiyama cross-coupling". *Physical Chemistry Chemical Physics* 2006; 8(1): 151-157pp.
- 60.
61. Flamberg, S., et al. "Analysis of Published Hydrogen Vehicle Safety Research". [Report No. DOTHS811267]. *US-DOE/NHTSA*. DC; 2010.
62. Hamilton, P. "Hydrogen sorption in palladium doped microporous materials". [Diss. M.Sc. Thesis] *University of Birmingham, UK*, 2009.
63. **Online:**
http://www1.eere.energy.gov/hydrogenandfuelcells/storage/pdfs/targets_onboard_hydro_storage.pdf; Accessed (2013 Sep. 4; 5:00pm).
64. Paloumpi, A. "Nanoscale magnesium as a hydrogen storage material". [Diss. Ph.D. Thesis] *University of Birmingham, UK*, 2010.
65. Ostenfeld, C. W. "A surface science approach to hydrogen storage". [Diss. Ph.D. Thesis] *DTU, Denmark*, 2005.
66. **Online:**
http://en.wikipedia.org/wiki/Energy_density; Accessed (2013 Sep. 18; 6:43pm).

67. Yang, J., et al. **"High capacity hydrogen storage materials: attributes for automotive applications and techniques for materials discovery"**. *Chemical Society Reviews* 2010; 39(2): 656-675pp.
68. Singh, A. and Singh, R. (Ed) **"Surface Chemistry"**. New Delhi: *Campus Book International*; 2005.
69. Doyle, M. L., et al. **"Hydrogen storage materials- The Characterization of Their Storage Properties"** *U.S. Patent No. 6,165,643*. 26 Dec. 2000.
70. Burch, R. **"The Adsorption and Absorption of Hydrogen by Metals"** [Book Auth.] M W Roberts, J M Thomas (Eds) **"Chemical Physics of Solids and Their Surfaces."** Vol.8. 1980,1-17pp
71. Kang, B. and Sohn, K. **"Diffusion process and interactions of hydrogen atoms in Pd."** *Physica: B*. 1995; 205(2):163-168pp
72. Kang, B-S. and Sohn, K-S. **"Barriers for diffusion and interactions with hydrogen in palladium."** *Physica: B*. 1996; 217(1): 160-166pp
73. Züttel, A. **"Materials for hydrogen storage."** *Materials today*. 2003; 6(9): 24-33pp.
74. Van Mal, H. H. (EDs) **"Stability of ternary hydrides and some applications"**. *Philips Research Laboratories*, 1976.
75. Broom, D. P. **"Hydrogen storage materials: the characterisation of their storage properties"**. UK: *Springer*; 2011.
76. Stuhr, U., et al. **"An investigation of hydrogen diffusion in nanocrystalline Pd by neutron spectroscopy."** *Journal of alloys and compounds*. 1997; 253: 393-396pp.
77. Szatanik, R. and Pietrzak, R. **"Influence of crystal defects on the electromigration of the hydrogen in palladium."** *Physica B: Condensed Matter*. 2001; 307(1): 211-216pp.
78. Pietrzak, R., and Szatanik, R. **"Influence of external stretching on hydrogen electromigration in Pd and PdCu, PdAg alloys."** *Physica B: Condensed Matter*. 2005; 367(1): 165-171pp.

79. Cizek, J., et al. "**Hydrogen-induced defects in niobium.**" *Journal of Alloys and Compounds*. 2007; 446: 479-483pp.
80. Van-den Berg, A. and Areán, C. "**Materials for hydrogen storage: current research trends and perspectives.**" *Chemical Communications*. 2008; (6): 668-681.
81. Andreasen, A. "**Design and building of a new experimental setup for testing hydrogen storage materials.**" *Risø National Laboratory*, Roskilde, Denmark, 2005.
82. Lennard-Jones, J. E. "**Processes of adsorption and diffusion on solid surfaces.**" *Transactions of the Faraday Society*. 1932; 28: 333-359pp.
83. Pundt, A., and R. Kirchheim. "**Hydrogen in metals: microstructural aspects.**" *Annu. Rev. Mater. Res.* 2006; 36: 555-608pp.
84. Suleiman, M., et al. "**Phase transition and lattice expansion during hydrogen loading of nanometer sized palladium clusters.**" *Journal of alloys and compounds*. 2003; 356: 644-648pp.
85. Yamauchi, M., et al. "**Nanosize effects on hydrogen storage in palladium.**" *The Journal of Physical Chemistry C*. 2008; 112(9): 3294-3299pp.
86. Narehood, D. G., et al. "**X-ray diffraction and H-storage in ultra-small palladium particles.**" *International Journal of Hydrogen Energy*. 2009; 34(2): 952-960pp.
87. Flanagan, B. and Oates, W. "**The palladium-hydrogen system.**" *Annual Review of Materials Science*. 1991; 21(1): 269-304pp.
88. Adams, B. D. and Chen, A. "**The role of palladium in a hydrogen economy.**" *Materials Today*. 2011; 14(6): 282-289pp.
89. Crespo, E. A., et al. "**Thermodynamics of hydrogen in Pd nanoparticles.**" *International Journal of Hydrogen Energy*. 2010; 35(11): 6037-6041pp.

90. Bardhan, Rizia, et al. **"Uncovering the intrinsic size dependence of hydriding phase transformations in nanocrystals."** *Nature materials*. 2013; 12(10): 905-912pp.
91. Laudahn, U., et al. **"Hydrogen-induced stress in Nb single layers."** *Journal of alloys and compounds*. 1999; 293: 490-494pp.
92. Pundt, A., et al. **"Hydrogen sorption in elastically soft stabilized Pd-clusters."** *Journal of alloys and compounds*. 1999; 293: 480-483pp.
93. Salomons, E., et al. **"Surface tension and subsurface sites of metallic nanocrystals determined from H-absorption."** *EPL (Europhysics Letters)*. 1988; 5(5): 449p.
94. Naito, S., et al. **"Sloping plateaux in the pressure–composition isotherms of the titanium–hydrogen and Ti₉₄Al₆–hydrogen systems."** *Journal of the Chemical Society, Faraday Transactions*. 1995; 91(22): 4143-4147pp.
95. Pasquini, L., et al. **"Magnesium nanoparticles for hydrogen storage: structure, kinetics and thermodynamics."** *IOP Conference Series: Materials Science and Engineering*. 2012; 38(1): 1-8pp.
96. Xu, X., Zheng, J. and Song, C. **"Dynamic measurement of hydrogen storage/release properties using tapered element oscillating microbalance for Mg doped with nano-sized Pd catalyst."** *Prepr. Pap.-Am. Chem. Soc., Div. Fuel Chem*. 2004; 49(1): 210p.
97. Langohr, D., et al. **"Development of a volumetric method—experimental test bench for hydrogen storage characterisation."** *International Journal of Hydrogen Energy*. 2007; 32(12): 1846-1854pp.
98. Jain, I. P., Lal, C. and Jain, A. **"Hydrogen storage in Mg: a most promising material."** *International Journal of Hydrogen Energy*. 2010; 35(10): 5133-5144pp.
99. **Online:**
<http://www.rsc.org/chemistryworld/News/2005/November/29110502.asp>, Accessed (19 Oct. 2013; 4.57pm)

100. Stakheev, Y., et al. **"Formation of palladium hydride nanoparticles in Pd/C catalyst as evidenced by in situ XAS data."** *Russian Chemical Bulletin*. 2009; 58(2): 280-283pp.
101. Sekiguchi, Y., Hayashi, Y. and Takizawa, H. **"Synthesis of palladium nanoparticles and palladium/spherical carbon composite particles in the solid-liquid system of palladium oxide-alcohol by microwave irradiation."** *Materials transactions*. 2011; 52(5): 1048-1052pp.
102. Tan, S., et al. **"Hydrogen-sensitive sensor with stabilized Pd-mixture forming sensing nanoparticles on an interlayer."** *International Journal of Hydrogen Energy*. 2011; 36(23): 15446-15454pp.
103. Noh, J., Lee, M. and Lee, W. **"Low-dimensional palladium nanostructures for fast and reliable hydrogen gas detection."** *Sensors*. 2011; 11(1): 825-851pp.
104. Lewis, F. A. **"The hydrides of palladium and palladium alloys."** *Platinum Metals Rev.* 1960; 4(4): 132p.
105. Broom, D. P. **"The accuracy of hydrogen sorption measurements on potential storage materials."** *International Journal of Hydrogen Energy*. 2007; 32(18): 4871-4888pp.
106. Messmer, R. P., et al. **"The interaction of atomic hydrogen with Ni, Pd, and Pt clusters."** *Chemical Physics Letters*. 1977; 51(1): 84-89pp.
107. Rather, S., et al. **"Hyperstoichiometric hydrogen storage in monodispersed palladium nanoparticles."** *Chemical physics letters*. 2007; 438(1): 78-84pp.
108. Vons, V. A., et al. **"Hydrogen storage properties of spark generated palladium nanoparticles."** *International Journal of Hydrogen Energy*. 2010; 35(11): 5479-5489pp.

109. David, E. **"Nanocrystalline magnesium and its properties of hydrogen sorption."** *Journal of Achievements in Materials and Manufacturing Engineering*. 2007; 20: 87-90pp.
110. Vons, V. A., et al. **"Low-temperature hydrogen desorption and the structural properties of spark discharge generated Mg nanoparticles."** *Acta Materialia*. 2011; 59(8): 3070-3080pp.
111. Gutfleisch, O., et al. **"Hydrogenation properties of nanocrystalline Mg-and Mg₂Ni-based compounds modified with platinum group metals (PGMs)."** *Journal of alloys and compounds*. 2003; 356: 598-602pp.
112. **Online:**
<https://notendur.hi.is/~hj/HstorageBrief.pdf> Accessed (19 Oct. 2013; 5.24pm "Árnason, B., Jónsdóttir F. and Hafsteinsson H. **"Light Metal Alloys for Hydrogen Storage."**
113. Pasquini, L., et al. **"Magnesium nanoparticles with transition metal decoration for hydrogen storage."** *Journal of Nanoparticle Research*. 2011; 13(11): 5727-5737pp.
114. Hanada, N., Ichikawa, T. and Fujii, H. **"Catalytic effect of Ni nanoparticle and Nb oxide on H-desorption properties in MgH₂ prepared by ball milling."** *Journal of alloys and compounds*. 2005; 404: 716-719pp.
115. Orimo, S., et al. **"Hydriding properties of the MgNi-based systems."** *Journal of alloys and compounds*. 1999; 293: 437-442pp.
116. Cui, N., He, P., and Luo, J. L. **"Synthesis and characterization of nanocrystalline magnesium-based hydrogen storage alloy electrode materials."** *Electrochimica acta*. 1999; 44(20): 3549-3558pp.
117. Yoshimura, K., et al. **"Optical switching property of Pd-capped Mg–Ni alloy thin films prepared by magnetron sputtering."** *Vacuum*. 2006; 80(7): 684-687pp.
118. Baum, L., Meyer M., and Mendoza-Zélis, L. **"Hydrogen storage properties of the Mg/Fe system."** *Physica B: Condensed Matter*. 2007; 389(1): 189-192pp.

119. Higuchi, K., et al. **"Remarkable hydrogen storage properties in three-layered Pd/Mg/Pd thin films."** *Journal of alloys and compounds*. 2002; 330: 526-530pp.
120. Paillier, J. and Roue, L. **"Hydrogen electrosorption and structural properties of nanostructured Pd–Mg thin films elaborated by pulsed laser deposition."** *Journal of alloys and compounds*. 2005; 404: 473-476pp.
121. Yoshimura, K. **"anomalous structure of palladium-capped magnesium thin films."** *Metals*. 2012; 2(3): 253-257pp.
122. Xie, W., et al. **"Role of nano in catalysis: Palladium catalyzed hydrogen desorption from nanosized magnesium hydride."** *Nano Energy*. 2013; 2(5): 742-748pp.
123. Siviero, G., et al. **"Structural evolution of Pd-capped Mg thin films under H₂ absorption and desorption cycles."** *International Journal of Hydrogen Energy*. 2009; 34(11): 4817-4826pp.
124. Callini, E., et al. **"Hydrogen sorption in Pd-decorated Mg–MgO core-shell nanoparticles."** *Applied Physics Letters*. 2009; 94(22): 221905-221905pp.
125. M. Suleiman et al. **"In-situ XRD for Mg/Pd core/shell clusters."** *Unpublished results*. (2014).
126. Coronado, E., et al. **"Synthesis, characterization and magnetism of monodispersed water soluble palladium nanoparticles."** *Journal of Materials Chemistry*. 2008; 18(46): 5682-5688pp.
127. Chen, S., Yao H. and Kimura, K. **"Reversible transference of Au nanoparticles across the water and toluene interface: A Langmuir type adsorption mechanism."** *Langmuir*. 2001; 17(3): 733-739pp.
128. Venkatesan, P. and J. Santhanalakshmi. **"Core-shell bimetallic Au-Pd nanoparticles: synthesis, structure, optical and catalytic properties."** *Nanoscience and Nanotechnology*. 2011; 1(2): 43-47pp.

129. Coleman, D. M. "**Design and Delivery of Water Soluble Gold Nanoparticles Containing Mixed Monolayers of Thiolated Polyethylene Glycol and Peptides to HeLa Cells.**" [Diss. M.Sc. Thesis]. *North Carolina State University*, Raleigh, North Carolina, 2004.
130. Muhammed, H. and Pradeep, T. "**Aqueous to organic phase transfer of Au₂₅ clusters.**" *Journal of Cluster Science*. 2009; 20(2): 365-373pp.
131. Freund, H. and Roberts, W. "**Surface chemistry of carbon dioxide.**" *Surface Science Reports*. 1996; 25(8): 225-273pp.
132. Ibanez, F. J. and Zamborini, F. P. "**Reactivity of hydrogen with solid-state films of alkylamine-and tetraoctylammonium bromide-stabilized Pd, PdAg, and PdAu nanoparticles for sensing and catalysis applications.**" *Journal of the American Chemical Society*. 2008; 130(2): 622-633pp.
133. Galhotra, P. "**Carbon dioxide adsorption on nanomaterials.**" [Diss. Ph.D.. Thesis]. *University of Iowa*, Iowa, US-State, 2010.
134. Matthew M. C., et al. "**Preparing water-dispersed palladium nanoparticles via polyelectrolyte nanoreactors.**" *Chemical Science*. 2010; 1(6): 772-775pp.
135. Li, J., et al. "**Analyzing the structure of CoFe-Fe₃O₄ core-shell nanoparticles by electron imaging and diffraction.**" *The Journal of Physical Chemistry B*. 2004; 108(37): 14005-14008pp.
136. Teng, X., et al. "**Platinum-maghemite core-shell nanoparticles using a sequential synthesis.**" *Nano Letters*. 2003; 3(2): 261-264pp.
137. Dibandjo, P., et al. "**Hydrogen storage in hybrid nanostructured carbon/palladium materials: Influence of particle size and surface chemistry.**" *International Journal of Hydrogen Energy* (2013) 38(2); 952-965pp.

138. Shen, C. M., et al. "**Synthesis and characterization of *n*-octadecylmercaptan-protected palladium nanoparticles.**" *Chemical physics letters*. 2003; 373(1): 39-45pp.
139. Holzwarth, U. and Gibson, N. "**The Scherrer equation versus the 'Debye-Scherrer equation'.**" *Nature Nanotechnology*. 2011; 6(9): 534-534pp.
140. Shah, A., et al. "**Synthesis, characterization and applications of bimetallic (Au-Ag, Au-Pt, Au-Ru) alloy nanoparticles.**" *Review on Advanced Materials Science*. 2010; 30(2): 133-149pp.
141. Garcia-Torres, J., Vallés, E. and Gómez, E. "**Synthesis and characterization of Co-Ag core-shell nanoparticles.**" *Journal of Nanoparticle Research*. 2010; 12(6): 2189-2199pp.
142. Singh, P., et al. "**Enhancing the hydrogen storage capacity of Pd-functionalized multi-walled carbon nanotubes.**" *Applied Surface Science*. 2012; 258(8): 3405-3409pp.
143. Yu, Y., et al. "**Shape-controlled synthesis of palladium nanocrystals by microwave irradiation.**" *Pure and Applied Chemistry*. 2009; 81(12): 2377-2385pp.
144. Iglesias-Silva, E., et al. "**Synthesis of silver-coated magnetite nanoparticles.**" *Journal of Non-Crystalline Solids*. 2007; 353(8): 829-831pp.
145. Sun, H., et al. "**Solvothermal preparation of Pd nanostructures under nitrogen and air atmospheres and electrocatalytic activities for the oxidation of methanol.**" *ACS applied materials & interfaces*. 2011; 3(7): 2425-2430pp.
146. Adams, B. D., et al. "**Facile synthesis of Pd- Cd nanostructures with high capacity for hydrogen storage.**" *Journal of the American Chemical Society*. 2009; 131(20): 6930-6931pp.
147. Suleiman, M., et al. "**Hydrogen absorption in 3.1 nanometre sized palladium samples: does structure matter?.**" *International journal of materials research*. 2008; 99(5): 528-534pp.

148. Bian, Z., et al. **"In situ encapsulation of Au nanoparticles in mesoporous core-shell TiO₂ microspheres with enhanced activity and durability."** *Chemical Communications*. 2009; (25): 3789-3791pp.
149. Moores, A. and Goettmann, F. **"The plasmon band in noble metal nanoparticles: an introduction to theory and applications."** *New Journal of Chemistry*. 2006; 30(8): 1121-1132pp.
150. Nemamcha, A. and Rehspringer, J. L. **"Morphology of dispersed and aggregated PVP-Pd nanoparticles prepared by ultrasonic irradiation of Pd (NO₃)₂ solutions in ethylene glycol."** *Reviews on Advanced Materials Science*. 2008; 18(8): 687-690pp.
151. Nguyen, V. L., et al. **"Chemical synthesis and characterization of palladium nanoparticles."** *Advances in Natural Sciences: Nanoscience and Nanotechnology*. 2010; 1(3): 1-5pp.
152. Haas, I. and Gedanken, A. **"Synthesis of metallic magnesium nanoparticles by sonoelectrochemistry."** *Chem. Commun.* 2008 (15): 1795-1797pp.
153. Moon, H., Urban J. J. and Milliron, D. J. **"Size-controlled synthesis and optical Properties of monodisperse colloidal magnesium oxide nanocrystals."** *Angewandte Chemie International Edition*. 2009; 48(34): 6278-6281pp.
154. Csapó, E., et al. **"Synthesis and characterization of Ag/Au alloy and core (Ag)-shell (Au) nanoparticles."** *Colloids and Surfaces A: Physicochemical and Engineering Aspects*. 2012; 415: 281-287pp.
155. Chen, L., et al. **"Characterization of Ag/Pt core-shell nanoparticles by UV-Vis absorption, resonance light-scattering techniques."** *Spectrochimica Acta Part A: Molecular and Biomolecular Spectroscopy*. 2007; 68(3): 484-490pp.

كلية الدراسات العليا

جامعة النجاح الوطنية

تحضير جسيمات بحجم النانومتر من معدن المغنيسيوم المغلف
بمعدن البلاديوم ودراسة قدرتها على امتصاص الهيدروجين

إعداد

ضياء "محمد معروف" صالح عارف

إشراف

الدكتور محمد عبد القادر سليمان

قدمت هذه الأطروحة استكمالاً لمتطلبات درجة الماجستير في الكيمياء بكلية الدراسات العليا في
جامعة النجاح الوطنية في نابلس، فلسطين.

2014

ب

تحضير جسيمات بحجم النانومتر من معدن المغنيسيوم المغلف بمعدن البلاديوم

ودراسة قدرتها على امتصاص الهيدروجين

اعداد

ضياء "محمد معروف" صالح عارف

اشراف

د. محمد عبد القادر سليمان

الملخص

لم يعد يخفى في هذا القرن (القرن الواحد والعشرون) اهمية الجسيمات بحجم النانو لما تحتويه من خصائص فيزيائية وكيميائية مميزة. وفي الوقت الحالي عظم الاهتمام بشكل خاص على التحضير الهندسي لهذه الجسيمات من حيث التحكم في حجمها واشكالها وتركيبها الجزيئي من حيث ترتيب الجزيئات و الذرات المكونة لهذه الجسيمات وما يتبعها من خصائص مغايرة.

في هذه الدراسة تم تحضير جسيمات بحجم النانومتر والمكونة من معدني المغنيسيوم المغلفة بالبلاديوم و المثبتة بجزيئات بروميد الامونيوم رباعي(الاكتيل) المستخدمة كمثبطات نمو لجسيمات النانو المحضرة ومنع تراكمها الى جسيمات اكبر من حجم النانو. عملية التحضير تمت بالاعتماد على عمليتي الاختزال المترامنة من الاختزال الملحي و الاختزال الكهروكيميائي باستخدام الخلية الكهركيميائية البسيطة. ومن ثم باستخدام تقنيات التحليل المختلفة (TEM, FT-IR, XRD, AAS...) تم التحقق من حجوم وأشكال وتركيب الجسيمات الناتجة ومن كونها على الشكل الهندسي المتمثل بالمغنيسيوم (الكور) المغلفة بالبلاديوم. بالاضافة الى دراسة خصائصها الضوئية و طاقة الفجوة الحزمية لتركيبها الجزيئي (E_g) باستخدام المطياف الضوئي (المرئي - فوق بنفسجي) "UV-Vis spectroscopy". التحقق من قدرة هذه الجسيمات على امتصاص غاز الهيدروجين و استخراج كمية الهيدروجين الممتصة مرة اخرى بفاعلية تمت دراستها ايضا باستخدام ميزان الكتروني حساس مفرغ من الهواء (UHVEM).

ت

وبعد التحقق من الجسيمات الناتجة، وجد ان جسيمات من معدن المغنيسيوم المغلف بمعدن البلاديوم والمثبتة بمثبطات النمو تم تحضيرها بنجاح. وعند فحص حجمها باستخدام تقنيات (TEM, XRD) وجد ان حجمها لا يتجاوز (5 نانوميتر) بتوزيع حجمي لا يتجاوز (1 نانوميتر) وكما تم دراسة اثر تغيير كثافة التيار الكهربائي و الكمية البدائية من معدن المغنيسيوم (الكور) المستخدمة على الجسيمات الناتجة من حيث حجمها و نسبة جزيئاتها المكونه لها. وقد وجد ان حجم الجسيمات الناتجة تقل مع زيادة كثافة التيار الكهربائي او مع تقليل كمية المغنيسيوم المستخدمة.

ومع دراسة خصائصها الضوئية بالاعتماد على تتبع نسبة الامتصاص للاطوال الموجية المختلفة وتتبع التردد البلازموني السطحي (SPRB) و من خلال ايضا حساب طاقة الفجوة الحزمية (E_g) لهذه الجسيمات الناتجة. وجد ان خصائصها الضوئية تتبع التشتت الضوئي لقانون ماي (Mie scattering) لجسيمات البلاديوم، وهذا يعتبر دليل اخر على ان الجسيمات مكونه من البلاديوم على سطحها مع وجود (SPRB) في منطقة الضوء المرئي وتتحرف باتجاه مناطق الاطاقة الاعلى (انخفاض في الطول الموجي) كلما قلت نسبة البلاديوم على سطحها. ووجد ايضا ان لها طاقة فجوة لتركيبها الجزيئي يتراوح بين (3,0-3,3 إلكترون فولت) والتي تزداد مع انخفاض كمية البلاديوم المغلفة للمغنيسيوم على سطح هذه الجسيمات الناتجة.

التحقق من قدرة الجسيمات المحضرة على امتصاص الهيدروجين تم من خلال دراسة العينات المحضرة باستخدام طريقتي الفحص (Gravimetric و Volumetric)، وابتدت قدرة عالية لامتصاص الهيدروجين. كما تم دراسة عينة تحوي على جسيمات بحجم 3,5 نانوميتر ونسبة مولية بين المغنيسيوم و البلاديوم تكافئ (Mg_1Pd_3)، ووجد ان لها قدرة جيدة على امتصاص الهيدروجين بحيث امتصت ما نسبته (1,22% نسبة كتلية) و كونت هيدريدات بالشكل الجزيئي ($Mg_1Pd_3H_{4.2}$)، مع سرعة امتصاص واستخلاص للهيدروجين الممتصة بنسبة تصل الى 100% في غضون دقائق معدودة.